UC Santa Barbara
UC Santa Barbara Electronic Theses and Dissertations

Title
Microplasma jet sources for direct deposition of thin films and nanomaterials

Permalink
https://escholarship.org/uc/item/5w55m606

Author
Mackie, Katherine E

Publication Date
2019

Peer reviewed|Thesis/dissertation

eScholarship.org Powered by the California Digital Library
University of California

University of California
Santa Barbara

Microplasma jet sources for direct deposition of thin films and nanomaterials

A dissertation submitted in partial satisfaction
of the requirements for the degree

Doctor of Philosophy
in
Chemistry

by

Katherine E. Mackie

Committee in charge:

Professor Michael J. Gordon, Co-Chair
Professor Galen D. Stucky, Co-Chair
Professor Dan Morse
Professor Horia Metiu
Professor Steve Buratto

June 2019

The Dissertation of Katherine E. Mackie is approved.

Professor Dan Morse

Professor Horia Metiu

Professor Steve Buratto

Professor Galen D. Stucky, Committee Co-Chair

Professor Michael J. Gordon, Committee Co-Chair

March 2019

Microplasma jet sources for direct deposition of thin films and nanomaterials

Copyright © 2019

by

Katherine E. Mackie

Acknowledgements

First, I would like to sincerely thank my thesis advisors, Profs Michael Gordon and Galen Stucky. Mike, you are one of the most impressive experimentalists I've ever known and over these last six years you have convinced me over and over again that we really can build anything! It has been a pleasure and a privilege to work with you - I have learned more from you than you know. I've also enjoyed and valued our discussions on topics ranging from world travel to the Dune series. Thank you so much for everything.

I would also like to thank a few of the characterization facilities managers on campus - Mark Cornish, Dr. Tom Mates, Dr. Youli Li. Thank you all for not only maintaining the user facilities, but for taking the time to teach me the operating principles of each technique. I'd also like to acknowledge the horde of undergraduates and Master's exchange students who have contributed to the project over the years; especially Julia Brockmeier. Julia, you and I joined the Gordon group around the same time and I was and am so grateful to have had you as a colleague and friend during those first few months. And also thank you to Korina Hartmann, who didn't work directly on the project, but was a great friend and a wonderful addition to lab. Thanks to Igor Chiasso and Moritz Follner as well for months of amazing work.

I am very grateful for both the Gordon and Stucky groups and all the friendships forged in graduate school. Pebbles, you were the only colleague in lab with whom I could discuss the (sometimes) infuriating complexities of plasma-based deposition. You've also been like a big brother to me in many respects - in both always having my back and the constant banter! Alex, you are quite possibly the most positive person I've ever known. Even in the trenches of grad school, your sense of humor and overall enthusiasm made lab a brighter place... as did your stash of bourbon. Rich, I'm grateful for your friendship and will always remember the rat-catching sagas. Fed, Lesley, Louis, Liz, Katherine,

Tracy, Pavel, Ryan, and Sheng - you all made this experience a very special one, full of shenanigans - thank you all.

I'd also like to thank my dear friend, Lacey, for years of support and friendship (i.e., putting up with years of complaining). Lacey, thanks for not reminding me of just how much my estimated time-to-degree has changed over the last 4, 5, 6, no, 6.5 years. To my family, thank you, and especially Dad - thank you for supporting this (arguably crazy) path. I'd also like to acknowledge my grandparents who encouraged curiosity in the natural world and who were always ready to enthusiastically delve into any topic, be it the origins of the "Empress tree", nanotechnology, or the intricacies of grain production.

And finally, my last year and a half of graduate school would certainly not have been the same without my wonderful Zach. I am beyond grateful for all the support, practical advice, the home-cooked meals, and your delightful, sanity-saving sense of humor.

Curriculum Vitæ

Katherine E. Mackie

Education

2019	Ph.D. in Chemistry (Expected), University of California, Santa Barbara.
2008	B.S. in Chemistry (minors in Physics and Mathematics), Whitworth University.

Publications

- K. E. Mackie, M. J. Gordon, "Optical emission spectroscopy and Langmuir probe investigations of low pressure microplasma jets used for materials deposition", *Manuscript in preparation.*
- K. E. Mackie, A. C. Pebley, M. J. Gordon, "Microplasma spray deposition of vertically-aligned MnO_2 nanostructures for solid-state, planar microsupercapacitors", *Manuscript in preparation.*
- K. E. Mackie, A. C. Pebley, M. M. Butala, J. Zhang, G. D. Stucky, M. J. Gordon, "Microplasmas for direct, substrate-independent deposition of nanostructured metal oxides", *Applied Physics Letters*, **2016**, 109(3), 033110.
- W. Chouyyok, C. L. Warner, K. E. Mackie, M. G. Warner, G. A. Gill, R. S. Addleman, "Nanostructured metal oxide sorbents for the collection and recovery of uranium from seawater", *Ind. Eng. Chem. Res.*, **2015**.
- C. L. Warner, W. Chouyyok, K. E. Mackie, D. Neiner, L. V. Saraf, T. C. Droubay, M. G. Warner, R. S. Addleman, "Manganese doping of magnetic iron oxide nanoparticles: Tailoring surface reactivity for regenerable heavy metal sorbent", *Langmuir*, **2012**, 28 (8), 3931-3937.
- M. Losada, K. E. Mackie, J. Osborne, S. Chaudhuri, "Understanding Nanoscale Wetting using Dynamic Local Contact Angle Method", *Advanced Materials Research*, **2010**, Vol 138, 107-116.
- T. Kim, K. E. Mackie, Q. Zhong, M. Peterson, H. Tam, T. Konno, R. H. Dauskardt, "Surfactant mobility in nanoporous glass films", *Nano Letters*, **2009**, 9(6), 2427 - 2432.

Presentations

- K. E. Mackie, M. J. Gordon, "Microplasma spray deposition of metal oxide nanostructures for energy applications", *AVS 64th International Symposium*, Tampa, FL, **2017**.

- K. E. Mackie, M. J. Gordon, “Microplasma-based deposition of functional nanomaterials for energy storage applications”, *ACS Spring Meeting 2017*, San Francisco, CA, **2017**.

Scholarships and awards

2013-2015	PIRE-ECCI Fellowship (“The Partnership in International Research and Education in Electron Chemistry and Catalysis at Interfaces”)

Abstract

Microplasma jet sources for direct deposition of thin films and nanomaterials

by

Katherine E. Mackie

The ability to synthesize a wide range of nanostructured materials, as well as integrate them into larger systems, is fundamental to the development of next-generation micro- and optoelectronic devices, sensors, and energy harvesting and storage technologies. Toward this goal, we have developed a versatile, plasma spray-like deposition technique, based on flow-through microhollow cathode discharges (MHCDs) at 10-100 Torr. These microplasma jet sources can deposit nanoparticles, dense layers, and structured thin films of crystalline materials on virtually any surface (e.g., conductors, insulators, polymers, fibers, and lithographic patterns). Supersonic microplasma jets are seeded with organometallic precursors under oxidizing conditions to create a directed flux of growth species (e.g., atoms, ions, clusters, and/or nanoparticles) that are subsequently 'spray-deposited' onto the surface of interest at room temperature. A diverse range of nanostructured transition metal oxide materials, e.g., CuO, MnO_2, RuO_2, NiO, Fe_2O_3, Co_xO_y, and spinels ($NiCo_2O_4$) can be realized with the technique. These films were then used for electrochemical energy storage applications and are discussed with emphasis on the fabrication of microscale energy storage devices. We also highlight detailed measurements of T_{rot}, T_{vib}, T_e, and n_e on various jets made using trace gas optical emission spectroscopy (OES) and Langmuir probe studies.

Contents

Curriculum Vitae **vi**

Abstract **viii**

1 Introduction to plasmas and plasma-based materials processing **1**
1.1 Plasma basics 2
1.2 MHCDs for materials deposition and synthesis: A review of previous work 14
1.3 Thesis overview 21

2 Microhollow cathode discharge-based plasma deposition system **23**
2.1 Microhollow cathode discharge (MHCD) source 23
2.2 Fluid mechanics of the MHCD (microplasma) jet source 26
2.3 MHCD-based plasma jet deposition system 28
2.4 Plasma diagnostics 32
2.5 Microplasma deposition systems 34

3 Optical emission spectroscopy and Langmuir probe studies of a low pressure microplasma jet deposition source **36**
3.1 Experimental setup 37
3.2 Results and discussion 42
3.3 Summary and conclusions 52

4 Microplasmas for direct, substrate-independent deposition **54**
4.1 Introduction 55
4.2 Experimental details 56
4.3 Results and discussion 58
4.4 Conclusions 65

5 Importance of substrate charging during microplasma jet deposition **66**
5.1 Introduction 67
5.2 Experimental details 68
5.3 Results 70

5.4 Discussion 80
5.5 Conclusions and future work 81

6 Microplasma-deposited materials for electrochemical energy storage 82
6.1 Introduction to electrochemical capacitors 83
6.2 Pseudocapacitive materials 86
6.3 Nickel oxide nanostructures on carbon fiber for hierarchical pseudocapacitors 95
6.4 Microplasma spray deposition of vertically-aligned MnO_2 nanostructures for solid-state, planar microsupercapacitors 101

7 Thesis summary 111

Bibliography 113

Chapter 1

Introduction to plasmas and plasma-based materials processing

The purpose of this chapter is not only to introduce the work that will be presented in this thesis, but to help orient the reader in the particular context of this research in the vast fields of plasma physics and plasma-based materials processing. Plasma-based processing of materials is ubiquitous in industry today and for good reason - the reactive environment of even a weakly ionized gas enables access to unique chemical reaction pathways and momentum-assisted mechanisms for materials growth and processing. Examples include "dry" etching of materials, sputter deposition, ion implantation, and plasma-enhanced chemical vapor deposition processes, the latter being the primary focus of this work. But before diving into this, its useful to consider the fundamentals that define the physics of the systems that will later be described, specifically, microhollow cathode discharges or "microplasmas". This chapter provides a broad overview of the salient features of plasma physics relevant to this thesis.

1.1 Plasma basics

The term “plasma”, coined by Irving Langmuir, refers to a quasi-neutral, partially ionized gas. It is a collection of electrons, ions, and neutral atoms/molecules where the number of electrons is approximately equal to the number of positive ions; that is, $n_{e^-} \approx n_i$. Ionization occurs due to either extreme heating (thermal means) or electrical breakdown. In the later case, the degree of ionization is generally low, $10^{-3} - 10^{-4}$ [1]. Most electrically-driven laboratory plasmas are highly non-equilibrium or “non-thermal”, i.e., the electron temperatures far exceed temperatures of the neutral species and ions $T_e \gg T_{n,i}$. As such, electrically-driven discharges often exhibit room temperature neutral atoms/ions and electron temperatures of several eV (10,000 - 50,000 K). These high energy electrons are very effective at ionizing atoms and dissociating molecules [2]. When this kind of environment is used for nanomaterials synthesis, gaseous precursors are easily dissociated into radicals and ions that readily react under relatively mild processing conditions (i.e., no high temperatures, solvents, ligands/capping agents, etc. are required). Dissociation is a result of any one of a large number of various elementary plasma processes and collisions that occur in a plasma environment, the extent of which is dependent on factors such as the plasma number densities of ions, electrons, and neutrals. Collisions between species in a plasma fall into one of two catagories - elastic collisions, which result in scattering and no transfer of kinetic energy, and inelastic collisions, where kinetic energy is transfered [3]. This latter case is where excitation, dissociation, and ionization of molecules and atoms occur. A handful of two-body collision processes are given in Table 1.1 and are shown here to emphasize the complexities of processes that can occur in a plasma.

In most electrically-driven plasmas (i.e., non-thermal plasmas), the electrons are preferentially heated by the applied power, while the heavier ions efficiently exchange energy

Class	Reacting particles	Reactions	Name of collision
Photon-induced	Photon, N	$Photon + N \rightarrow N^*$	Photo-excitation
reactions	"	$Photon + N \rightarrow e + N^+$	Photo-ionization
Electron-induced	e, N, N_2	$e + N \rightarrow e + N^*$	Excitation by e^- impact
reactions	"	$e + N \rightarrow e + 2N$	Dissociation by e^- impact
	e, N^{**}	$e + N^{**} \rightarrow e(fast) + N$	Superelastic collision
	e, N^+	$e + N^+ \rightarrow N + Photon$	Radiative recombination
		$e + N_2^+ \rightarrow 2N$	Dissociative recombination
Ion-induced reactions	$N^+(1), N(2)$	$N^+(1) + N(2) \rightarrow N(1) + N^+(2)$	Charge exchange
Atomic or	N^*, M	$N^* + M \rightarrow M^+ + N$	Penning ionization
molecular reactions	$N^*, Nor M_2$	$N^* + N(or M) \rightarrow N + M^*$	De-excitation by atomic/ molecular impact

Table 1.1: List of two-body inelastic collision processes commonly observed in plasmas. (e: electron, N, M: neutrals, N_2: diatomic molecule, N^+: positive ion, N^*: excited atom, N^{**}: metastable atom). Adapted from [1].

by collision with the background gas, thus maintaining a lower temperature [2]. These interactions and collisions between electrons, neutrals, atoms and molecules, vibrationally and rotationally excited particles, ionized atoms and ions, etc. ultimately define the plasma parameters T_e, $T_{n,i}$, and the temperature of the discharge T_{gas}. Figure 1.1 shows a variety of plasma types as a function of electron temperature (T_e) and electron density (n). The solar corona is an example of a low density plasma with high electron temperatures, shown in the lower half of Figure 1.1, while a high pressure arc plasma exhibits high densities and lower electron temperatures (upper left of Figure 1.1). Non-equilibrium, low pressure glow discharges (the shaded region in Figure 1.1) will be the focus of this thesis.

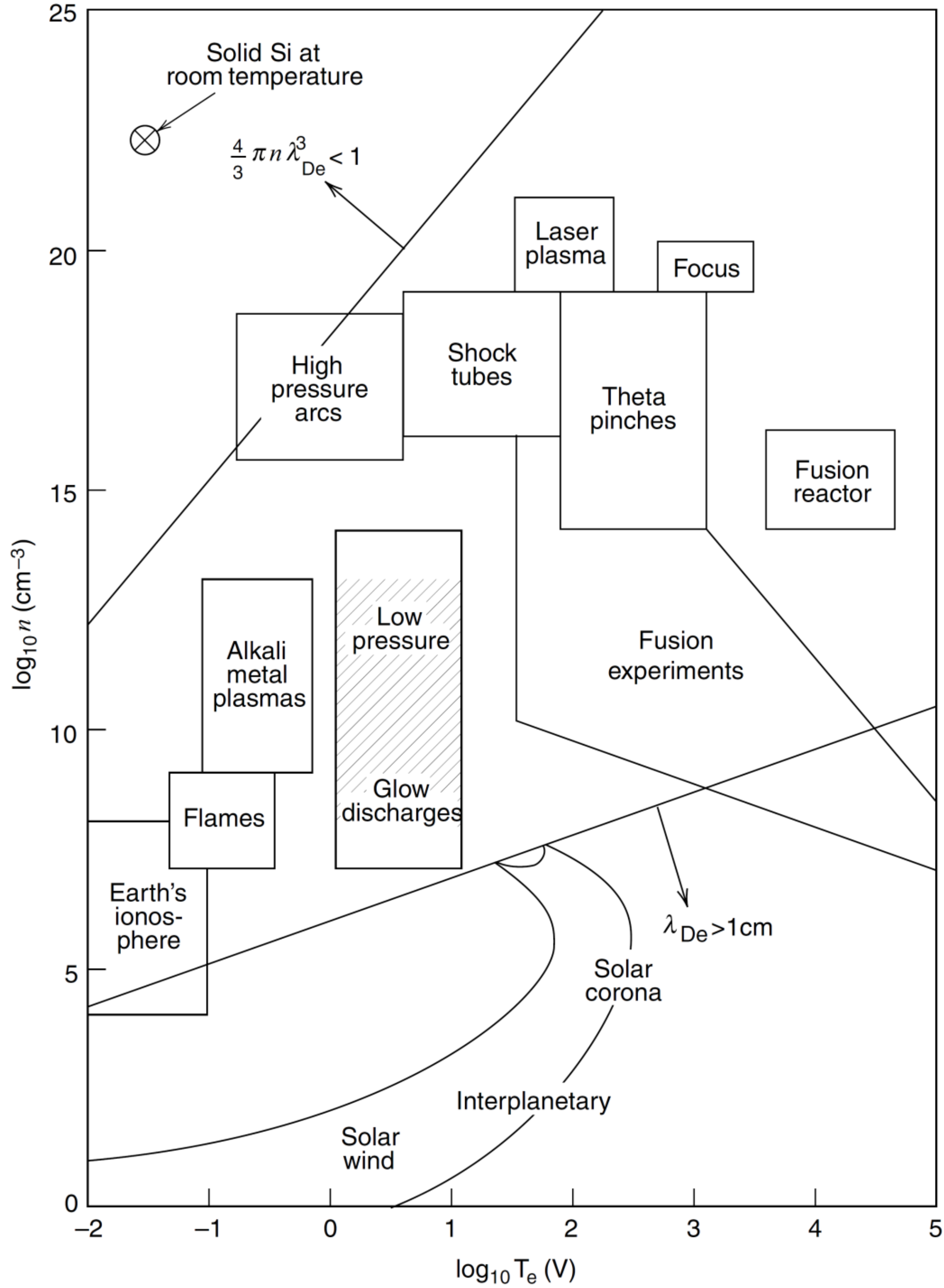

Figure 1.1: Types of plasma discharges as a function of electron densities and electron temperatures where λ_D is the Debye length. Adapted from [2].

1.1.1 Non-equilibrium plasmas

An important consideration, especially in plasma diagnostics, is how far from thermal equilibrium the discharge species are and in what way. Specifically, when spectroscopically studying a plasma (as described in Chapter 3), interpretation of radiation intensities relies on the use of theoretical plasma models. These models describe populations of species in the plasma that are determined by the excitation/de-excitation processes occurring in the discharge. Here, brief descriptions of a few of the more common plasma models used for spectroscopic investigations of plasmas are given:

- *Thermal plasma.* For a thermal plasma, electron and ion/neutral species temperatures are in equilibrium (e.g., the sun, plasma torches, etc.) where $T_e \approx T_{i,n}$. As such, the radiation field may be described by Plank's equation for a black body, the quantum state populations determined by a Boltzmann distribution, and the degree of ionization can be determined by the Saha-Boltzmann equation [4]. This is very rarely the case for laboratory plasmas, as most electrically-driven plasmas are not in equilibrium.

- *The LTE model.* Some high density plasmas ($n_{e^-} \geq 10^{16} cm^{-3}$) may be considered in "local thermodynamic equilibrium" or LTE and is discussed in detail by Griem [5]. In this case, collisional processes dominate the population/de-population of quantum states and radiative processes are not significant. Quantum state population can again be described by Boltzmann and the ionization field by Saha-Boltzmann equations [4].

- *The corona model.* The corona model (named for the solar corona) describes a low-density ($n_e \geq 10^{12} m^{-3}$) non-equilibrium plasma where the electron temperature is high ($\approx 100 eV$) [6] and radiative processes dominate. This coronal equilibrium or

"collisional ionization model" assumes that due to very low densities, upward transitions are due to electron collisions and de-populating or downward transitions are due only to radiative decay [6]. Some low pressure, lower temperature laboratory plasmas fit into this category.

- *CR models.* Collisional-radiative (CR) models are rigorous approaches to bridge the gap between the corona and LTE approximation models and assume no specific equilibrium. Here, rate equations for each state of the particle and coupling to other particles provide a full description of the collisional and radiative processes [6].

As previously mentioned, care must be taken specifically when using optical emission spectroscopy (OES) to probe plasma parameters. OES is a very powerful technique for extracting information about a plasma system without perturbing the discharge. However, since the interpretation of data relies on a deep understanding of the complicated population-depopulation phenomena that result in radiative emission, it is essential to understand which of the above models is appropriate. We do not believe our microplasma discharge to fulfill all the requirements that would allow us to use the LTE or corona approximation models. So, in this work, a simulation package, SPECAIR, that calculates transitions using a collisional-radiative model was used to aid in the characterization of our microplasma source and will be discussed at length in Chapter 3.

1.1.2 DC plasmas

One common (and arguably the most straight-forward) way to generate a lower pressure discharge is to apply a DC high voltage between two plates surrounded by a low pressure gas. The DC glow discharge (see Figure 1.1) describes a class of non-thermal, usually lower pressure plasmas, with $T_e \gg T_{i,n}$. Electron energies are generally assumed to have a Maxwellian energy distribution. Often, the electron temperature is much less

than the threshold energies for ionization and dissociation. Figure 1.2 from [6] provides a good visualization of how the high energy tail of a Maxwellian EEDF will contribute to the ionization in a discharge and how even subtle changes in electron temperature will result in greater excitation rates.

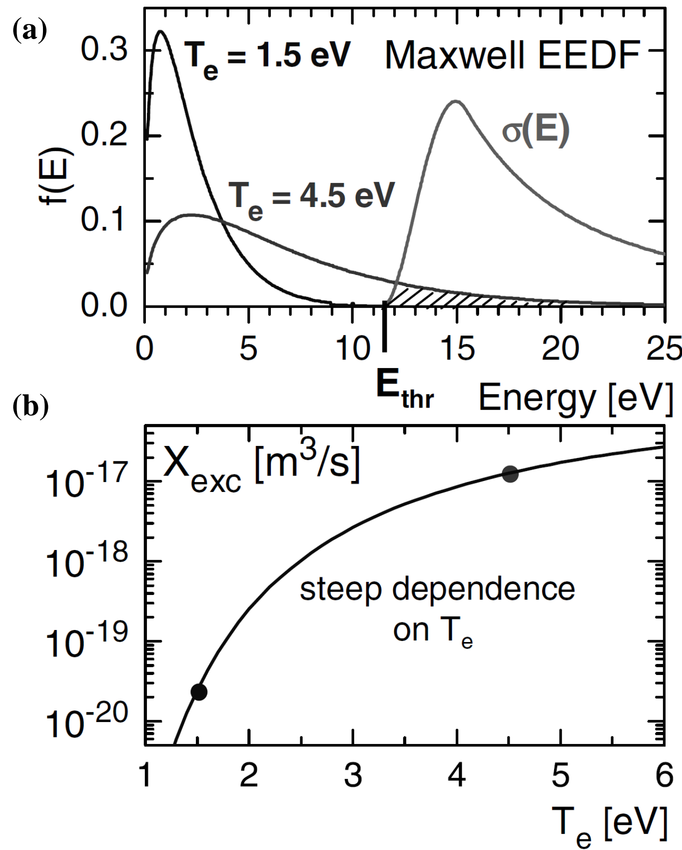

Figure 1.2: (a) shows two Maxwellian electron distribution functions of two T_es, 1.5 and 4.5 eV and an example of a typical cross section for an electron impact excitation process. The excitation rate coefficients of such a process are given in (b) for respective T_es. From [6]

In a simple parallel plate discharge, a low pressure gas fills the region between two electrodes. Breakdown is achieved when a high voltage is applied between these electrodes and an ionization cascade is initiated. That is, when a natural ionization event (generally due to a cosmic ray) occurs in this electric field, the created free electron is

accelerated by the field, resulting in more collisions and more free electrons. This ionization cascade is sustained due to the applied electric field. This phenomenon is commonly referred to as an "avalanche breakdown" or a Townsend discharge. Figure 1.4 shows a representation of this type of parallel plate discharge with all the characteristic regions labeled. Electrical breakdown of the gas only occurs when the necessary breakdown voltage is applied between the parallel plates. The breakdown voltage is largely dependent on the spacing between the plates and the pressure of the gas. Paschen's law describes the required breakdown voltage as

$$V_B = \frac{Bpd}{ln(Apd) - ln\left[ln\left(1 + \frac{1}{\gamma_e}\right)\right]} \tag{1.1}$$

where B is related to excitation and ionization energies, p is discharge pressure, d is the gap distance, A is the saturation ionization in the gas, and γ_e is the secondary-electron emission coefficient [2]. A plot of the breakdown voltages of various gases as a function of the pd parameter is shown in Figure 1.3. This parameter is useful for describing discharges as well as scaling them. As will be discussed later, by decreasing d, achieving breakdown is possible at higher pressures and is the fundamental reason why microplasmas are able to operate at much higher pressures.

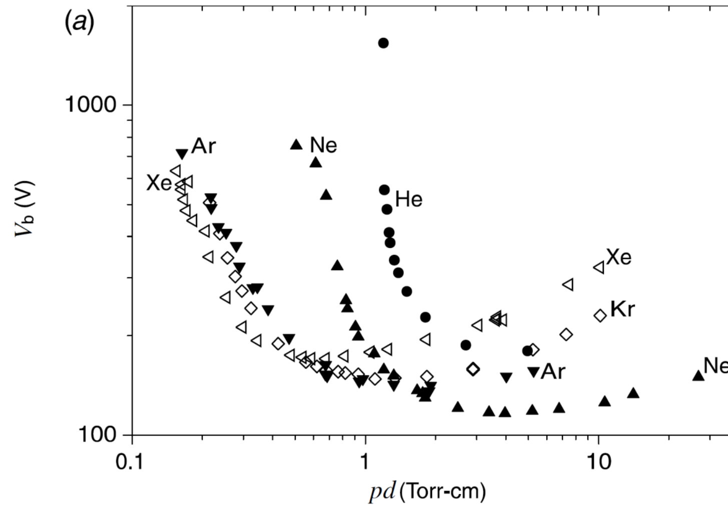

Figure 1.3: Breakdown voltage curves as a function of *pd*, as given by [2]

Another important consideration in plasma behavior is how a discharge interacts with an object - this can be a counter electrode, a Langmuir probe, or even the walls of the vacuum chamber. These surfaces will charge slightly negative resulting in a positive "sheath" surrounding it. A sheath is a layer that forms on a surface that is in contact with a plasma - this layer has a greater density of positive charges that balances the accumulated negative charge at the surface. This phenomenon arises from the greater relative mobility of electrons than ions, which results in more electron collisions at the surface and thus an accumulation of negative charge with respect to the rest of the plasma. The length scale of a plasma sheath is often described in terms of the Debye length.

In the schematic of the DC glow discharge (Figure 1.4), we note significant variation in the appearance, electric potential, and electron an ion concentrations between the two plates and this distribution depends on many factors. One way of quantifying the length scales over which variations in plasmas occur is the Debye length, λ_D. That is, λ_D

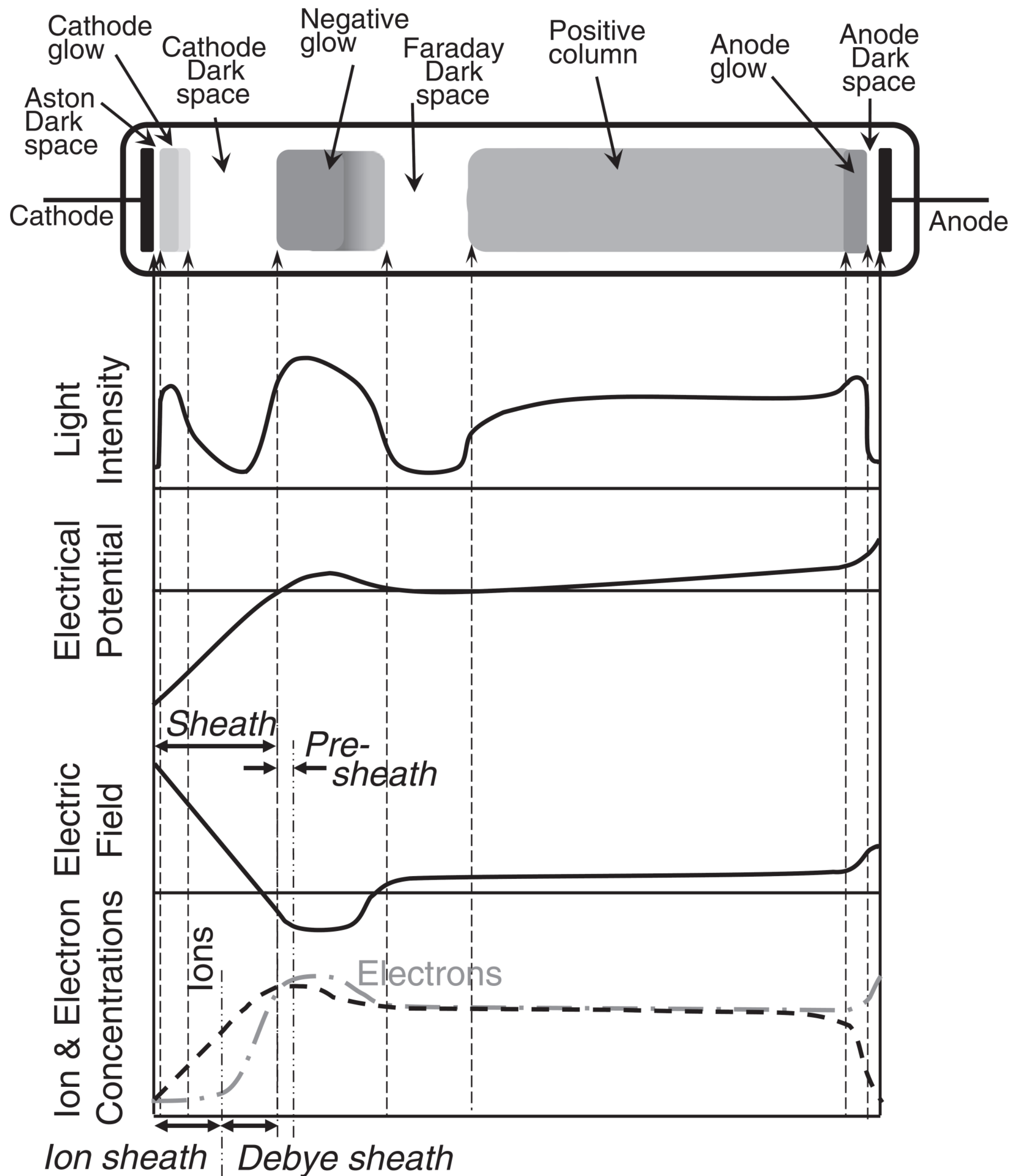

Figure 1.4: Schematic of a DC glow discharge and the resulting light intensities, electrical potentials, and ion and electron concentrations in the different characteristic regions of the discharge [7].

describes how much an electrical disturbance is screened by the plasma space charge [1]. The Debye length λ_D can be written as

$$\lambda_D = \sqrt{\frac{\epsilon_0 k_B T_e}{n_e e^2}} \tag{1.2}$$

where ϵ_0 is permittivity of free space, k_B is the Boltzmann constant, T_e is the electron temperature, n_e is the electron density, and e is the charge of an electron [1]. From this, we see that λ_D will decrease with increasing electron density (n_e) and decreasing T_e. Note that this is only valid when $T_e \gg T_{i,n}$ and $n_e \approx n_i$ [7]. This relationship describes the variations in space charge of a bulk plasma between two parallel plates in Figure 1.4, but also is a very important concept for understanding how plasmas interact with surfaces, such as Langmuir probes as discussed in Chapter 3.

Sheath formation at the cathode and anode of a simple DC glow discharge are shown schematically in Figure 1.4. The thickness of sheaths will depend on various plasma parameters such as the discharge potential (V_p), T_e, T_i, and whether or not the sheath is collisionless or with collisions (low or high pressure), and is typically on the order of several Debye lengths for low-pressure discharges [7]. Sheath thickness is often described with the Child-Langmuir law given as

$$s = \frac{\sqrt{2}}{3} \lambda_D \left(\frac{2V_p}{T_e} \right)^{3/4} \tag{1.3}$$

where s is the sheath thickness, and V_p is the plasma potential [3]. (This law is also commonly expressed in terms of the space-charge limited current flow between two plates with V_p between them and this is referred to as the "3/2 power law".) Understanding the nature of DC sheaths is important in understanding the plasma discharge structure but are also is important in probe diagnostics and will be discussed more in Chapter 3.

1.1.3 Hollow cathode and microhollow cathode discharges

Hollow cathode discharges describe a class of non-thermal plasmas that share many of the same features as the simple parallel plate discharge described above, but are ones in which the cathode geometry has been modified. For one, the cathode dimensions are decreased, usually on the order of centimeters for hollow cathodes and to sub-milimeter dimensions for microhollow cathodes, allowing for gas breakdown and higher pressure operation (Paschen's law above). Secondly, hollow cathodes can be cavities, trenches, parallel plates, or flow-through cylinders, the latter being the focus of this work [8, 9]. The discharge is struck between the hollow cathode and some remote anode. In the case of the cylindrical geometry, similar plasma structures observed in the parallel plate discharge are observed and shown schematically in Figure 1.5 [7]. A sheath and negative glow region are still observed, but extends radially inside the cylindrical cathode which leads to features unique to plasmas generated in this geometry. Specifically, it gives rise to the oscillatory motion of electrons between the opposite cathode walls. This behavior is called the "Pendel effect" or "pendulum trapping" of electrons [10] and results in a significant increase in ionization events due to both secondary electron generation as well as from electron emission as a result of photon and metastable bombardment of the cathode [7].

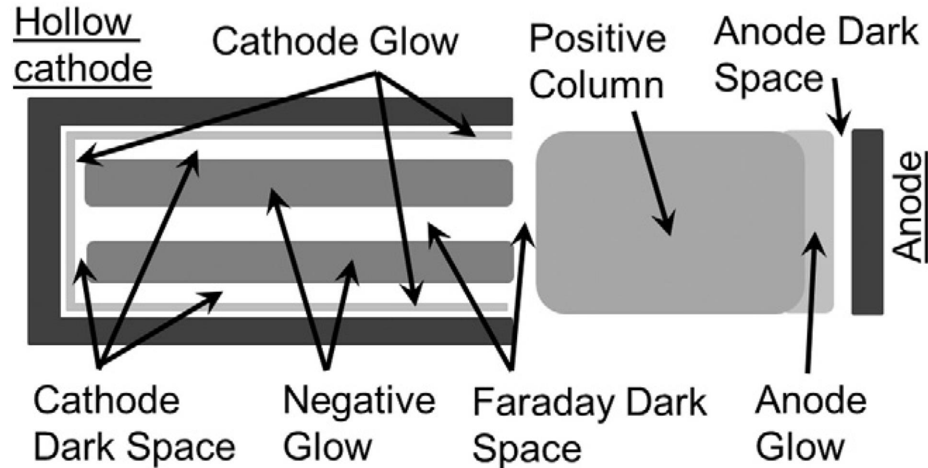

Figure 1.5: Schematic of a DC hollow cathode discharge [7]

The result of this unique environment is the formation of high energy electrons. Hollow cathode discharges are generally assumed to have two groups of electrons: (1) a lower energy population that has a Maxwellian velocity distribution and (2) a much smaller population with a higher energy [7]. Hashiguichi and Hasikuni developed a hollow cathode model assuming two electron temperatures that they termed a two-temperature collisional radiative model (see [11] for more detail). The result is the formation of a high density plasma within the hollow cathode - the perfect environment for driving chemical reactions. Specifically, the enhanced collision rate inside the hollow cathode makes this an ideal platform for chemical vapor deposition, or CVD-like processes, as precursor molecules are more likely to be broken down into reactive growth species. The work to be presented in this thesis focuses on the use of microhollow cathode discharges (MHCDs), or "microplasmas" for this purpose.

1.2 MHCDs for materials deposition and synthesis: A review of previous work

MHCDs are high-density, non-thermal, miniature plasma sources, and they have been used to synthesize a wide variety of materials including semiconductor, metallic, and oxide nanoparticles, thin films, and vertically-aligned nanowires/nanostructures. Many of these systems operatate at atmospheric pressure. These synthesis/deposition plasma sources are usually designed as flow-through systems where CVD precursors are dissociated or a metal is sputtered and a reactive spray of growth precursors is directed toward a collection or deposition substrate [12–14]. The majority of previous work has focused on the synthesis of nanoparticles using microplasmas.

1.2.1 Nanoparticle synthesis

The synthesis of nanoparticles using microplasmas is usually achieved in one of the following ways: (1) cracking of CVD precursors, (2) sputtering of a metal cathode, or (3) via the electrochemical reduction of metal ions in solution, all using a non-thermal, often atmospheric pressure microplasma source. The electrochemical reduction of species via microplasma jet simply entails generating a microplasma between a hollow cathode and reasonably conductive solution containing metal ions. The high energy electrons in the plasma discharge rapidly reduce metal species when in conctact with the solution. The result is the rapid precipitation of metallic nanoparticles. The generation of these colloidal nanoparticle slurries has been widely researched for a variety of systems. Bare silver and gold nanoparticles of uniform size have been synthesized using a microplasma jet in contact with a solution containing metal ions for use in surface-enhanced raman spectroscopy (SERS) applications [15, 16]. A gas-phase approach for the production of

bare, monodispersed nickel and iron nanoparticles has also been reported [17]. Here, volatile organometallics are introduced to a continuous-flow, atmospheric pressure microplasma jet, cracked, and the metal centers nucleate into small nanoparticles that are collected down stream. This type of approach has also been used to catalyze the growth of single-wall carbon nanotubes (SWCNTs) at the nanoparticle surface post-microplasma synthesis [18]. The direct synthesis of 1-3 nm diameter luminescent Si nanoparticles from a silane/Ar flow-through microplasma has also been shown [19]. It is perhaps surprising at first glance that (1) such tight control over nanoparticle size can be achieved in the chaotic environment of a non-thermal plasma seeded with organometallics, and (2) highly crystalline nanoparticles can be created in a low temperature, non-thermal plasma discharge. Both of these phenomena have been widely studied.

Nanoparticle charging

The control of size and monodispersity of nanoparticles synthesized in a plasma has largely been attributed to nanoparticle charging. Recall that electrical "sheaths" form at all solid surface-plasma interfaces due to the large thermal speed of electrons, and this includes a plasma-nanoparticle interface. When nanoparticles are in contact with a non-thermal plasma, they will take on a slight negative charge with respect to the rest of the bulk plasma [14]. Before microplasma-based nanoparticle synthesis gained momentum, there was great interest and effort put into understanding the charging and evolution of particles in a plasma or in an area known as "dusty" plasmas . Particle generation and evolution was and is of great interest in industry where particles in discharges are usually contaminates [20]. These researchers developed models using modified versions of the orbital motion limited (OML) theory to describe how electrons and ions will interact with a charged particle (see [14] for an excellent summary of work in this field as it pertains to nanoparticle charging in plasmas).

Practically speaking, these models approximate the negative potential at nanoparticle surfaces in a flowing plasma to be on the order of a few volts [14]. As such, Coulomb repulsion between the negatively charged particles prevents aggregation and further coalescence, limiting both the size and size distribution of particles. Based on these models, it is hypothesized for some bulk plasmas that during the initial stages of growth, very small particles will be either neutral or singly charged, allowing for further growth. However, after a certain size threshold, the larger particles will charge to a greater extent and further coagulation is hindered. Nanoparticle growth may however continue through surface reactions with the precursor, but not coalescence. It is likely these phenomena will be slightly different in the low pressure, flow-through, microhollow cathode discharge deposition system presented in this work, but the basic idea may guide how we think about processes in our system. Some of these ideas will be revisited in Chapter 5.

Nanoparticle heating

Related to nanoparticle charging in plasmas, low-temperature synthesis of crystalline materials (often generated significantly below the conventional crystallization temperatures) is attributed to preferential particle heating in a plasma [21,22]. This observation has been made in experiment as well as simulation for a few systems. An experimentally observed temperature change of ∼75 K in magnesium fluorogermanate particles above the gas temperature after being introduced to a low pressure non-thermal plasma has been reported. The crystallization of silicon nanoparticles in microplasmas has also been investigated. Askari *et. al.* showed that in an atmospheric pressure microplasma with $T_{gas} \sim 490$K, Si nanoparticles of 4 nm, 6 nm, 8 nm, and 10 nm can heat to 773 K, 1073 K, 1173 K, and 1273 K, respectively [22]. This selective heating is attributed to ion/-electron fluxes reaching the surface of the particle as well as exothermic surface reactions occurring at the particle surface. Figure 1.6 shows how a particle may charge and heat

under various plasma conditions. Another important observation made in this body of research is that there are significant differences in how particles selectively heat in low pressure versus atmospheric pressure plasmas. Specifically, particles will cool faster at higher pressures due to the increased conductive heat transfer. As such, particles formed in low pressure plasmas heat to a higher degree given the slower conductive cooling at low pressures [23]. While there is very limited research into whether or not these observations for nanoparticle synthesis in a microplasma environment hold true for thin film deposition, we believe these observations are relevant to our work.

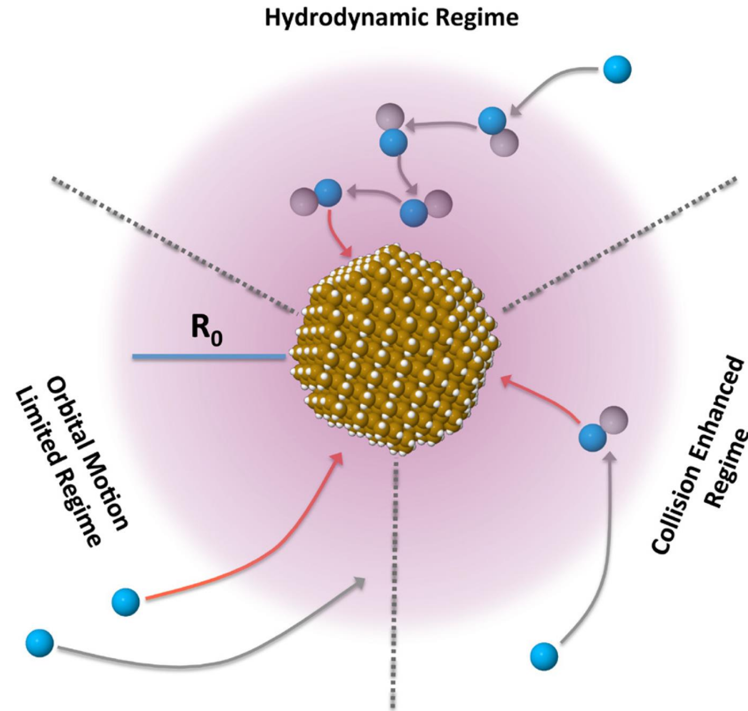

Figure 1.6: Illustration from [23] showing three collisional regimes that are considered in nanoparticle heating and charging models where R_0 is the “capture radius” wherein these collisions occur.

1.2.2 Thin film deposition

Using microplasmas for thin film and vertically aligned nanostructure deposition has not been as extensively explored as nanoparticle synthesis. However, when compared to other common materials deposition methods, we see that low-pressure microplasma jets exhibit locally high deposition rates and operate at higher pressures. Figure 1.7 shows where microhollow cathode discharge sources fall in comparison with other thin film deposition techniques in terms of operating pressures (Torr) and deposition rates (nm/min).

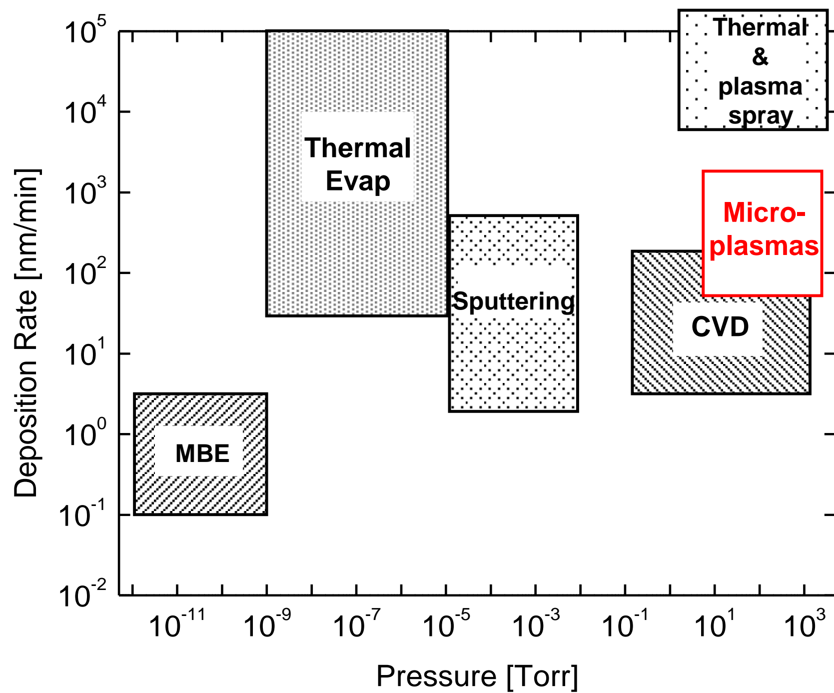

Figure 1.7: Common deposition techniques and their respective deposition rates and operating pressures.

Koh and Gordon reported a general synthesis route to a variety of metallic and transition metal oxide materials using a hydrodynamically-stabilized high pressure microplasma jets. Here, organometallic precursors were sublimed and injected into a mi-

crohollow cathode discharge operating a high pressures and in an Ar/H_2 or Ar/O_2 background. Specifically, deposition of Cu, Pd, and Ni metal thin films, CuO, PdO, and NiO nanostructured oxide films has been demonstrated [24–27]. Additionally, Pebley *et. al.* directly deposited nanogranular, biphasic metal oxide thin films using a low pressure, supersonic microplasma seeded with CVD presursors. Specifically, the growth of $NiFe_2O_4$-NiO biphasic films was demonstrated for use in exchange bias and magnetic storage applications [28, 29]. The ability to tune dopant levels in an Fe-doped NiO electrocatalyst for use in the oxygen reduction reaction [30] was also shown.

Structure-zone models

There have not been many mechanistic inquiries into the plasma-based deposition or growth of aligned nanostructures. This might partially be due to the fact that aligned nanostructures are rarely seen in most CVD processes. However, several authors have noted general trends during dense metal film deposition that align with observations made during the CVD-like metal film deposition conducted by Koh [26]. For example, Thornton's "structure-zone" model [31] describes the resulting morphology of metal films deposited at high rates (100 nm/min) under different pressures and substrate temperatures. In the original work, Thornton used a large hollow cathode discharge with the metal cathode acting as the sputtering source. The sputtered cathode was deposited onto substrates located within the discharge. The model describes how the fate of impinging nuclei during deposition is largely a function of substrate temperature and deposition pressure. The contributing factors being the incident flux, density of surface sites, and adatom mobility [31]. The resulting morphologies observed are summarized in Figure 1.8.

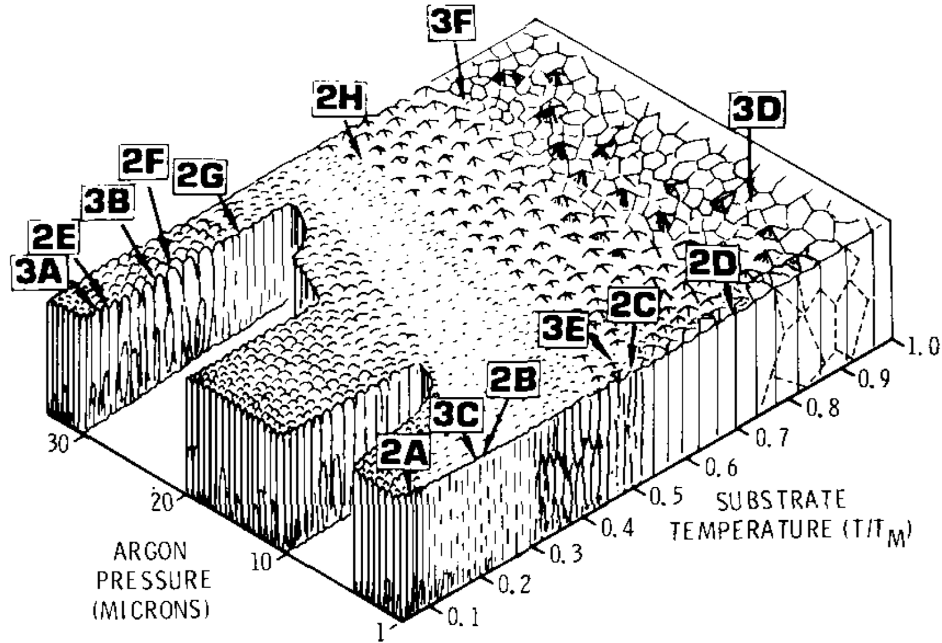

Figure 1.8: A structure-zone model showing various film morphologies obtained where T/T_m is the substrate temperature and T_m is the melting point of the material.

Overall, its noted that at low T/T_m values, there is little adatom mobility and the resulting morphology is a matchstick-like structures with tapered crystallites (2A region in Figure 1.8). As the substrate temperature is increased ($> T/T_m$ value), diffusion is more likely and coalescence is possible during growth, and at very high T/T_m values, surface mobility is great enough to encourage grain boundary migration and recrystallization (3D region of Figure 1.8) [31]. While this is certainly not describing the CVD-like deposition process when using a microhollow cathode and organometllic precursors, there are similarities noted in the morphology evolution in microplasma deposits. Moreover, while the work presented in this thesis largely does not make use of a heated substrate, we

have established in this chapter that nanoparticles/clusters within the plasma, and thus nanoparticles/clusters impinging on a substrate, will likely have the thermal mobility to support some surface diffusion, which we believe is evident in the crystalline structures we observe.

1.3 Thesis overview

The design, construction, and characterization of a novel microplasma-jet based deposition source are presented in this thesis, along with application of this new synthesis tool to deposit nanostructured thin film materials for electrochemical energy storage. The deposition source is based on a flow-through, micro-hollow cathode plasma discharge and uses volatile organometallic precursors to spray deposit high surface area, nanostructured metal oxides on virtually any surface. This thesis is organized as follows:

- Chapter 1 provides an overview of plasma physics and introduces the reader to plasma-based materials processing;
- Chapter 2 highlights the fundamental fluid mechanics and plasma physics associated with micro-hollow cathode discharges (MHCDs), discusses their unique operational characteristics, and details the design and construction of the flow-through MHCD plasma source and deposition system developed in this work;
- Chapter 3 looks more deeply at the microplasma jet itself, with focus on optical emission spectroscopy (OES) and double Langmuir probe (DLP) electrical characterization of the source to determine the rotational, vibrational, and electron temperatures of the jet;
- Chapter 4 provides a demonstration of how the microplasma jet source can be used to deposit a wide variety of nanostructured and mixed metal oxides on virtually any

substrate, along with detailed materials characterization (e.g., SEM/TEM, XPS, CV) of the resulting films and application to batteries;

- Chapter 5 focuses on the importance of the electrical configurations of the plasma drive circuit and sample (e.g., related to sample charging for conducting vs. insulating substrates and a grounded vs. floating deposition chuck) insofar as they directly affect the resulting film morphology, crystallinity, composition, and contamination; and finally,

- Chapter 6 shows how microplasma jet deposition can be combined with standard microelectronics foundry techniques to realize electrochemical energy storage devices, namely NiO-carbon fiber based pseudocapacitors and MnO_2-based microsupercapacitors for on chip energy storage.

Chapter 2

Microhollow cathode discharge-based plasma deposition system

An overview of the flow-stabilized microhollow cathode discharge-based (microplasma-based) source and reactor system used for spray deposition of nanostructured thin films is presented. The goal is to provide a practical description of the reactor components and provide enough detail to guide future work. The reactor design is an extension of that described by Koh [24, 25, 27] and Pebley [28–30] with added plasma diagnostics capabilities, including Langmuir probes and optical emission spectroscopy.

2.1 Microhollow cathode discharge (MHCD) source

The microhollow cathode discharge (MHCD) source at the heart of the plasma spray deposition system is shown in Fig. 2.1. The discharge is struck by applying a negative DC high voltage (800-2000 V to strike; 300V to sustain) between a stainless steel capillary

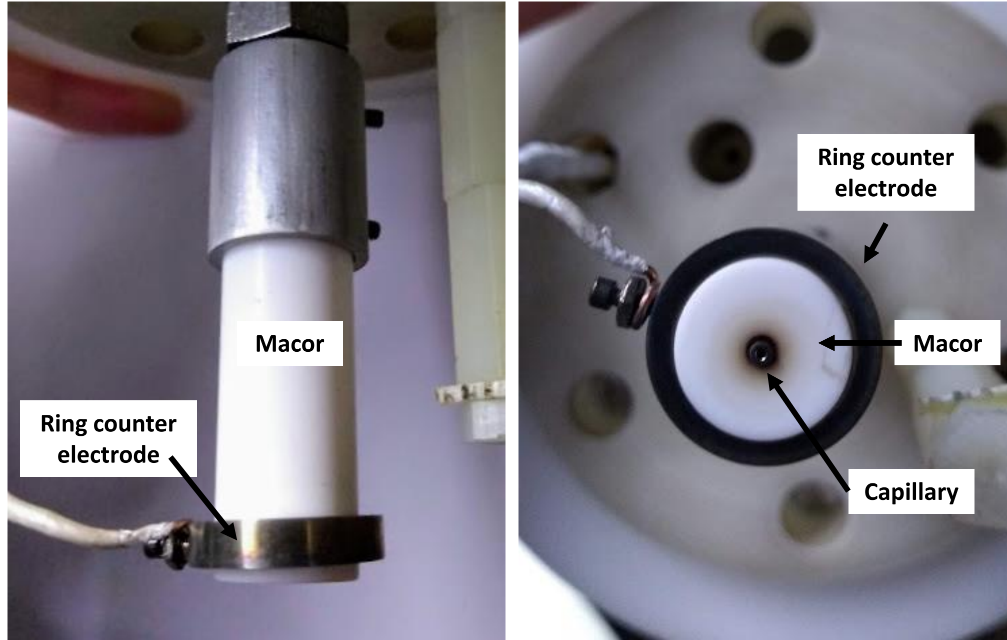

Figure 2.1: Photographs of the Macor-housed hollow cathode capillary and ring counter electrode

(usually ID 500 μm and housed in a Macor insulator) and a remote counter electrode with a current-regulated high voltage power supply (Glassman, Series EW). The ceramic insulator surrounding the capillary prevents arcs and insures a uniform discharge. A constant flow of Ar (50-300 sccm) is introduced to the capillary, and when high voltage is applied, gas breakdown occurs, forming a stable, high density plasma in and near the capillary tube exit.

2.1.1 Plasma circuit

The plasma HV circuit is completed to a grounded anode, which can be a (conductive) substrate or the deposition chuck downstream of the capillary exit, or alternatively to the aforementioned remote ring anode, as depicted in Fig. 2.2. The ring anode configuration

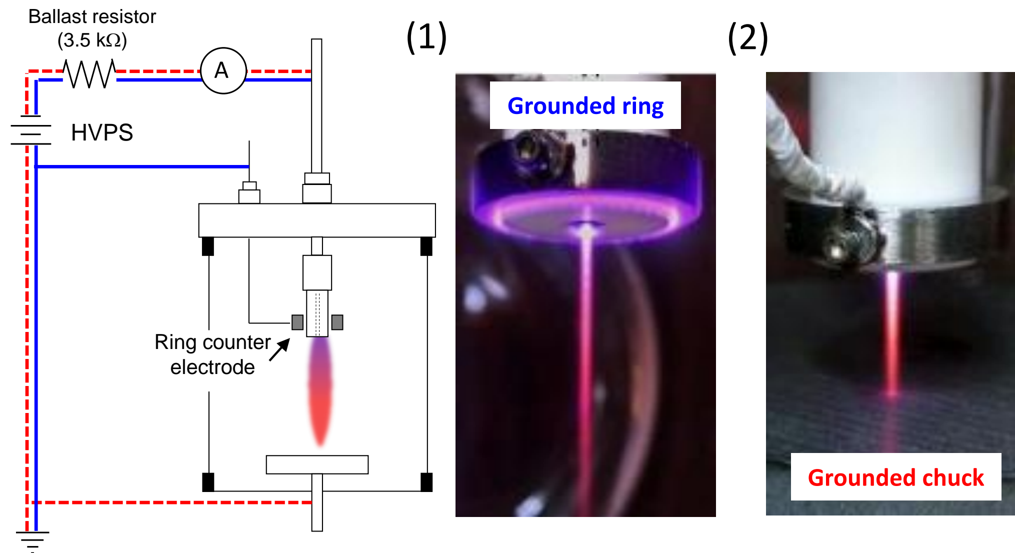

Figure 2.2: Schematic of the electrical configuration of the MHCD source. The discharge is struck between the capillary and a remote counterelectrode (anode), which can be a grounded ring (1) or the sample substrate/deposition chuck itself (2). A slight glow, due to emission of excited Ar neutrals and ions, is visible around the ring electrode where high energy electrons are collected.

was predominantly used in this work, as the metal oxides being deposited often resulted in substrate charging and unstable source operation; the influence of anode configuration is discussed in more detail in Chapter 5. The electrical configuration of the anode, i.e., using the ring anode versus completing the plasma through the sample itself, was seen to not appreciably change the morphology of the deposited films for many material systems. However, it was observed that sample uniformity was much better when using the ring anode and an electrically floating sample substrate. Moreover, the ring anode allowed deposition of insulating films and deposition on insulating substrates, such as glass, polymers, and woven fibers, as well as independent biasing of the substrate for plasma IV measurements.

2.2 Fluid mechanics of the MHCD (microplasma) jet source

In a typical deposition, an MFC-regulated flow of Ar gas (100-300 sccm) is introduced to the stainless steel capillary tube (ID 50-500 μm) situated above the deposition chuck. The deposition chamber is pumped with a rotary vane pump and throttled to 10-50 Torr, where the chamber pressure is monitored with a Terranova 808 Si diaphragm vacuum sensor. The MFC-regulated flows and pressure sensor readouts are monitored in real time with LabVIEW.

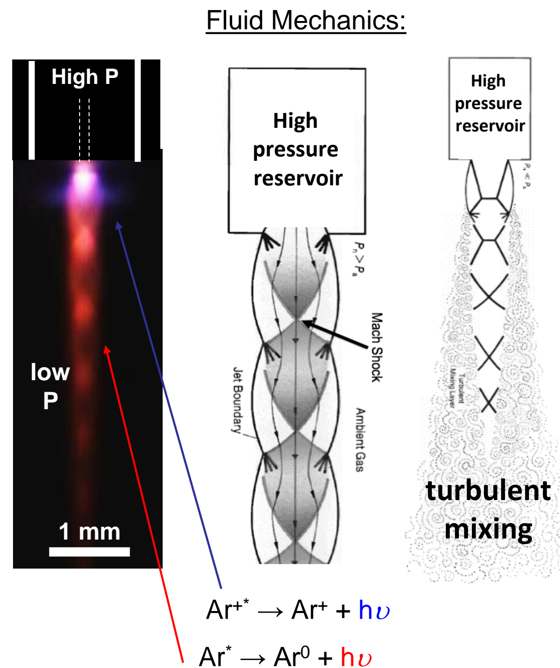

Figure 2.3: Microplasma jet operating at 10 Torr with characteristic shock diamonds typical of a supersonic gas expansion. The blue and red emissions are caused by decay of excited ions and neutrals, respectively. Ar flow was 150 sccm with 9 mA plasma current.

The Ar pressure upstream of the capillary has been measured to be on the order of 300 Torr. The result is a supersonic (>300m/s) gas expansion into vacuum from a

high pressure reservoir, resulting in characteristic shock structures [26]. These standing shock waves are ultimately eroded by interactions with the background gas, resulting in turbulent mixing downstream of the capillary exit. Figure 2.3 depicts an Ar microplasma operating at 10 Torr in which a supersonic expansion from a high pressure reservoir into a low pressure background with characteristic shock diamonds can be clearly seen. Deposition within the standoff shocks and stagnation regions has been studied and reported [26]; in the present work, all depositions were conducted with the substrate in the turbulent wake (well mixed) zone ($>$ 5 mm from the capillary exit) to avoid flux nonuniformities.

The fluid flow characteristics of the plasma jet system were examined by evaluating the Reynolds number and pressure corresponding to sonic flow at the capillary tube exit. For our case of compressible flow, the system Re is given by [32]:

$$Re = \frac{Q_m}{\pi R \mu} \tag{2.1}$$

where Q_m is the mass flow rate, R is the capillary radius, and μ is the gas viscosity. Using a 100 sccm Ar feed to a 500 μm ID capillary, the system Re varies from 75 to 150, assuming that the gas exiting the capillary is at 673 or 300K, respectively. As such, the flow exiting the capillary is indeed laminar and sonic or supersonic. The pressure (Pc) corresponding to sonic flow at the capillary exit was also evaluated assuming an adiabatic expansion via:

$$P_c = \frac{Q_m}{\pi R^2}\sqrt{\frac{kT_g}{\gamma M}} \tag{2.2}$$

Where γ = C_p/C_v = 1.67 for Ar, M_Ar = 40 g/mol, and T_g is the effective gas temperature. Although the gas temperature is unknown (see Ch. 3 for details on OES measurement of T_g), the adiabatic sound velocities for Ar range from 190 to 350 m/s for gas temperatures of 300-1000 K, yielding sonic flow pressures of 220 to 400 Torr,

respectively. These values are on the same order as the pressures measured upstream of the capillary (300 Torr).

The aforementioned calculations thus suggest that the flow exiting the capillary is laminar and supersonic, and moreover, support the idea that the flow inside the capillary tube is totally decoupled from the flow outside. As such, given that the downstream chamber pressure is in the 10s of Torr range, it is unlikely that the chamber pressure significantly affects the flow, and plasma, *inside* the capillary.

2.3 MHCD-based plasma jet deposition system

Figure 4.1 shows how these flow-through microplasma sources are used for materials deposition. Sublimed chemical vapor deposition (CVD) organometallic precursors are entrained in a heated Ar flow and are injected into the microplasma jet. The metal complexes are cracked in the energetic plasma environment inside the hollow cathode, forming active growth species such as ions, neutrals, and clusters. Reactive gases such as H_2 or O_2 are also added to the chamber background or directly in the plasma gas feed to further reduce or oxidize the precursor, as well as scavenge carbon species. These active, metal-containing species react with one another and/or the background gas, but given the short space-time (μs) in the plasma zone and rapid drop is gas density associated with supersonic expansion, particle growth and aggregation are quenched. The end result is a directed flux of active growth species that are subsequently spray deposited onto a surface.

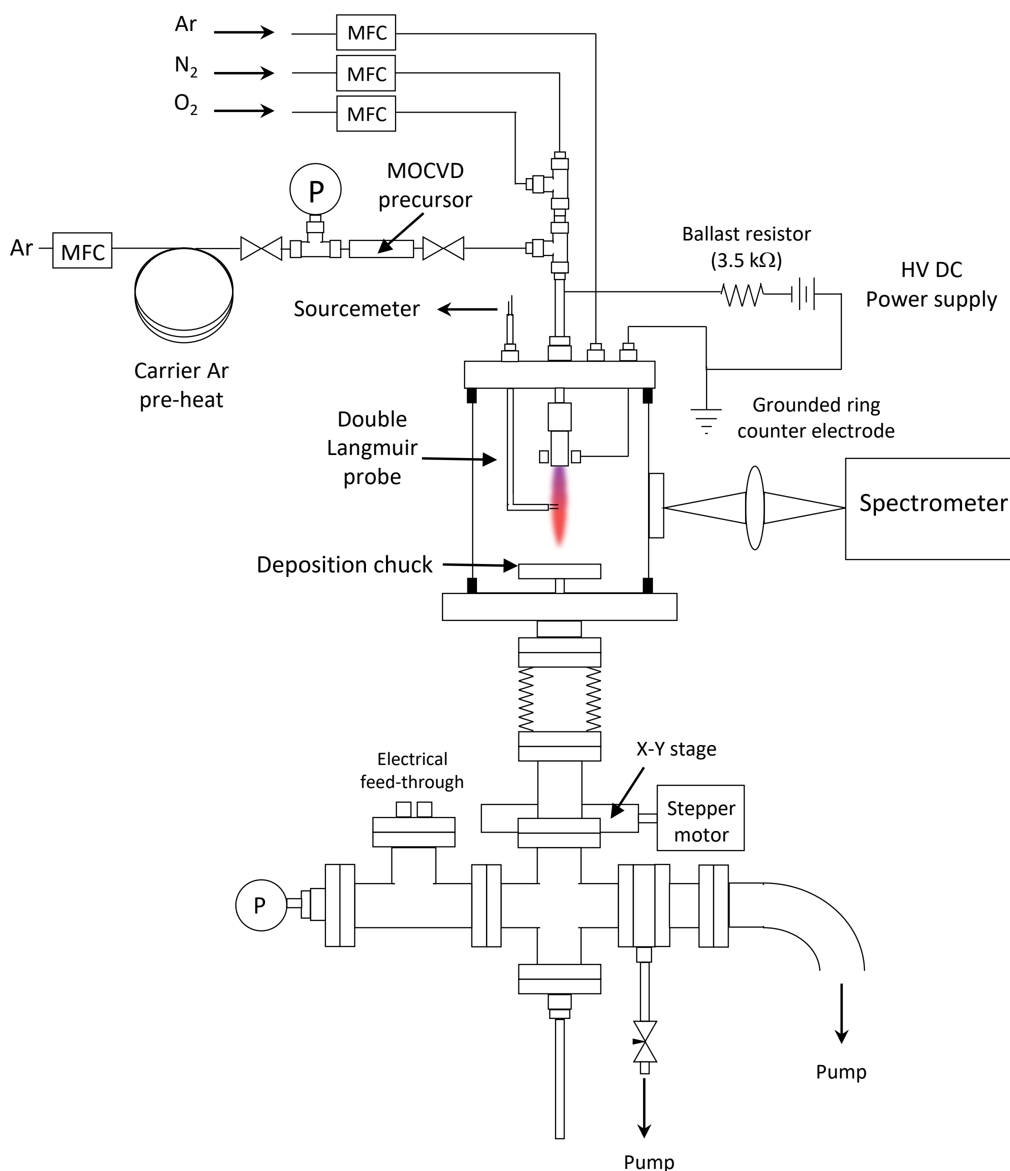

Figure 2.4: Schematic of the microplasma jet deposition system. Ar carrier gas and sublimed organometallic precursor(s) are introduced into a stainless steel capillary inside a macor insulator with ring anode. A hollow cathode DC microplasma is struck between the capillary and ring anode (or the substrate) using a current-regulated, high voltage power supply (HVPS). MFC = mass flow controller.

2.3.1 Precursor chemistry

The nanostructured films discussed in this work were deposited using common CVD precursors (STREM Chemicals). Metal cyclopentadienyls and β-diketonates were of interest herein, due to their high vapor pressures, thermal stability, and adaptable chemical functionality (i.e., substituting CF_3- for CH_3- groups on acetylacetonates (acacs) to increase volatility). Vapor pressures and decomposition pathways of of many of the these precursors can be found in [33–36].

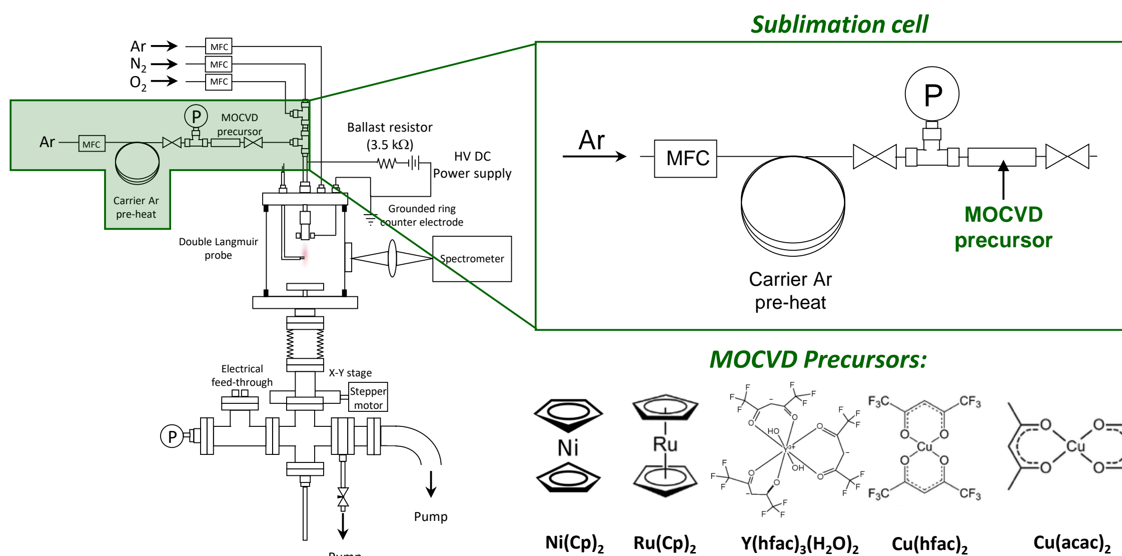

Figure 2.5: Solid organometallic precursors, 1-2g packed inside an NPT pipe nipple with quartz wool, were sublimed at controlled temperature, entrained in Ar carrier gas (XX-YY sccm), and delivered to the plasma jet through heat-traced lines to avoid precursor condensation. In some cases, precursors cells were cooled below room temperature in a freezer and back-heated to a constant temperature (5-15 C) using heat tape and a PID temperature controller. Chemical structures of several of the precursors used in this work are shown.

The relative flux of organometallic precursors to plasma discharge, as well as O_2 addition to the plasma feed and/or chamber background, significantly affected the resulting film morphology as well as C and F contamination levels. This was especially true for some metal cyclopentadienyls with high vapor pressures (e.g., nickelocene, ferrocene,

and cobaltocene), necessitating temperature-controlled cooling of their respective sublimation cells below room temperature (2-15 C). Under optimized growth conditions, C and F contamination were found to be minimal, e.g., < 1 at% (see EDS and XPS studies in Chapters 4 and 5 for more details).

2.3.2 Deposition scale-up

The deposition "footprint" of the microplasma jet is on the order of a few mm^2, and while these small "spot deposits" may be useful for some applications presented in Chapter 6, its often necessary to scale-up the process. To accomplish this, the sample chuck was attached to a stepper motor driven stage via flexible bellows, allowing 3x3 cm^2 deposition areas via raster scanning the sample beneath the fixed plasma jet source. The XY stage was controlled with LabVIEW for point-to-point movements, vector moves at constant velocity, raster-scanning, and direct writing of arbitrary patterns.

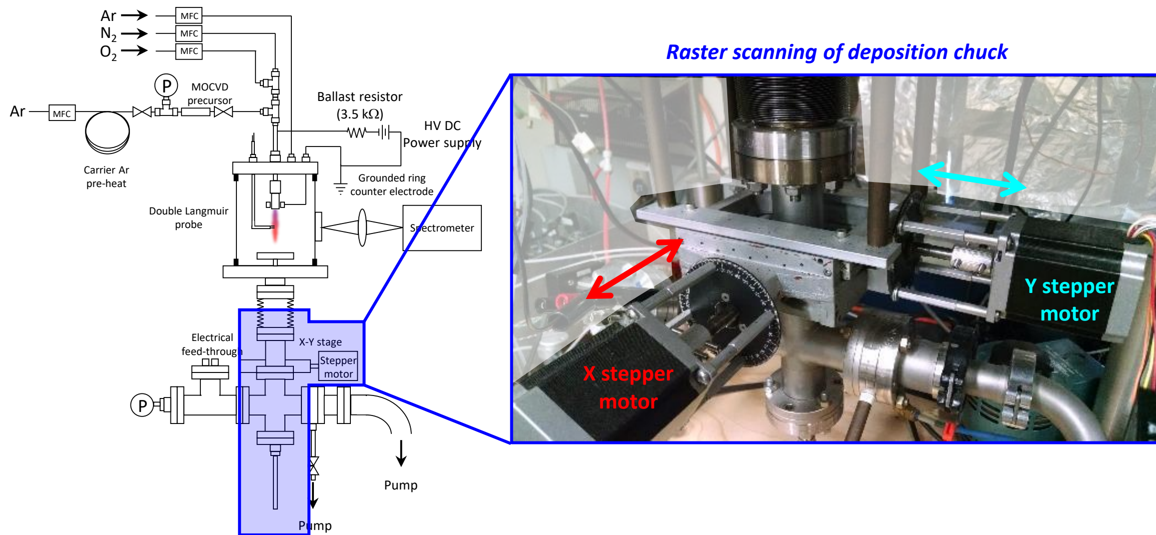

Figure 2.6: Detail of the stepper motor-driven x-y stage to raster scan the deposition chuck under the fixed microplasma jet.

2.4 Plasma diagnostics

The plasma deposition system was outfit with optical emission spectroscopy and Langmuir probe diagnostics (see Figure 2.7) to gain fundamental understanding of the deposition process and plasma parameters of the MHCD. Both the theoretical basics of these diagnostic techniques and the results of these investigations are reported in detail in Chapter 3, but introductory descriptions of the experimental setup is provided here.

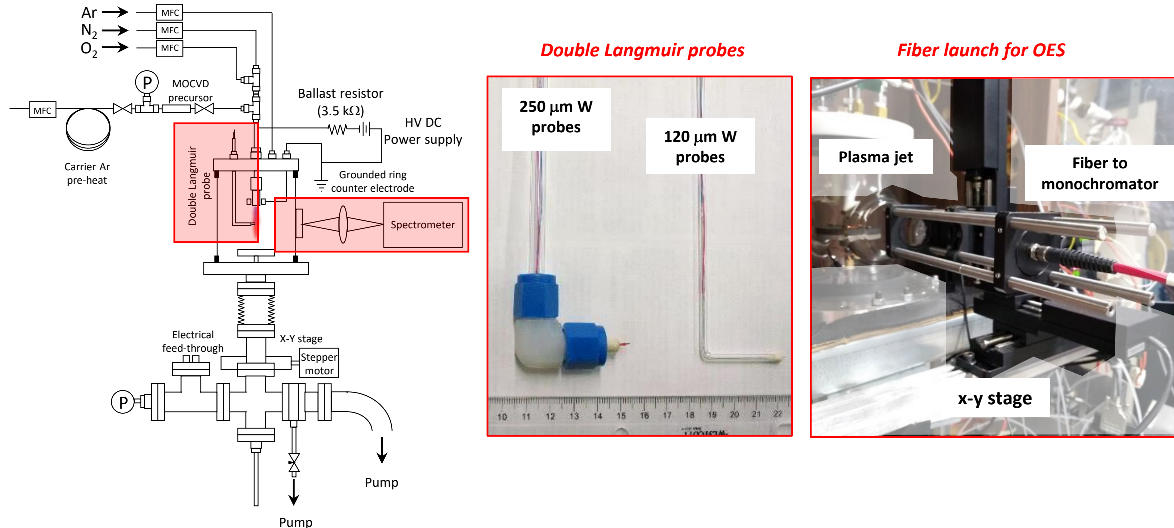

Figure 2.7: Langmuir probe and optical emission spectroscopy (OES) diagnostics on the microplasma jet deposition system. Photos of the double Langmuir probes (250 and 120 mm tungsten probes) and OES collection configuration are shown.

2.4.1 Optical emission spectroscopy

Optical emission spectroscopy (OES) is a powerful, non-invasive technique commonly used to characterize plasmas, e.g., to determine the rotational and vibrational gas temperatures (via N_2 rovibrational transitions), electron temperature (via rare gas actinometry), and even electron density (via Stark broadening spectroscopy). Towards the goal of implementing these methods on the present system, an light collection and spectroscopy

system was set up. Light from the plasma discharge was collected with a 50 mm focal length biconvex lens, coupled to a 500 μm fiber, and sent to a 550 mm focal length Jobin-Yvon iHR550 monochromator with 1800 gv/mm grating and LN2-cooled CCD detector. The collection optics were placed on an xyz alignment stage and the 500 um fiber acted as a spatial filter to limit the light collection volume, i.e., light from the plasma was imaged at 1:1 magnification onto the fiber directly. OES data were analyzed using a variety of semi-empirical and quantum mechanical simulation (SPECAIR software) methods, as discussed in detail in Chapter 3, to determine vibrational, rotational, and translational gas temperatures (T_{vib}, T_{rot}, and T_{trans}).

2.4.2 Langmuir probes

Langmuir probes are ubiquitous in plasma characterization and their use on the present MHCD source will be discussed at length in Chapter 3. Briefly, a metal probe is inserted into the plasma and biased positively or negatively, drawing electron and ion currents from the plasma through the sheath that forms around the probe wire(s). From the I-V characteristics of the probe, parameters such as plasma potential, ion saturation current, electron energy distribution function (EEDF), and electron densities may be determined. In the present case, due to the electrical configuration of the MHCD source (to be discussed in Chapter 3), double Langmuir probes (DLPs) with dual electrodes were required for plasma IV characterization. The design of these probes are schematically shown in Figure 2.8. Dual tungsten wires of various diameters (50, 120, 250 μm) were epoxied into 1/8" diameter glass tubing with 1 mm gap and $\sim$2 mm protrusion into the plasma. The glass tube was then bent at 90 deg and sealed to the vacuum deposition chamber via Cajon o-ring fitting, allowing the probe to be moved both laterally and axially in the plasma jet expansion direction. IV spectroscopy of the plasma was carried

out by connected the DLP to a Keithly 2400 biasable electrometer piloted via LabVIEW.

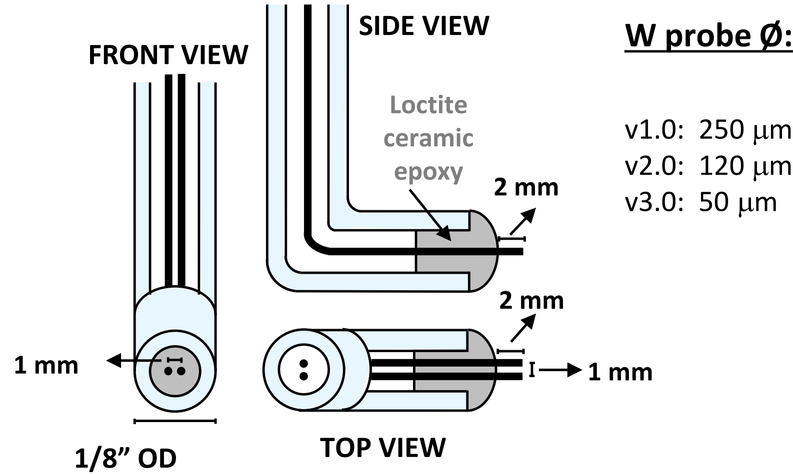

Figure 2.8: Schematic of the double Langmuir probes constructed for electron temperature and density measurements.

2.5 Microplasma deposition systems

The aforementioned plasma system components and characterization apparatus were combined in several generations of depositon reactors, as depicted in Figure 2.9. Reactors were constructed for (1) CuO and MnO_2 deposition, outfit with OES and Langmuir probes, (2) deposition of Ni, Fe, and Co oxide with a heated chuck, and (3) a generic test reactor to quickly evaluate different materials systems, also outfit with a heated deposition chuck. All of the systems were operated in the 5-100 Torr pressure range with MFC-based gas delivery, temperature controlled organometallic precursor sublimation cells, and raster scanning of the sample chuck. All system variables (P, T, etc.), flow control, and stage scanning were automated in LabVIEW.

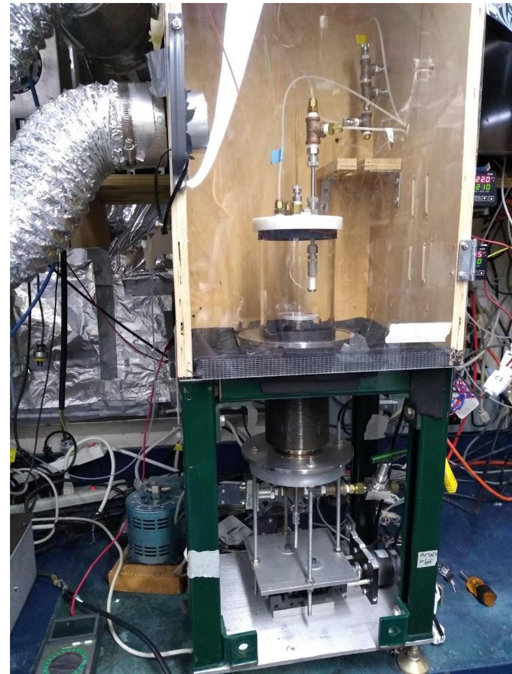

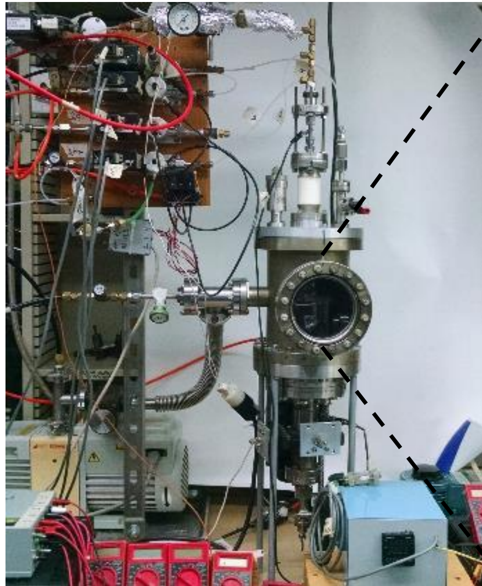

Figure 2.9: Photographs of microplasma reactors used in this work

Chapter 3

Optical emission spectroscopy and Langmuir probe studies of a low pressure microplasma jet deposition source

Micro-hollow cathode discharges (MHCDs), also known as microplasmas, are geometrically confined, high(er) pressure plasma discharges operated over a range of pressures from 10-1000 Torr [8, 9, 37, 38]. These cold plasma sources ($T_{gas} \ll T_e$) have been used in a variety of venues to synthesize and modify all types of materials (see [12, 15, 17, 39] for a review); generate reactive species (e.g., O_3, NO_x) for chemical conversion [40], VOC destruction [41], and plasma medicine [42]; and even to generate hard-UV (eximer) radiation [43]. Static microplasmas formed in small holes and slits at atmospheric pressure have also been characterized extensively using optical emission spectroscopy (OES) and Thomson scattering [44–46].

Low pressure (1-20 Torr) microplasmas, specifically when configured as a flow-through

supersonic plasma "jet", have also been used to spray deposit metal and metal oxide nanostructures and thin film materials on virtually any surface [47]. A wide range of nanostructures, including nanoparticles, rods, wires, aggregates, dense films, and dendritic structures can be realized with such methods [25, 27, 28] and it has been shown that plasma operating conditions, growth precursor, background gas, and supersonic flow characteristics [26] can all influence deposit morphology. However, these low pressure deposition sources have been much less studied, especially from the standpoint of plasma diagnostics.

Here, we present OES and double Langmuir probe (DLP) measurements on these low pressure, flow-through supersonic microplasma jet systems to highlight how plasma operating conditions (e.g., pressure, current, presence of growth precursors / O_2, distance from the nozzle, floating vs. grounded substrate) affect the local gas (T_{rot} and T_{vib}) and electron (T_e) temperatures in the plasma jet plume. T_{rot} and T_{vib} were estimated using semi-empirical and rigorous quantum mechanical fits to OES spectra of the first positive group of N_2 ($B^3\Pi_g \longrightarrow A^3\Sigma_u^+$) and T_e was obtained via fits to DLP IV curves.

3.1 Experimental setup

3.1.1 Microplasma jet deposition source

A schematic depicting the microplasma-based reactor used in this work is shown in Figure 3.1. A microhollow cathode discharge is generated inside a stainless steel capillary tube (ID 500 μm) by applying a DC high voltage between the capillary and a remote anode while a flow of Ar is supplied to the capillary. The remote electrode is typically a conductive deposition substrate/chuck; alternatively, plasma circuit may be completed through a concentric ring anode near the capillary exit (see Chapter 5 and [47] for details),

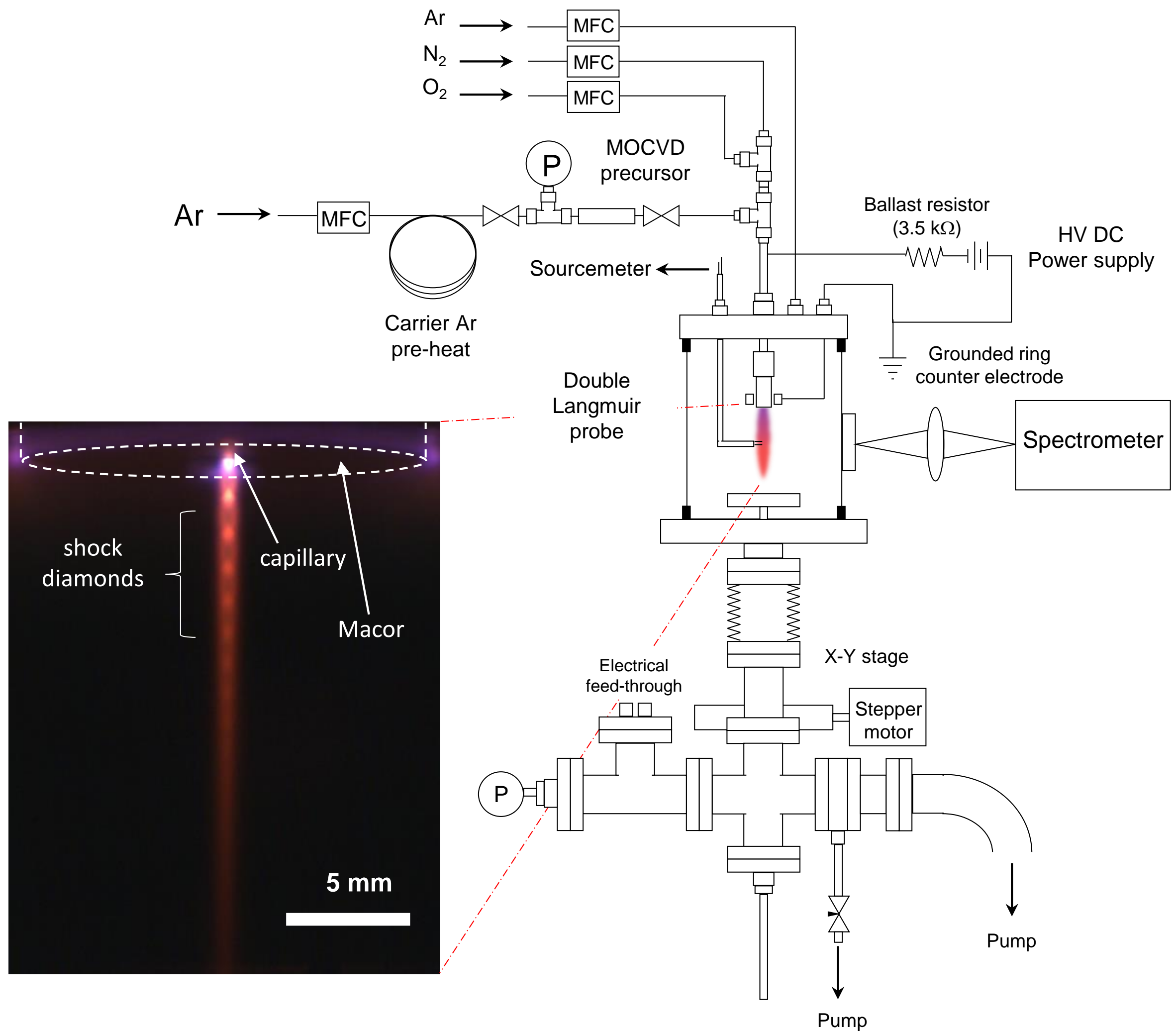

Figure 3.1: Microplasma-based deposition system with OES and DLP capabilities. (Inset) Photograph of an Ar microplasma jet operating at 12 Torr.

allowing for deposition on nearly any substrate. Both plasma circuit configurations were considered here, with the downstream reactor pressure held in the 10-50 Torr range, resulting in supersonic gas expansion within the jet.

3.1.2 Optical emission spectroscopy

Optical emission spectroscopy of rovibrational bands of N_2 was used to estimate the T_{rot} and T_{vib} of the plasma jet plume. A small amount (2.5 %) of N_2 was added to

the plasma jet feed gas and light was collected from various points in the expansion plume using a 75 mm focal length lens coupled to a 500 μm diameter fiber. Spectra were analyzed using a 550 mm focal length monochromator (JY iHR550) with 1200 groove/mm grating and LN2 cooled CCD detector.

The estimation of gas temperature in non-thermal plasmas can be challenging, especially in lower pressure discharges. If rotational-translational relaxation times are sufficiently fast (i.e., high collision frequency allows T_{rot} energy transfer to particles, emitting species have long radiative lifetimes, and if excitation/de-excitation processes are sufficiently slow) [48, 49], then T_{rot} and gas temperature (T_g) can be assumed to be in equilibrium. These constraints guided what portion of the rovibronic spectrum was used for T_g estimation in this work, i.e., the second vs. first positive groups of N_2. The second positive group, namely ($C^3\Pi_u \longrightarrow B^3\Pi_g$), is most often used to determine rotational temperatures in plasmas, but several authors [49, 50] have demonstrated that this is problematic when working with Ar-based discharges for several reasons. For example, fast resonant energy transfer from Ar ($1s_5$) to the N_2 $C^3\Pi_u$ state can occur and moreover, the $C^3\Pi_u$ state has short lifetime (40 ns), making the equilibrium assumption that T_{rot} $\sim T_{gas}$ invalid, especially at lower pressures. To remedy this, a different portion of the N_2 emission spectrum, specifically the first positive system ($B^3\Pi_g \longrightarrow A^3\Sigma_u^+$), was used herein to estimate the rotational temperature. For the 1st positive system specifically, Golubovskij and Telezhko have estimated that T_{rot} and T_{gas} are in equilibrium for plasma discharges at pressures greater than approximately 100 Pa (0.77 Torr) [51].

In the present work, N_2 OES spectra were interpreted using two methods: (i) quantum mechanical fitting of spectra using a commercial plasma spectroscopy simulation software package known as SPECAIR [52], and (ii) semi-empirically using ratios of several rovibrational peaks (at the band head), after the quantum mechanical simulations and methodology of deBenedictis [49]. SPECAIR can simulate a full OES spectrum using

various radiative molecular and atomic transitions of common plasma species (NO, N_2, N, N_2^+, OH, CO, N, O, and C), along with rigorous application of quantum mechanical selection rules and cross-sections. These calculations take into account any Doppler, collisional, Stark, and natural broadening based on plasma parameters (pressure of the discharge, etc.), with T_{rot} and T_{vib} as inputs. Additionally, SPECAIR accounts for instrumental broadening by convolving the simulated spectrum with a spectrometer "slit function". In the present work, the "slit function" (and so instrumental broadening specific to our setup) was measured using the HeNe laser line at 632.8 nm with the same spectrometer configuration as used for OES measurements (1,200 groove/mm grating, 100 μm slit width). SPECAIR was then used to simulate the first positive N_2 spectrum under various conditions and temperatures (T_{vib}, T_{rot}, and T_{trans}), with iterative fits to experimental data to determine T_{rot} and thus T_{gas}, as well as to approximate T_{vib}. SPECAIR results were also benchmarked against the method of deBendictis [49], which involves taking ratios (known as R21 = I2/I1 and R31 = I3/I1) of three emission peaks (I1, I2, I3) associated with the 3-0 band transitions of N_2 in the 686-688 nm spectral range (see Figure 3.4(a)), and comparing them with empirical fits to rigorous quantum mechanical simulations based on T_{rot}.

3.1.3 Double Langmuir probe

A double Langmuir probe (DLP) was used to measure T_e under different plasma operating conditions. Unlike the more commonly used single Langmuir probe, where the single probe is biased with respect to some reference (usually the anode/ground of the discharge, or a metallic wall, etc.), the wires of a double Langmuir probe are biased with respect to each other. As such, they are otherwise completely isolated from the rest of the plasma system. The DLP approach was required for the microplasma jet

to avoid completing the plasma circuit through the Langmuir probe itself, i.e., a single probe wire would act as the plasma anode and disturb the discharge under certain bias configurations. The floating double probe circuit is shown schematically in Figure 3.2, and uses using a floating Keithley 2400 SourceMeter as the variable voltage source with reversible polarity. The meter also monitored ion current and probe bias. Cylindrical DLPs were constructed out of two 120 μm tungsten wires, each 2 mm long, with 1 mm distance between the two wires (see Figure 2.8 and associated discussion in Chapter 2 for details).

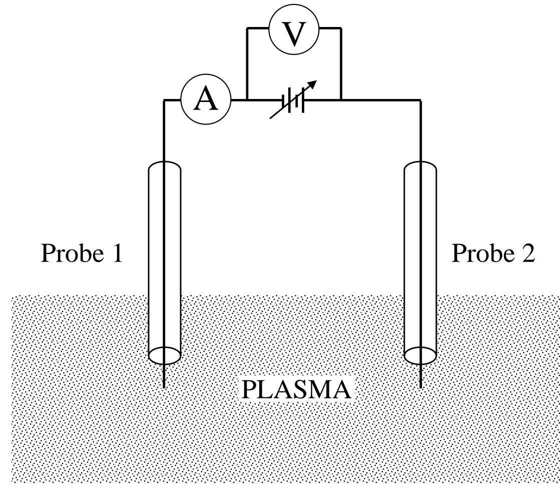

Figure 3.2: Schematic of a floating double Langmuir probe system.

The DLP bias was swept between -20 V and 20 V and the resulting IV characteristics were fit with the following model to extract the electron temperature ξ in eV (see [53,54] for details):

$$I_p = I_{1+} \tanh\left(\frac{V_p}{2\xi}\right) + \frac{I_{1+} - I_{2+}}{\exp\left(\frac{V_p}{\xi}\right) + 1} \tag{3.1}$$

where I_p is the net probe current, I_{1+} and I_{2+} are the ion saturation currents for probes 1 and 2, V_P is the probe bias voltage, and ξ (commonly referred to as T_e) is the elec-

tron temperature. The above model was fit to experimental data using LabVIEW with adjustment of T_e, I_{1+}, and I_{2+} until good overlay was achieved.

3.2 Results and discussion

A representative OES spectrum of an Ar/N_2 microplasma jet at 10 Torr and 8.5 mA is shown in Figure 3.3; strong emission lines from metastable Ar ions and neutrals can be seen in the blue and red regions, along with the characteristic first and second positive systems of N_2 in the red and UV regions, respectively. The bottom panel provides a SPECAIR simulation of an N_2 plasma for comparison, which clearly shows similar features for the first and second positive systems. For the remainder of this section, we focus entirely on the first positive system, with specific analysis of the (3,0) band region in the 680-690 nm range.

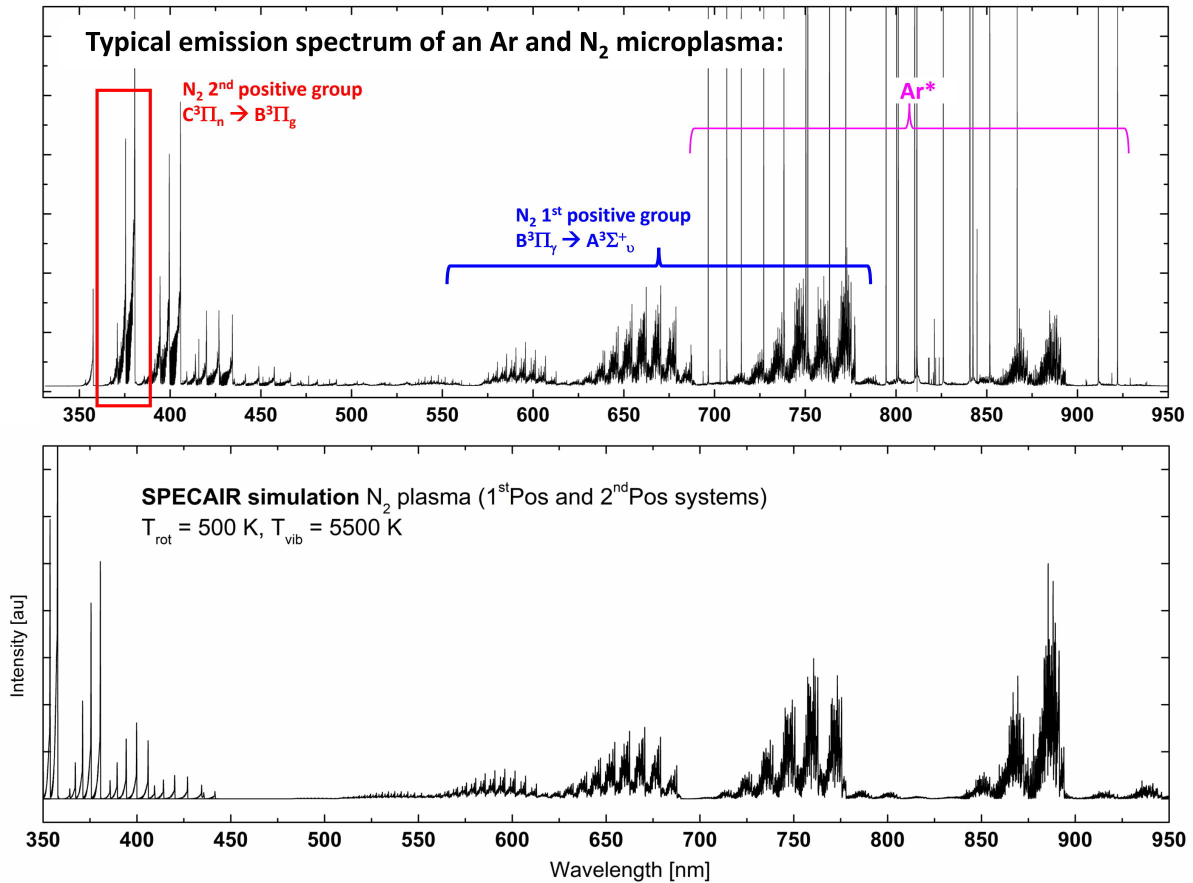

Figure 3.3: OES spectrum of an N_2/Ar microplasma jet at 10 Torr and 8.5 mA (top), along with a SPECAIR simulated spectrum (bottom) of an N_2 plasma with T_{rot} = 500 K and T_{vib} = 5500 K.

3.2.1 Rotational, vibrational, and gas temperatures in an Ar microplasma jet

Figure 3.4(a) shows an experimental OES spectrum and a converged SPECAIR fit for an Ar microplasma with 2.5% N_2 in the jet feed. The simulated spectrum is an excellent fit, and gives T_{rot} = 560K and T_{vib} = 5000K. The three sub-bandhead peaks used in the de Benedictis model are also labeled as I1, I2, and I3. First off, the rotational temperature, and hence overall gas temperature, of the jet is relatively low (550K), on

par with expectations given that microplasmas in general are rather cold discharges. The 550K value for our low pressure suspersonic jet is similar to, but slightly colder (100-200K) than temperatures measured near (< 1mm) the cathode in a static Ar slit microdischarge at 100 Torr and similar currents [50]. We hypothesize that the supersonic expansion in our case plays an additional role in cooling of the gas, resulting lower downstream temperatures. When the plasma current was incrementally increased (panel (b)), a steady increase in the relative intensity of the I3 and I2 peaks (all spectra were normalized to the I1 peak) was observed, indicating that more plasma current results in higher effective gas temperatures, as might be expected. The resulting T_{rot} values from SPECAIR and the de Benedicis model are in excellent agreement (panel (c)), and appear to linearly increase with plasma current up to 20 mA, followed by a gentle leveling off of the temperature at 700-800K for 30 mA. At these high currents, the end of the capillary tube was seen to glow red slightly, and support the idea that the gas in the plasma volume within the capillary tube may be in thermal equilibrium with the capillary cathode wall, as has been observed for hollow cathode arc discharges [55]. The low effective gas temperatures measured in the microplasma jet are also reasonable, given that it is possible to deposit nanostructured materials on polymers and photoresist features without damage (see Chapter 6 for details.)

Given the agreement in T_{rot} between the two OES models, T_{vib} at different plasma currents was determined with SPECAIR using the T_{rot} values determined from the deBenedictis fits. These T_{vib} values are seen to range from 4,000 to 6,000 K, which is typical for low pressure discharges, as N_2 exchanges vibrational energy with electrons faster than with heavy particles, and exchanges rotational and translational energy faster with heavy species [56].

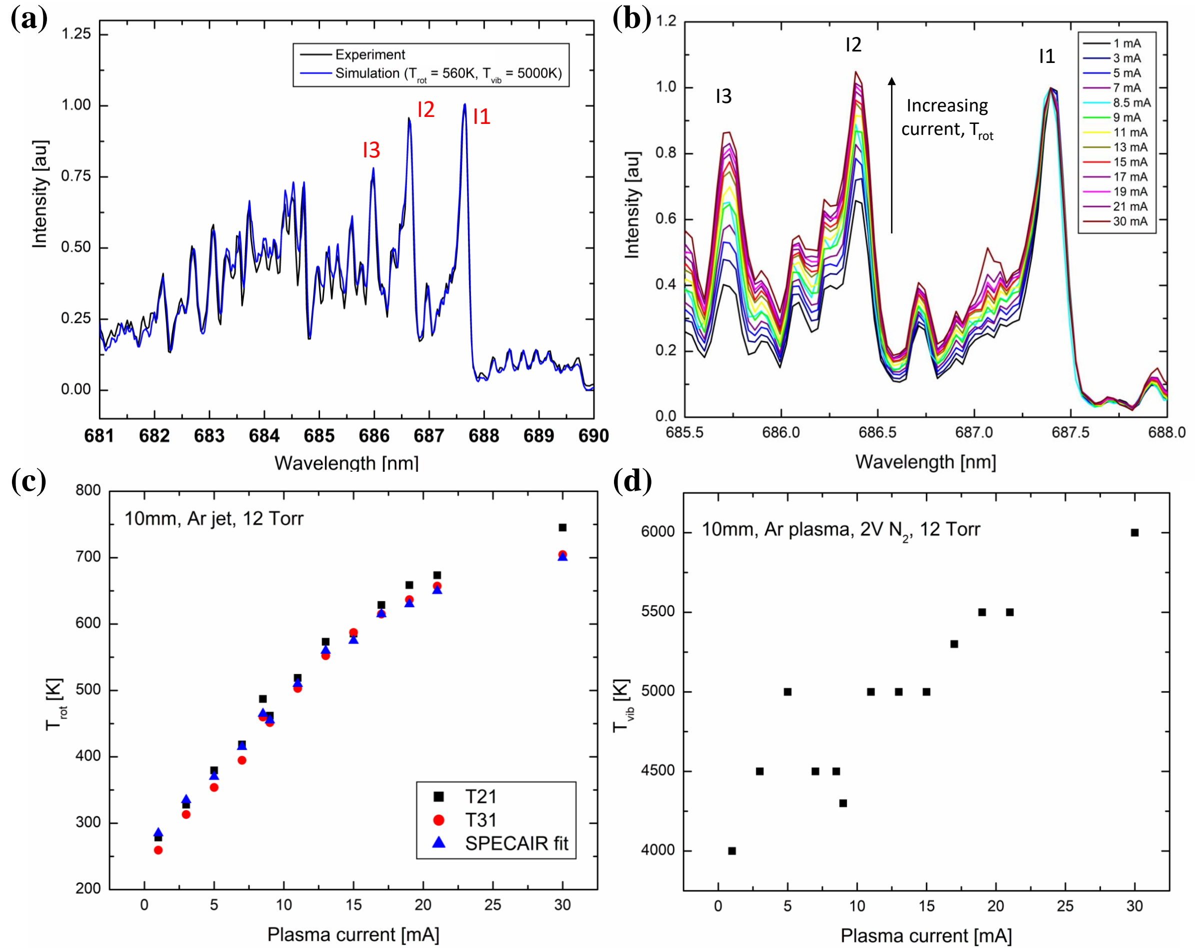

Figure 3.4: (a) Quantum mechanical fit of the first positive OES region of N_2 ($B^3\Pi_g \longrightarrow A^3\Sigma_u^+$) with SPECAIR simulation using an input of T_{rot} = 560 K and T_{vib} = 5,000 K, for an Ar microplasma jet with 2.5% added N_2 operating at 10 Torr and 8.5 mA. (b) Evolution of OES data as the microplasma current is increased. (c) T_{rot} values calculated via fits to OES spectra using the deBenedictis model (R21 and R31 line ratio method, equivalent measures) and SPECAIR. (d) SPECAIR-derived vibrational temperatures from simulations using the rotational temperatures given in (c).

3.2.2 Electron temperature and ion saturation current

Measurements of the local electron temperature in the expanding microplasma jet was carried out by placing a movable double Langmuir probe at different positions in

the jet plume downstream of the capillary exit. Figure 3.5 (a) shows three typical IV characteristics for an Ar jet at 10 Torr and 3 mA, measured at d = 3, 5, and 10 mm downstream of the capillary exit. In general, the IV characteristics are symmetric, which they should be given the floating probe configuration, and they approach a saturation current at large differential bias when the plasma sheath around the probe wires is space charge limited. Saturation currents do slightly increase with bias, instead of plateauing, due to slow expansion of the sheath at high bias providing a larger lateral surface area around the probe before for the onset of the space charge limit. The trend with distance, i.e., larger saturation currents closer to the capillary exit, makes sense because charged plasma species collide with background gas and are neutralized as the jet plume expands. This phenomenon, namely quenching of plasma charge carriers with distance from the source, is highlighted in Chapter 5, where it is observed that substrate charging, and the resulting film morphology, depends critically on the electrostatic configuration at the film deposition front.

Figure 3.5(b) shows a model fit of equation 3.1 to the DLP data, and gives an electron temperature of T_e = 2.4 eV. Similar fits were conducted for DLP measurements at different locations in the jet plume and plasma currents; these T_e data are summarized in Table 3.1. In general, T_e's are in the 1-2.5 eV range, and higher plasma currents and larger downstream distances result in lower T_e. These trends can likely be explained by (i) lower plasma currents resulting in lower plasma density, and hence more opportunity for electrons to experience the Pendel effect and gain energy in the hollow cathode, and (ii) plasma electrons suffer more energy-robbing (inelastic) collisions with background gas as the plasma jet expands.

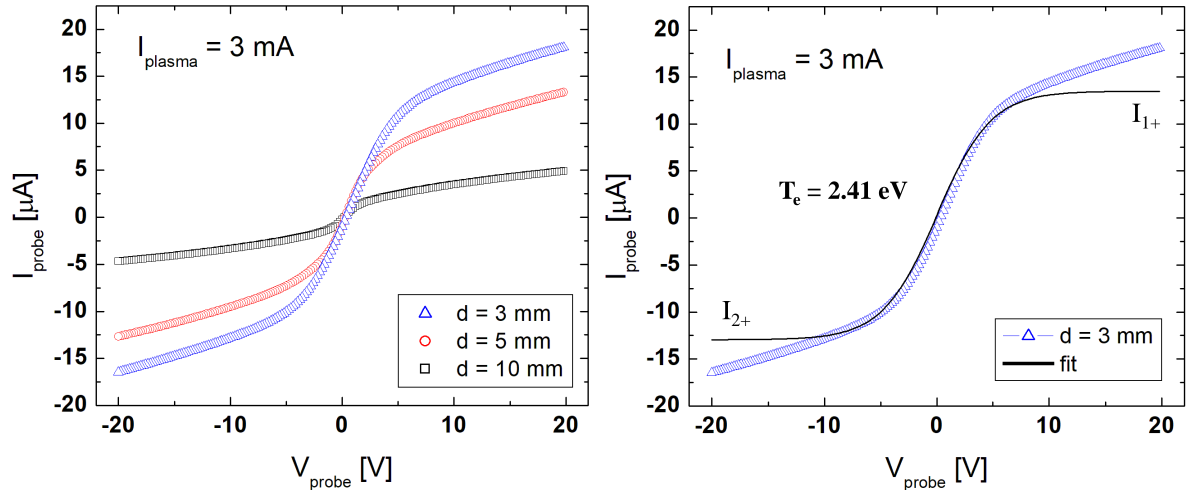

Figure 3.5: (a) Double Langmuir probe (DLP) IV characteristics measured at different points in the plume of an expanding Ar microplasma jet at 10 Torr and 3 mA. Distances correspond to the location of the DLP wires from the capillary tube cathode exit. (b) Model fit (equation 3.1) of DLP data, showing how the electron temperature (T_e) can be extracted from the IV characteristic.

Plasma current	3 mm	5 mm	10 mm
3 mA	2.41 eV	1.17 eV	0.87 eV
8.5 mA	1.44 eV	2.05 eV	1.07 eV
20 mA	1.39 eV	1.07 eV	0.99 eV

Table 3.1: Summary of T_e measurements of an Ar microplasma jet operating at 10 Torr at different currents and distances downstream of the capillary tube cathode exit.

3.2.3 Effect of plasma circuit configuration and O_2 addition on double Langmuir probe measurements

As will be discussed more deeply in Chapter 5, the electrostatic configuration of the sample, as it relates to how the microplasma jet bias circuit is completed, namely through the sample vs. to a remote ring anode, plays a large role in the morphology, crystallinity, and fluorine content of the deposited film. Here, we explore how the bias configuration, plasma current, and O_2 addition affect (nor not) the electron temperature and saturation

currents measured in the jet. These measurements were conducted with an Ar jet at 12 Torr with a grounded graphite chuck (functioning as the plasma anode) or a floating teflon chuck with a grounded ring anode, with the DLP and chuck placed at 5 mm and 15 mm downstream of the capillary exit, respectively.

Figure 3.6 (a-c) shows a summary of these DLP measurements for different plasma conditions, where T_e and saturation currents can be seen to change significantly with plasma current. Overall, the general behavior for both bias configurations can be grouped into two regimes, namely below and above 8-9 mA drive current, where the behavior is markedly different. For the low current regime, large variations or spikes in T_e, ranging from 0.5 to 4 eV in some cases can be seen, with similar trends in the saturation current. In this regime, the plasma jet was observed to progress through different phases of emission intensity and shock structures that were extremely sensitive to the current, reminiscent of pre-discharge-like phenomena and instabilities that can occur under higher *pd* situations. Support for this explanation can be found in the actual plasma drive circuit IV characteristic shown in Figure 3.8, where the voltage drop across the plasma is not constant, and hence not a hollow cathode, below 8-9 mA. However, above ∼8-9 mA, the microplasma jet was seen to quiet down and stabilize with T_e's in the 1 eV range, and saturation currents that scaled linearly with plasma drive current. This current regime is true micro-hollow cathode operation, where the voltage drop across the plasma is indeed approximately constant as current is increased. Additionally, how the plasma circuit is completed does affect details of the DLP characteristic, but similar spikes in T_e and saturation current were obtained in both cases below the 8-9 mA threshold.

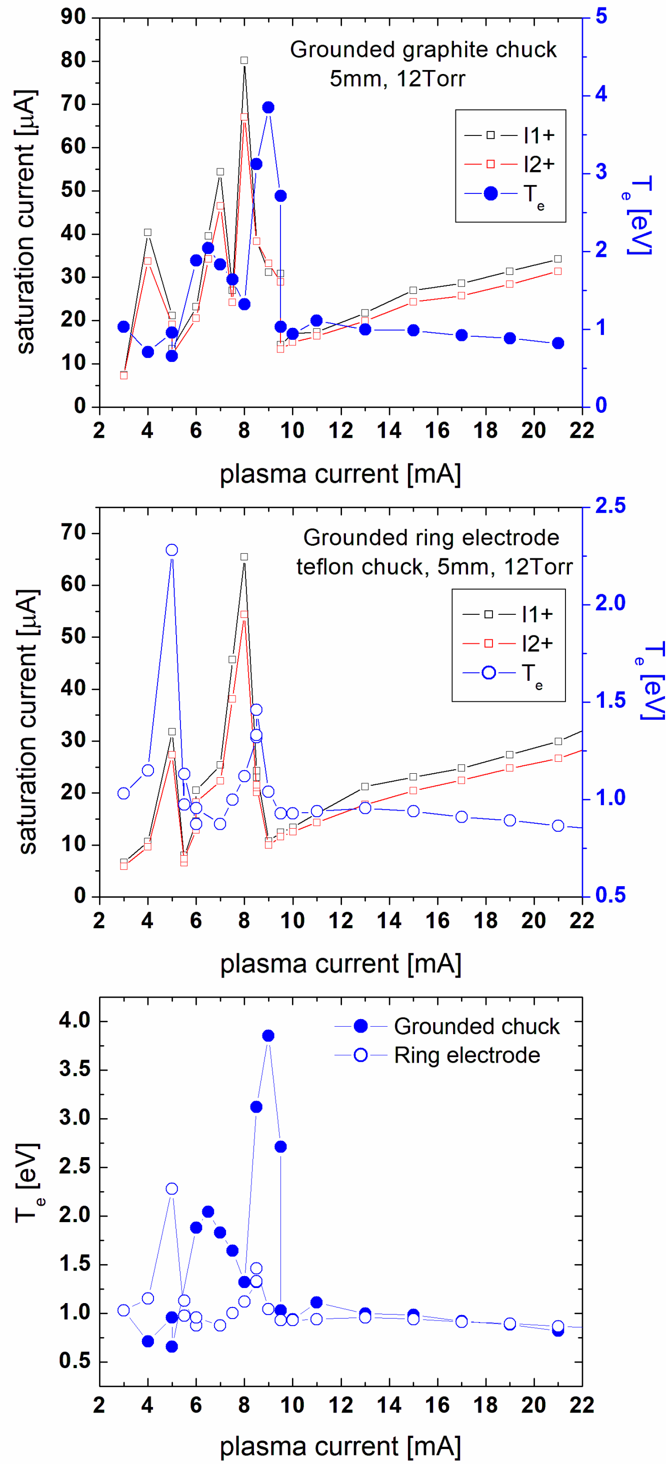

Figure 3.6: DLP data for saturation currents and electron temperatures for an Ar microplasma jet at 12 Torr, with grounded graphite chuck anode vs. remote ring anode with a teflon chuck.

Although the spikes in the electrical characteristics at low currents would imply unstable plasma jet operation, the observed trends were qualitatively reproducible over the 1-8 mA range as plasma current was raised and lowered. This observation suggests that multiple, reasonably stable operating regimes occur, the physics of which need to be explored further. We also hypothesize that the current regulated mode of biasing the plasma discharge was quite important in squelching oscillations and instabilities, if they indeed occurred. It should be noted that many of the nanostructured films in this work were deposited at 8.5 mA, within or near the low current regime; however, all of the deposited films, in general, had well defined morphologies, which is interesting given the complexity and stability of this low current, likely pre-discharge, operating regime. Additional DLP measurements with O_2 in the jet feed vs. the chamber background only, at different capillary exit-probe distances, and for different bias configuration were also carried out, as summarized in Figure 3.7. Similar behavior was observed in all cases, namely large spikes in T_e and saturation currents in the low current regime and quiet, stable operation above $\sim$10 mA. Details of these various operational configurations need further investigation.

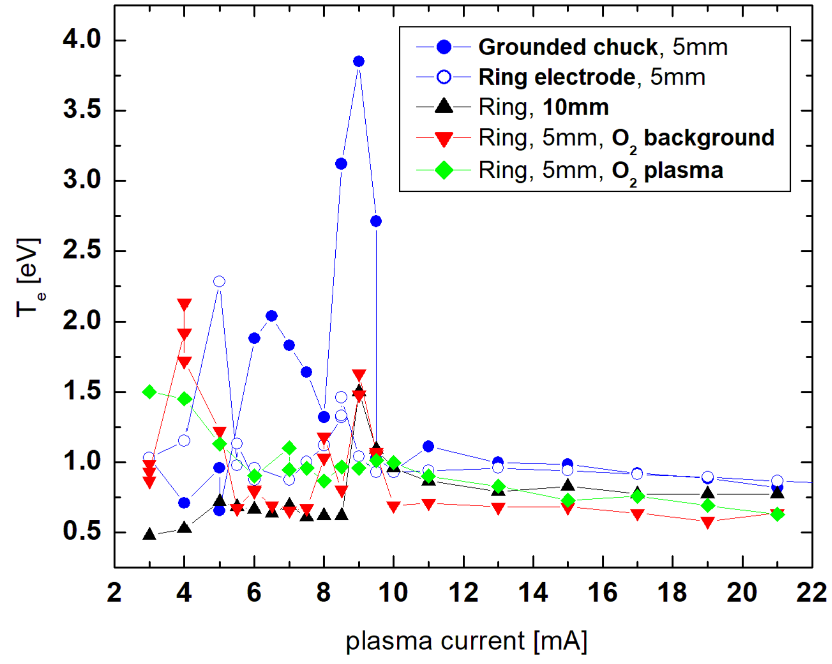

Figure 3.7: Comparison of electron temperature (T_e) for various plasma operating conditions.

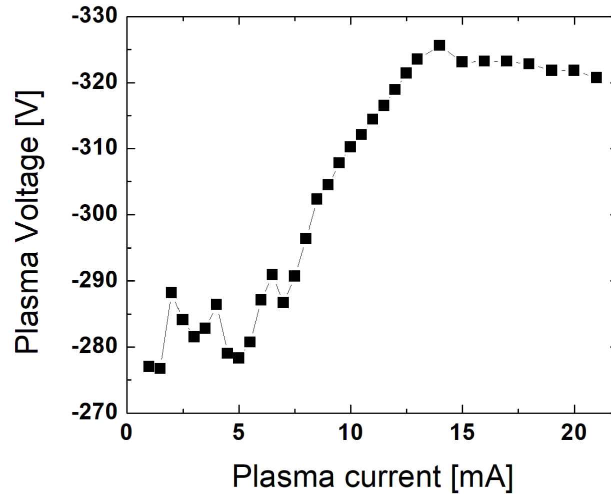

Figure 3.8: Microplasma jet drive circuit IV characteristic. At currents below 8-9 mA, the bias voltage across the plasma was seen to increase with current, indicative of a pre-discharge operational mode. Above 10 mA, the voltage bias is constant as current is raised, indicative of true hollow cathode operation. Operating conditions were 160 sccm Ar and 12 Torr using a grounded ring anode.

3.3 Summary and conclusions

This chapter explored the use of optical emission spectroscopy (OES) and double Langmuir probe (DLP) methods to characterize the operation of the microplasma jet source. OES with trace N_2 in an Ar jet yielded estimates of $T_{rot} = T_{gas}$ and T_{vib} of 500-700 K and 5000-6000 K, respectively, using two independent methods, demonstrating that the microplasma jet source is indeed a cold plasma. DLP data also provided estimates of T_e in the range of 1-2.5 eV, which depend on the exact location in the expanding jet plume. In general, lower plasma currents and smaller downstream distances resulted in higher T_e, which could be rationalized based on the increased likelihood of electrons gaining energy via the Pendel effect and quenching by collisions with the background gas during the jet expansion. The transition between a pre-discharge-like operating regime at low plasma currents ($<$ 8-9 mA) and true hollow cathode operation ($>$ 10 mA) was

observed in the plasma circuit IV characteristic. Future studies are underway to connect the electrical operating characteristics of the microplasma jet source with the morphology, crystallinity, and stoichiometry of the deposited nanostructured thin films.

Chapter 4

Microplasmas for direct, substrate-independent deposition

This chapter has been adapted from: K. E. Mackie, A. C. Pebley, M. M. Butala, J. Zhang, G. D. Stucky, and M. J. Gordon, "Microplasmas for direct, substrate-independent deposition of nanostructured metal oxides", Applied Physics Letters, 109(3), p.033110, 2016.

A general, substrate-independent method for plasma deposition of nanostructured, crystalline metal oxides is presented. The technique uses a flow-through, micro-hollow cathode plasma discharge (supersonic microplasma jet) with a 'remote' ring anode to deliver a highly-directed flux of growth species to the substrate. A diverse range of nanostructured materials (e.g., CuO, γ-Fe_2O_3O, and NiO) can be deposited on any room temperature surface, e.g., conductors, insulators, plastics, fibers, and patterned surfaces, in a conformal fashion. The effects of deposition conditions, substrate type, and patterning on film morphology, nanostructure and surface coverage are highlighted. The synthesis approach presented herein provides a general and tunable method to deposit a variety of functional and hierarchical metal oxide materials on many different surfaces.

High surface area, conversion-type CuO electrodes for Li-ion batteries are demonstrated as a proof-of-concept example.

4.1 Introduction

The ability to synthesize functional nanoscale materials, as well as to integrate these structures into devices, is fundamental for the development of next-generation micro- and optoelectronic devices, sensors, and energy harvesting and storage technologies [57–60]. Realization of nanomaterials and multi-scale systems often requires complicated processing steps that may involve a combination of wet chemistry, physical/chemical vapor deposition, vapor-liquid-solid or molecular beam epitaxy, self- and/or directed assembly, lithography, and etching. In addition, both wet and dry conditions, long processing times, high temperatures, vacuum processing, and templates or catalysts can be required. As such, we continually seek to develop general and tunable methods that can easily and rapidly create nanostructured functional materials. For example, atmospheric pressure plasmas [61, 62], plasma sprays [63–65], and microplasmas [12, 13, 24, 25, 27, 28, 66–70] have shown much promise toward this goal. Extending and adapting such methods in a generic way to different material systems and deposition situations, as well as understanding how plasma operating conditions affect growth processes, is critical for their implementation.

In this work, we present a general, microplasma-based approach for direct deposition of nanostructured and conformal, crystalline metal oxides (CuO, NiO, γ-Fe2O3) on virtually any substrate (e.g., conductors, insulators, polymers, fibers, patterns) at room temperature. A supersonic DC microplasma jet is seeded with organometallic precursors under oxidizing conditions to create a directed flux of growth species (e.g., atoms, ions, clusters, and/or nanoparticles) that are subsequently "spray-deposited" onto the surface

of interest. A remote, concentric ring anode, instead of the substrate, is used to complete the plasma circuit, allowing deposition on both conducting and insulting surfaces. Herein, we highlight the diverse range of materials that can be realized using microplasma growth and discuss how plasma operation and deposition conditions affect film morphology. High surface area CuO films were tested as conversion reaction anodes for Li-ion battery applications to demonstrate incorporation of microplasma-deposited films into devices, and the potential of microplasmas to synthesize nanostructured materials for energy applications.

4.2 Experimental details

Metal oxide nanostructures were deposited on a variety of different substrates using the microplasma deposition system depicted in Fig 4.1 A flow-stabilized, direct-current hollow cathode discharge was used to crack sublimed organometallic precursors into active growth species (e.g., atoms, ions, and clusters), which were directed towards the substrate under supersonic flow conditions. Nickelocene, ferrocene, copper(II) acetylacetonate (Cu(acac)2), and copper(II) hexafluoro-acetylacetonate hydrate ($Cu(hfac)_2$ xH_2O) (STREM) were sublimed and fed with 100-300 sccm Ar to the plasma jet cathode (stainless steel capillary, ID=500 μm) that was biased with current-regulated, DC high voltage (10 mA, 300-800 V). A macor-insulated stainless steel ring near the capillary exit served as the anode to complete the plasma circuit. Oxygen (50-100 sccm) was introduced into the cathode gas feed or chamber background, the latter being maintained at 10-50 Torr. The substrate stage, 8-12 mm downstream from the capillary exit, was static or raster-scanned in a serpentine pattern at a rate of 2-10 μm/s during growth. Deposition rates varied for different materials, but generally fell in the 50-100 nm/minute range, measured directly beneath the jet centerline. Substrates were conducting (<0.001 Ω-cm) and insu-

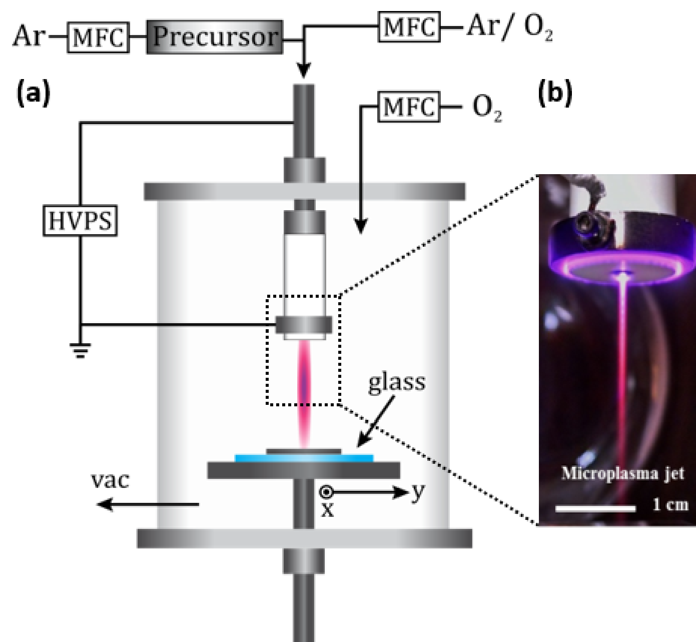

Figure 4.1: (a) Schematic of the microplasma deposition system. Ar carrier gas and sublimed organometallic precursor(s) are introduced into a stainless steel capillary (ID = 500 μm) inside a macor insulator with ring anode. A hollow cathode DC plasma is struck between the capillary and ring anode using a current-regulated, high voltage power supply (HVPS). O_2 is introduced into the chamber background at a rate of 50-100 sccm. (b) Photo of microplasma jet operating with 200 sccm Ar at 15 Torr and 8.5 mA. MFC = mass flow controller.

lating (>2000 Ω-cm) Si, glass coverslips, 300 nm ITO on glass, 50 μm Kapton polyimide film, 125 μm polished stainless steel, carbon paper, and fiberglass cloth. Deposition on patterned Si, i.e., micropillars created using colloidal lithography and reactive ion etching (see [71] for details), was also considered in order to evaluate if the deposited oxide films were conformal.

Crystallinity and phase of the deposited oxide coatings were analyzed via θ-2θ XRD (with -4 degree offset to suppress Si substrate peaks) using Cu Kα radiation on a PANalytical Empyrean diffractometer; high resolution micrographs and energy dispersive x-ray (EDX) spectra were taken on an FEI XL40 SEM and an FEI Tecnai G2 F20 S-Twin TEM using lacey carbon grids. X-ray photoelectron spectroscopy (XPS) analysis (Supplementary Information) of the films was carried out on a Kratos Ultra system with

monochromatic Al-Kα radiation. CuO films on Cu foil substrates were also tested as Li-ion battery electrodes that store charge by the conversion mechanism. Films were tested in Swagelok cells against a Li metal electrode in an electrolyte solution of 1 M $LiPF_6$ in 1:1 v/v ethylene carbonate:dimethyl carbonate with a glass filter paper separator. Cells were cycled at a rate of C/20, such that the theoretical 2e reaction of CuO to Cu and Li_2O upon reaction with Li takes place in 20 hours.

4.3 Results and discussion

4.3.1 Substrate-agnostic deposition

Nanostructured CuO was grown at room temperature on conducting, insulating, flexible, patterned, and fiber-based substrates to demonstrate the versatility of microplasma spray deposition (Fig. 2). Completing the plasma circuit through the remote anode ring, rather than the substrate, allowed deposition on insulating and floating substrates. All CuO deposits appeared to have similar “agave-like” nanowire morphologies, and coatings were reasonably conformal on both fibers and Si micropillars. For the fiber-based substrates, complete conformal coverage of the oxide was observed on the first few layers of the material, with coverage becoming more sparse on the inner layers due to shadowing. XRD also showed that all of the coatings were the monoclinic (tenorite) phase of CuO. Several points about the CuO deposition are noteworthy, as discussed in detail below: (1) films were nanocrystalline, monoclinic CuO with high surface area, even in the early stages of growth; (2) the identity and crystallinity of substrate do not appear to affect the film morphology; and (3) the deposited films were reasonably conformal.

XRD of microplasma-grown CuO nanowires on various substrates revealed that the structures are crystalline (Fig 4.4(a)), with no observable Cu_2O phase, and TEM further

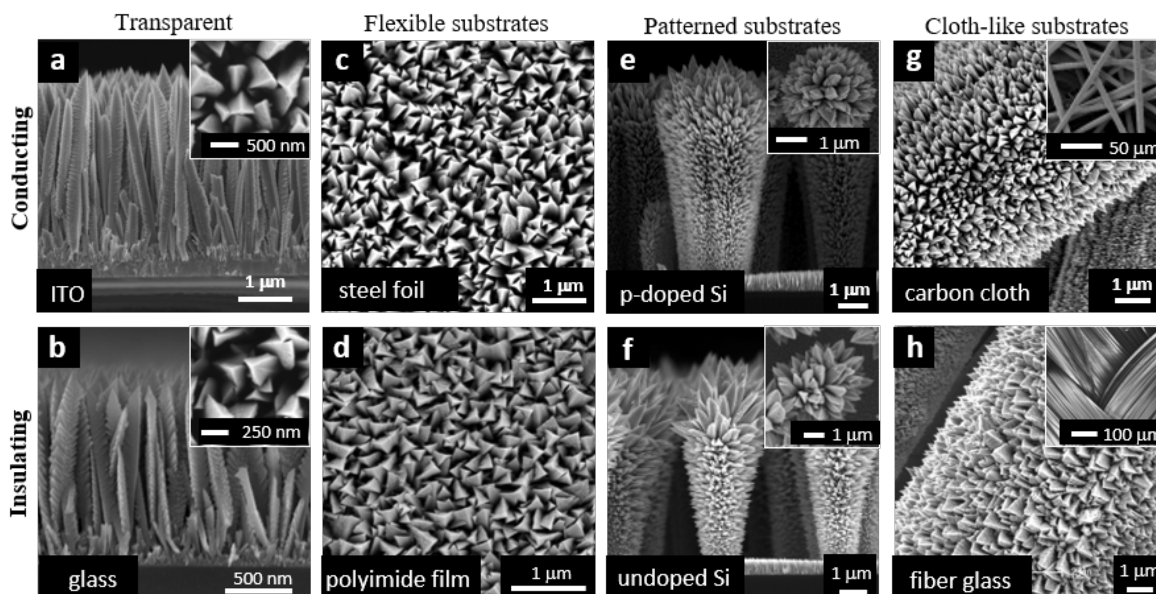

Figure 4.2: Microplasma spray deposition of CuO at 20 Torr, 8.5 mA with Ar:O_2 = 3:1 (O_2 in the background gas) on various, unheated substrates: (a) ITO, (b) glass, (c) stainless steel foil, (d) Kapton polyimide film, (e) conducting Si micropillars, (f) undoped (insulating) Si micropillars, (g) carbon paper, and (h) fiberglass cloth. Insets show top-down images of the oxide films at various length scales.

shows single-crystalline regions in the nanowires (Fig 4.4(b)-(d)). Nanowires were seen to principally grow along the direction. XPS analysis (see Supplementary Information) also showed Cu^{2+} with characteristic CuO shakeup satellites, and no indication of Cu^0. Scherrer analysis of the (-111) and (111) reflections from the CuO nanowire sample estimates crystallite size at 11 nm. The early stages of CuO growth were investigated by directing an Ar/Cu(hfac)$_2$ jet onto a lacey carbon TEM grid for one minute [Fig 4.4(e)]. Although the plasma jet flow distorted the fragile lacey carbon grid, a conformal coating of small (¡ 5 nm), seed-like CuO crystal growths with facets can be seen. The corresponding SAED pattern [panel (f), inset] for this sample indicates that the seeds are indeed crystalline CuO, with reflections corresponding to the monoclinic tenorite phase. Contamination from the capillary tube cathode, ring anode, or C from the precursor, was not seen in the CuO films, as evidenced by the lack of EDX signals from stainless

steel (Fe, Cr, Ni, etc.) and C. It is believed that active oxygen species are responsible for C removal from the growing film.

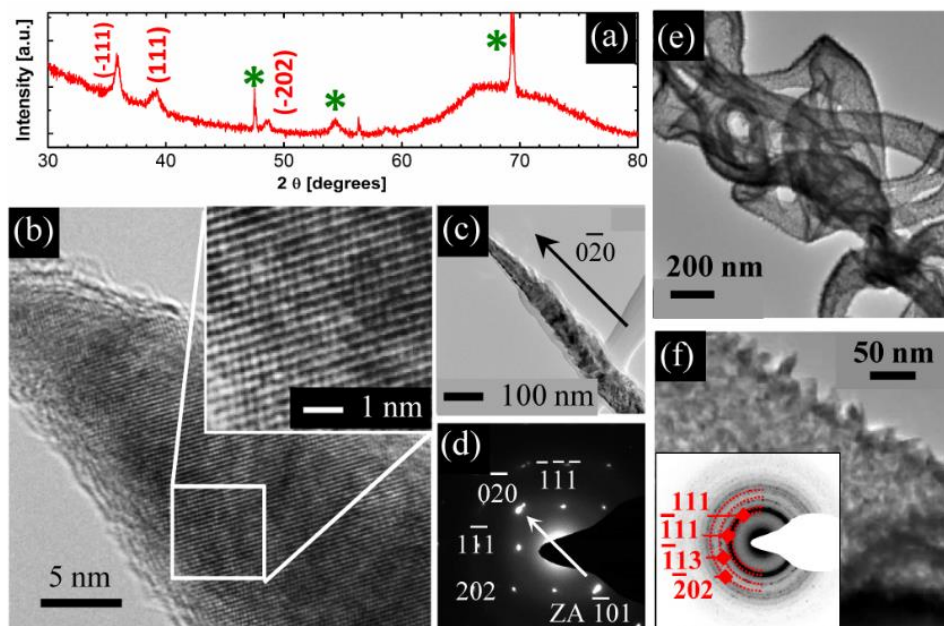

Figure 4.3: Characterization of microplasma-deposited CuO. (a) XRD scan of CuO deposit shown in Fig. 2(e), with reflections for monoclinic CuO (tenorite) shown. Green * are peaks from the Si substrate. (b) HRTEM image of a single-crystalline region of a CuO nanowire grown on Si with zoom of lattice planes. (c) Corresponding Low resolution image and (d) SAED pattern for the nanowire shown in (c). Growth of the wire was along the direction. (e) CuO nanocrystallites collected on a lacey carbon TEM grid exposed to an Ar/Cu(hfac)2 jet for one minute. Panel (f) inset shows the SAED ring pattern with reflections for tenorite CuO noted.

It is initially surprising that crystalline CuO can be deposited on a substrate that is 'nominally' at room temperature (i.e., a thermocouple beneath the sample read <70 degrees C throughout deposition). However, particle nucleation and crystallization in nonthermal plasmas, with gas temperatures well below the crystallization threshold, have been reported and studied for several years [21,23,72,73]. These works suggest that, due to energetic surface processes (e.g., ion/electron collisions, ion-electron recombination,

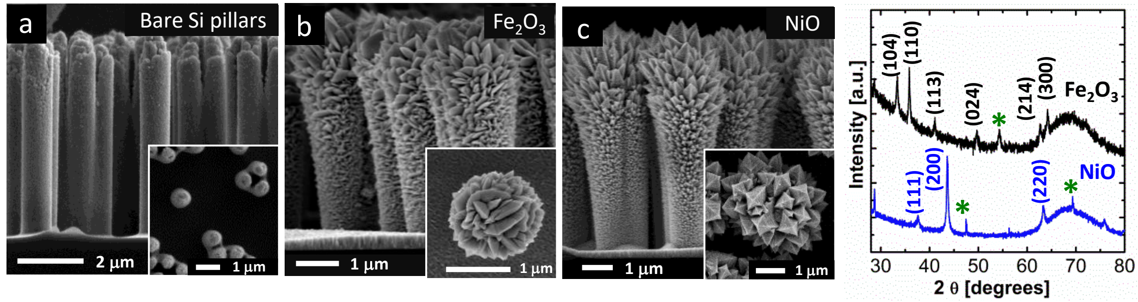

Figure 4.4: Microplasma deposition of (b) α-Fe_2O_3 and (c) NiO on 2.5 μm high Si micropillars (a). Insets show top-down zoom images of the oxide morphology. (d) XRD spectra of the films in (b) and (c). Reference reflections for NiO (bunsenite, rock-salt) and α-Fe_2O_3 (hematite, rhombohedral) are noted. Si substrate peaks are denoted with green *. All materials were deposited at 20 Torr, 8.5 mA with Ar:O_2 = 8:1 (O_2 in the jet) on unheated Si micropillar substrates; deposition time was 15 min with no substrate rastering.

and chemical reactions), clusters (nanoparticles) in the plasma can be selectively heated above the overall gas temperature. For example, it has recently been estimated that Si nanoparticles $<$10 nm formed in a non-thermal atmospheric pressure microplasma can reach temperatures of 750K due to collisional heating [22]. A similar mechanism may be at play here, forming crystalline CuO seeds in the plasma; in addition, bombardment of the substrate by the plasma jet afterglow could enhance surface diffusion by locally increasing the surface temperature.

The microplasma deposition technique can also be easily extended to other oxide systems, such as NiO and α-Fe_2O_3, and for conformal deposition, as shown in Fig. 4. Similar plasma operating parameters (20 Torr, 8.5 mA, Ar:O_2=8:1 with O_2 in the jet) and static substrate were used to deposit both oxides on silicon micropillars at room temperature. Oxide coverage was reasonably conformal, with growth at the tops of pillars being favored due to shadowing effects. The observed crystal habits for each oxide were consistent with the bunsenite (rock-salt) phase of NiO and the hematite (rhombohedral) phase of α-Fe_2O_3. Scherrer analysis of the NiO (200) and Fe_2O_3 (104)/(110) reflections

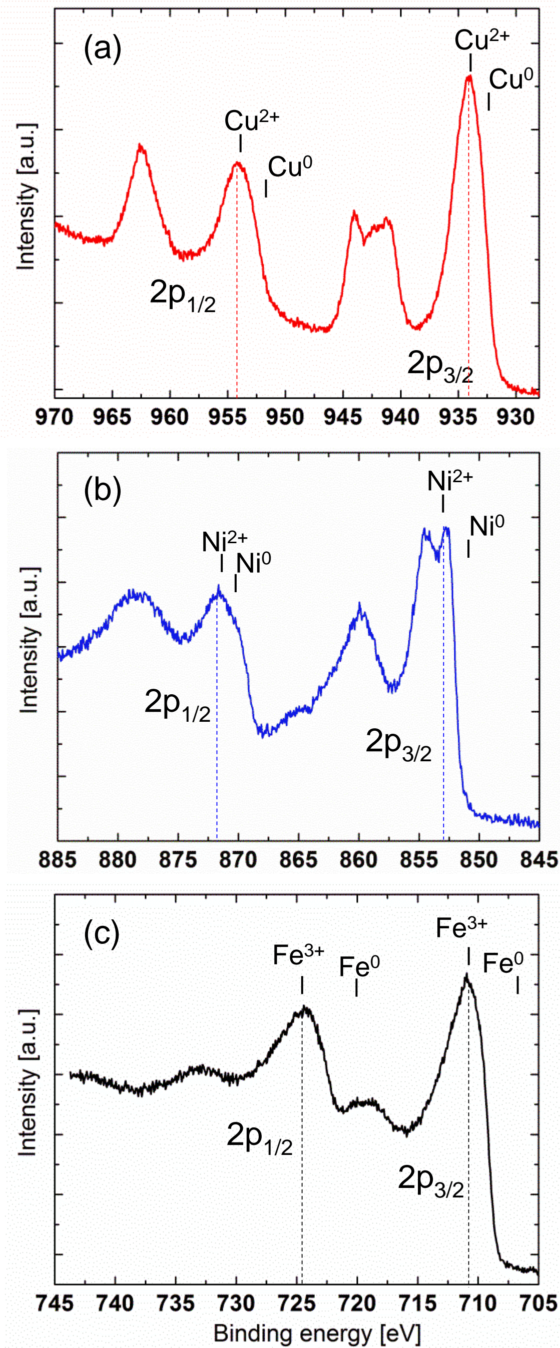

Figure 4.5: High resolution Cu, Ni, and Fe 2p spectra of microplasma-deposited CuO (a), NiO (b), and Fe_2O_3 (c) nanostructures on Si micropillar substrates (Figs. 2(e), 4(b), and 4(c)).

gave crystallite sizes of 20 and 23 nm, respectively. XPS of the films additionally showed Fe^{3+} and Ni^{2+} chemical environments, in agreement with the Fe_2O_3 and NiO phases seen by XRD. A Kratos Ultra x-ray photoelectron spectroscopy (XPS) system was used to measure the surface compositions of as-deposited nanostructures [see Fig. S1]. High resolution Cu, Ni, and Fe 2p spectra corroborate the XRD-determined compositions and oxidation states of the deposited materials. Cu2+ is the dominate species at the surface of the copper oxide nanowires, as evidenced by shakeup satellite peaks only observed for paramagnetic Cu(II) (Fig. SI (a)). Additionally, the lack of shoulders in the 2p3/2 and 2p1/2 peaks and the large size of the satellite peaks relative to the 2p further suggest pure CuO [1,2]. Likewise, the Ni and Fe 2p peaks correspond to Ni^{2+} and Fe^{3+} species, respectively [3,4], and are in agreement with the XRD-determined phases of NiO and Fe_2O_3.

4.3.2 CuO Conversion-type Li-ion battery

Finally, nanostructured CuO films were evaluated as conversion electrodes for Li-ion batteries. CuO directly spray-deposited onto a copper foil current collector was assembled in a Swagelok cell against a Li metal anode at a rate of C/20. As can be seen in Fig 4.6, the microplasma-deposited electrode exhibited high specific capacity and good cyclability (650 mA h/g over several charge-discharge cycles). The large and irreversible capacity loss after the first discharge-charge cycle is characteristic of CuO and other transition metal oxide conversion materials [74]. This loss is attributed to several factors including the incomplete conversion of Cu into Cu_2O instead of CuO during charge, cracking due to large volume expansion that could compromise electrical contact, and the formation of a solid electrolyte interphase (SEI) [74]. Despite the irreversible capacity loss in the first cycle, a capacity of about 650 mA h/g was retained over several cycles

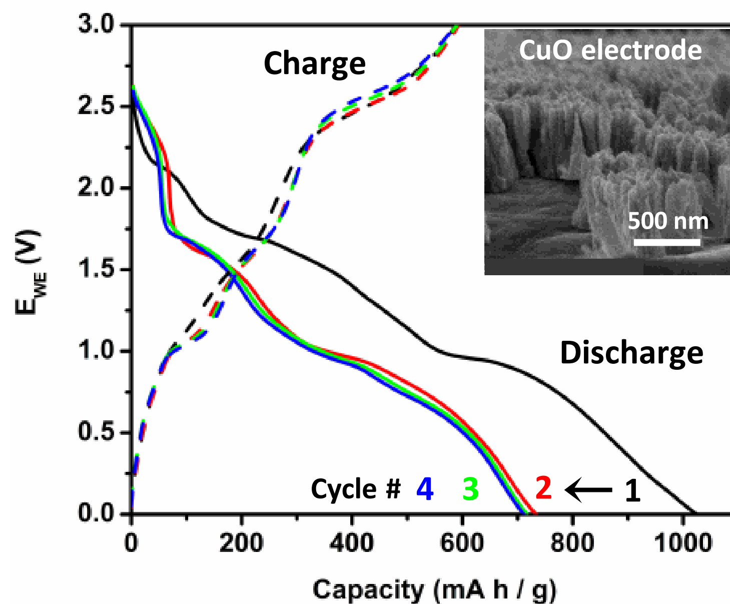

Figure 4.6: Discharge-charge profiles for microplasma-deposited CuO on Cu foil, used as a Li-ion battery anode. Testing configuration was a Swagelok cell operating at C/20 with 1M $LiPF_6$ in 1:1 v/v ethylene carbonate:dimethyl carbonate electrolyte and Li-metal cathode. (inset) SEM image of the CuO film

and is similar to capacities reported for CuO-based electrodes synthesized by traditional chemical methods [75–77]. The microplasma-deposited films have the added benefit in this application of not requiring the conductive carbon additives or polymer binders for electrode preparation, which can constitute 15 percent of the electrode films mass. This preliminary result demonstrates both the ease of integrating microplasma-grown materials into devices with minimal processing, as well as the viability of microplasma deposition to synthesize materials for energy applications.

4.4 Conclusions

In this work, we demonstrated a simple, microplasma-based approach for direct, low temperature deposition of nanostructured metal oxides on a variety of substrates ranging from conductors to insulators, and polymer films to fibers. The films were highly crystalline and conformal, and raster scanning the substrate allowed deposition over larger areas with a single microplasma jet. Overall, we believe that microplasmas have great potential in materials processing, and deposition methods can be extended to a wide range of functional materials and hybrid structures for use in micro- and optoelectronics, sensing, and energy applications.

Chapter 5

Importance of substrate charging during microplasma jet deposition

The influence of charging of the substrate during microplasma jet deposition is discussed in the context of different plasma anode electrical configurations (remote ring anode vs. sample as anode), substrate bias configuration (floating vs. grounded), and for several fluorintated organnometallic precursors, namely $Cu(hfac)_2$ and $Y(hfac)_3$. The electrostatic environment at the deposition front, as well as the ability of the sample to conduct and/or sink plasma current to ground, was seen to have significant impact on the morphology and fluorine contamination of the resulting film deposits. For example, the fluorine content of films was typically 5x larger with the sample as the plasma circuit anode, i.e., the plasma current was sunk through the sample to ground, as compared to using the remote ring anode and electrically floating sample. A case study of these effects is presented for CuO deposition from an Ar/O_2 plasma with $Cu(hfac)_2 \cdot H_2O$, where the F contamination in the film could be tuned using the aforementioned electrostatic effects. Application of the latter is demonstrated as a means to deposit phase pure YF_3 coatings from sublimed $Y(hfac)_3 \cdot H_2O$.

5.1 Introduction

Manipulating the electrostatic environment of the substrate during plasma processing is common practice to optimize etch rates and selectivity, as well as improve deposition rates and film quality. During deposition, tuning the electrostatic potential at the growth front is usually accomplished by biasing the deposition surface. Ostrikov [78] reported that during plasma-assisted quantum dot deposition, surface diffusion in the presence of an electric field (i.e., a biased surface) can result in significantly higher surface diffusion rates, and thus higher crystallinity of the deposited material. Similarly, during plasma-assisted atomic layer deposition (ALD), plasma (ion and electron) bombardment of the surface often allows deposition at lower temperatures, higher film crystallinity, and better control over composition - all due in part to an increase in adatom migration (enhanced surface diffusion) [79, 80]. Additionally, substrate biasing during plasma-assisted ALD can be used to tune growth per cycle, mass density, and crystallinity [80, 81]. Ito *et al.* also showed that accumulated charge on the substrate (10's nC) during SiO_2 deposition with an atmospheric plasma jet had a significant effect on deposition rate [82], i.e., the deposition rate varied from 40-80 nm/s as the effective capacitance of the substrate to ground was changed from 10 to 100 pF; ergo, local charging was quite important.

Microplasmas, at both atmospheric and lower pressures (10's of Torr), have shown great promise in the direct deposition of nanomaterials and nanostructured thin films [12, 25, 26, 47]. Briefly, these plasma jets are used to crack organometallic precursors that then react with O_2 or H_2, resulting in nucleation and aggregration of small growth sub-units, namely atomic clusters and/or small nanoparticles. At higher pressures, these species continue to coalesce until growth is quenched as particles exit the active plasma volume. However, at lower pressures, these fundamental growth units are small, and when deposited on a substrate, have enough mobility to form crystalline features. In

such systems, charging of both clusters and nanoparticles within the plasma, and the deposition substrate, are important. For example, it is commonly seen that clusters and nanoparticles become negatively charged in a plasma due to the difference in electron and ion fluxes across the plasma sheath [23, 83], resulting in reduced agglomeration [23]. It has also been shown that a dielectric substrate beneath a plasma jet will accumulate charge in the same way. Sobota *et al.* [84] and Wild *et al.* [85] have experimentally measured the electrostatic charge deposited on a dielectric by an atmospheric plasma jet. For example, Sobota showed that average fields up to 100 kV/cm could be obtained during one period of a 30 kHz AC excited He jet, and Wild noted that increasing the jet nozzle - substrate separation resulted in significantly lower or no charging at all, e.g., all surface charge was dissipated within a few mm of the nozzle exit.

In this chapter, we investigate how changing the electrostatic environment of the deposition substrate affects the deposition of materials from two common fluorinated precursors. For example, it is found that when the substrate is the plasma anode and grounded, the amount of fluorine in the deposited film is high (20%), resulting in a loss of crystallinity of CuO. However, deposition on a floating substrate that will charge up under the plasma jet yields lower contamination levels (< 5 %) and highly crystalline films. Additionally, given the aforementioned findings, it is shown that by controlling substrate charging, a dense, phase pure YF_3 film can be deposited from $Y(hfac)_3$ precursor.

5.2 Experimental details

All experiments were carried out in the microplasma-based deposition system described in Chapter 2. A flow-stabilized, direct-current hollow cathode discharge was generated inside a stainless steel capillary (ID=500 μm) that was biased with a current-regulated, DC high voltage (5 mA - 15 mA, 300-800 V). Ar (100-250 sccm) was fed to

the capillary and oxygen (50-100 sccm) was introduced into the chamber background, maintained at 12 Torr. The hollow cathode discharge was generated by applying high voltage between the capillary (micro-hollow cathode) and one of two anodes: a remote, ring anode located near the capillary exit (Configuration 1) or a graphite deposition chuck (Configuration 2).

In Configuration (1):

- The MHCD circuit was completed between the capillary (cathode) and remote ring anode,
- the graphite deposition chuck was floating, i.e., the chuck was electrically isolated from the rest of reactor via ceramic electrical break, and
- the deposition substrate was isolated from the graphite chuck using a large glass slide.

In Configuration (2)*:

- The plasma circuit was completed through the grounded graphite deposition chuck,
- a CuBe clip made electrical contact with both the deposition substrate and the conductive graphite chuck, and
- the remote ring electrode was grounded during deposition.

*In Configuration 2, ammeters were connected from the ring electrode and graphite chuck to ground. During plasma operation, the ring electrode read no current, and the ammeter on the chuck confirmed that all of the plasma current was sunk through the chuck to ground. The latter was true for all experiments, even when depositing on dielectric substrates, as will be discussed below.

Organometallic precursors $Cu(hfac)_2 \cdot H_2O$, $Cu(acac)_2$, or $Y(hfac)_3 \cdot H_2O$ (STREM, Sigma Aldrich) were sublimed at 23 C, 130 C, and 120 C in 10-50 sccm Ar sweep gas, respectively, and mixed with the main Ar/O_2 gas feed to hollow cathode. A variety of deposition substrates were studied, both conducting (degenerately-doped Si, Cu (100), polycrystalline molybdenum, rolled titanium, aluminum, and tungsten) and insulating (spinel, quartz, sapphire, magnesium oxide, and borosilicate glass). The substrate chuck, 5 - 20 mm downstream from the capillary exit, was static or raster-scanned in a serpentine pattern at a rate of 200 μm/s during growth of CuO and YF_3.

The deposited films were imaged with an FEI XL30 SEM, and composition (C and F contamination) was quantified using an extended range EDAX Element Silicon Drift Detector [86] at 15keV electron beam energy. XRD was performed using Cu Kα radiation on a PANalytical Empyrean diffractometer, with -4 degree offset to suppress the Si substrate peak.

5.3 Results

5.3.1 Deposition on floating versus grounded substrates

The electrostatic environment during deposition, as well as substrate charging, have a very pronounced effect on the resulting morphologies of CuO deposited from $Cu(hfac)_2$. Figure 5.1 (a,d) and (b,e) illustrate this drastic change in morphology under identical growth conditions, i.e., precursor flux, gas flows, substrate distance from plasma jet (~8 mm), plasma current (8.5 mA), and chamber pressure (12 Torr) were all held constant. Deposition on a conductive Si substrate with a grounded chuck (panel (b)) yielded a dense, thin film with >20 at% fluorine, whereas, deposition on the same Si, but with the substrate and chuck both floating (panel (a)), resulted in vertically aligned CuO wires

with low (< 5 at% fluorine) content (panel (f)). Similar behavior occurred on the Mo substrate (panels (g,h,i)), and more generally for all conductive substrates, when in a floating electrical configuration, i.e., substrate on a glass slide, with the graphite deposition chuck as ground. Moreover, these experiments demonstrate that incorporation of F, dictated by the whether the substrate is electrically floating versus grounded, dictates the CuO morphology, i.e., CuO nanowires can be grown with a non-fluorinated $Cu(acac)_2$ precursor on a grounded Si substrate (panel (c)).

Deposition of CuO from the fluorinated $Cu(hfac)_2$ precursor on a variety of insulating and conductive materials, for both floating and grounded chuck configurations, generally followed the aforementioned trends (see Figure 5.2), that is, floating substrates giving nanowire-like morphology, as outlined in Figure 5.1. A few exceptions to this trend occur, which provide some insights into the importance of substrate charging during deposition. First, in Figure 5.2 Row (2), we expect CuO nanowires or nanostructures to grow on a dielectric, but we instead observe a loss of crystallinity and, in the cases of sapphire and MgO, dense films are seen. It should be noted that deposition on dielectric substrates on a grounded chuck (Row (2)) was possible due to the small size (5x5 mm^2) of the coupons. In this case, interestingly, the plasma circuit could still be completed through the chuck, resulting in a uniform secondary glow around the dielectric substrate (see Figure 5.3). Given the morphology and high fluorine content of these two films, it is likely that the secondary glow provided a charge dissipation pathway to the chuck, effectively mimicking a grounded substrate. For the other Row (2) samples, which were considerably larger than 5x5 mm^2, we hypothesize that the secondary glow was not uniform, e.g., the plasma jet plume was asymmetrically deflected to the grounded graphite chuck, allowing certain regions of the sample to differentially charge - recovering the floating substrate morphology and low F content. Moreover, this charging is likely to be more prevalent directly beneath the capillary centerline, from which the plasma jet plume was defected

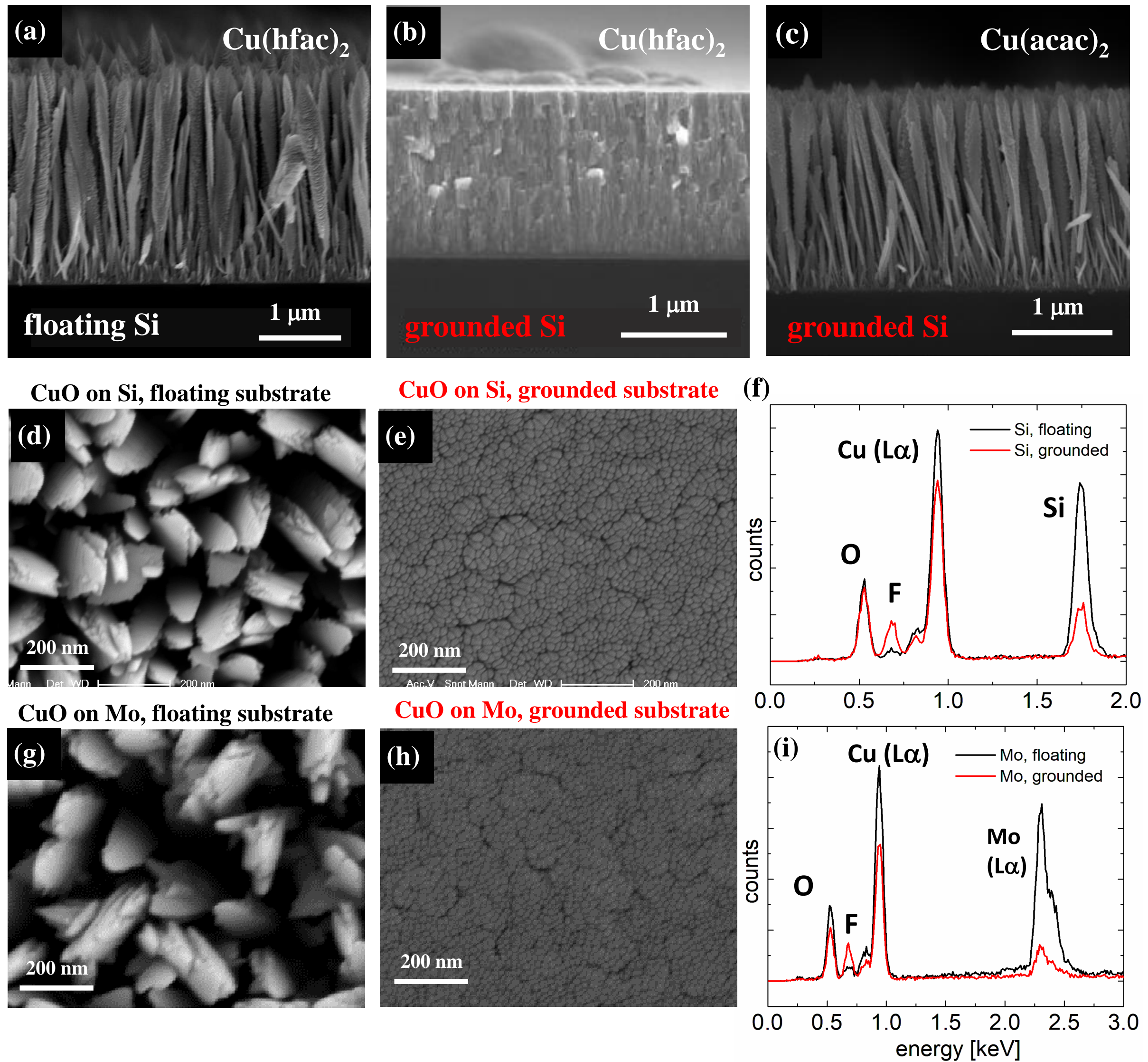

Figure 5.1: Example of how surface charging and precursor affect the morphology of CuO films deposited on (a,d) floating Si, (b,e) grounded Si, (g) floating Mo, and (h) grounded Mo substrates with a microplasma jet. Panels (b) and (c) compare the effect of using fluorinated precursor ($Cu(hfac)_2$) versus non-fluorinated ($Cu(acac)_2$) for the grounded Si substrate case. Panels (f) and (i) show EDAX data of film contamination with C and F for the Si (floating and grounded) and Mo (floating vs. grounded) cases highlighted in (d,e) and (g,h), respectively. Plasma deposition conditions are detailed in the text.

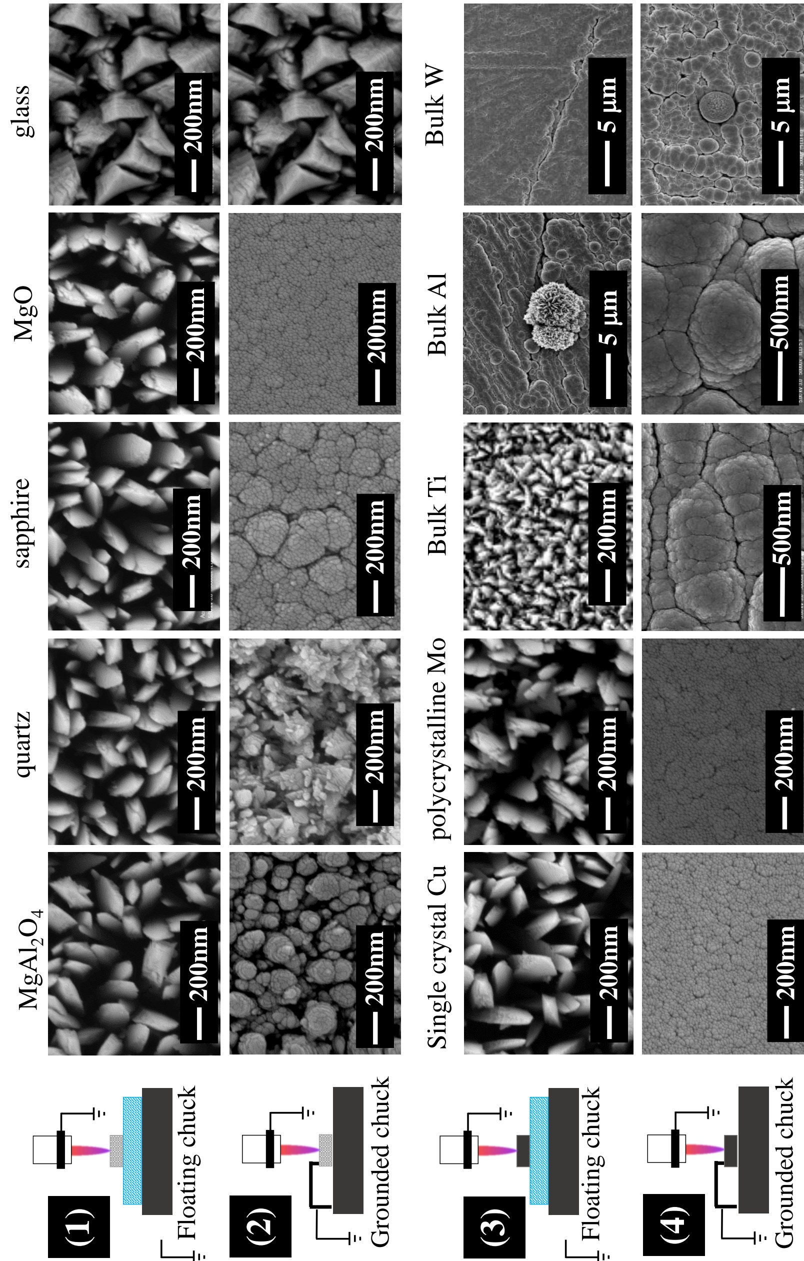

Figure 5.2: Example of how substrate electrical configuration (floating vs. grounded) and sample conductivity (insulators vs. conductors) affect the morphology of CuO films deposited via microplasma jet from $Cu(hfac)_2$ precursor. Plasma conditions were 150 sccm Ar : 50 sccm O_2 in background, 8.5 mA, and 12 Torr. Rows (1)-(4) represent deposition on insulator + floating chuck, insulator + grounded chuck, conductor + floating chuck, and conductor + floating chuck, respectively.

to the grounded chuck. Additionally, while all substrates in Row (3) were floating, we observed dense films and higher fluorine content for two of the three bulk metal substrates. In the former cases (Al and W), the large substrate was able to sink or distribute charge build-up while in contact with the plasma jet, resulting in less surface charge than would have be experienced at the surface of a dielectric under the same jet. The cauliflower-like nodule or secondary nanostructure 'growth' on Al, may therefore be due to insulating debris on the surface, leading to charging and necessarily nanowire-like features.

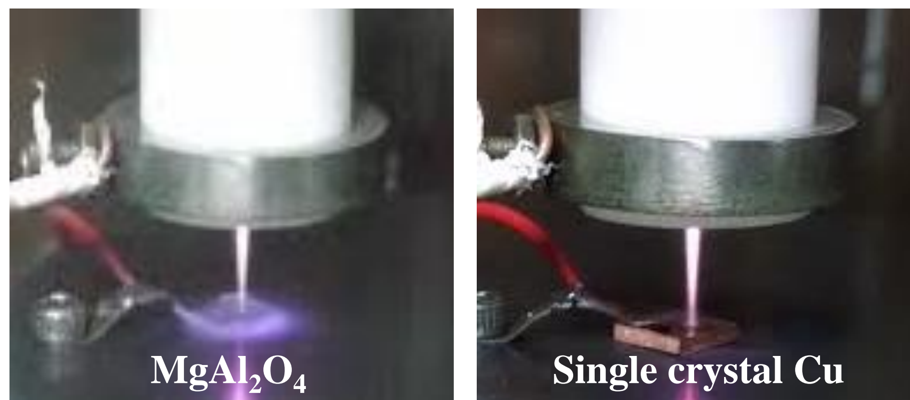

Figure 5.3: Example of the secondary glow phenomenon during CuO deposition occurring on an insulting substrate ($MgAl_2O_4$), but grounded chuck, versus a directly grounded single crystal Cu substrate. The uniform secondary glow above the small (insulating) $MgAl_2O_4$ substrate is thought to dissipate any surface charge, resulting in a more grounded environment, leading to a dense film of nanoscale aggregates (like all grounded substrates) instead of larger nanowires.

5.3.2 Plasma jet - substrate distance

Fluorine contamination, and the resulting CuO film morphology, was previously shown to correlate strongly with a grounded vs. floating substrate. A similar correlation was also seen as the capillary-substrate (jet-substrate) distance was changed, namely larger jet-substrate distances resulted in more fluorine, and for floating substrates. As previously mentioned, Wild *et al.* reported [85] a decrease in charge accumulation on

a dielectric surface as the plasma - substrate distance was increased. Likewise here, we see a significant increase in fluorine content for floating conductive substrates at large jet-substrate distances, suggesting that there may be less charge accumulation, as in the case described by Wild. Figures 5.4 (a) and (b) show deposits on degenerately-doped (conductive) Si at plasma-substrate distances of 7 mm and 15 mm, respectively. The same depositions were conducted on borosilicate glass at the same distances (panels (c) and (d)), and no change in morphology or fluorine content was observed. As such, we hypothesize that as the jet-substrate distance increases, the charge buildup on the conductive silicon is less, and unlike glass, the (conductive) Si can distribute the charge through the bulk of the substrate, making the charge at the surface and growth front significantly less than in the case with the dielectric.

5.3.3 Plasma current

Altering the plasma operating current during deposition was found to be another method of tuning fluorine content in the deposited film. For example, EDAX data and the F, O, and Cu content of various CuO films deposited at 3, 8.5, and 14 mA on conductive Si (electrically floating) at 7 mm jet-substrate distance are shown in Figure 5.5 and Table 5.1.

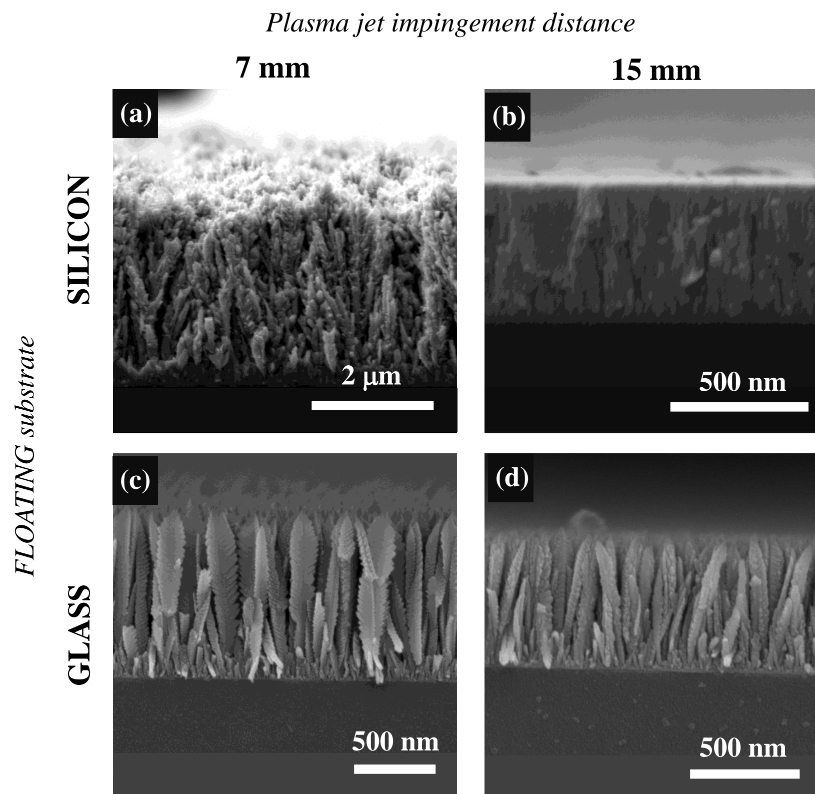

Figure 5.4: Example of how jet-substrate distance can affect the charge state at the growth front for CuO deposition on consucting Si versus glass. No change in morphology occurs on glass, which always charges, no matter the distance; the same is not true for the conducting Si.

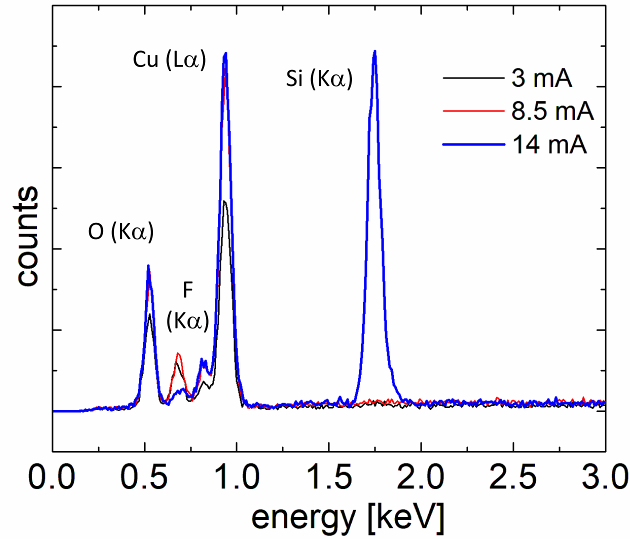

Figure 5.5: EDAX spectra of CuO deposits on a floating Si substrate for various plasma jet currents.

Current [mA]	O at%	F at%	Cu at%
3	42.9	21.7	35.3
8.5	42.6	18.5	38.9
13	49.9	8.2	41.9

Table 5.1: F, O, and Cu content of CuO films presented in Figure 5.5. Data are atomic % based on EDAX spectra.

Overall, higher plasma currents led to lower fluorine contamination and (as a result) higher film crystallinity. This trend is likely due to the fact that higher plasma currents deliver more cumulative charge to the substrate and a higher electrostatic potential at the growth front (i.e., the sample floats up), in similar fashion to the morphology results for insulated vs. grounded substrates discussed in Section 5.3.1.

5.3.4 Deposition of YF_3 from $Y(hfac)_3 \cdot H_2O$

YF_3 and YOF_x are currently being investigated as refractory coatings for plasma etch tooling and optical systems due to their high temperature and chemical stability in the presence of fluorine/oxygen plasmas and broadband transmission in the UV-vis-IR range, respectively. Controlling the stoichiometry and morphology of such coatings, as well as depositing them on a variety of surfaces, are therefore very important. Toward this end, we have explored if the aforementioned ability to tune the level of F-incorporation with substrate electrical configuration could be used to spray-deposit YOF_x and phase pure YF $_3$ from a hexafluoroacetylacetonate precursor. For example, Figure 5.6 shows SEM and EDAX results for three $Y(hfac)_3 \cdot H_2O$ deposition experiments carried out under different conditions: using degenerately-doped Si substrate that was (1) floating + 8.5 mA plasma current, (2) floating + 3 mA, and (3) grounded + 8.5 mA. Film (1) was a mixed YOF_x deposit (10% O + 65% F), and the F-content decreased by a factor of 2 when the plasma current was lowered from 8.5 $\longrightarrow$ 3.0 mA (Film (1) $\longrightarrow$ Film (2)). When the substrate was grounded, oxygen was not detected in the film by EDAX, and pure YF_x was obtained. These data are consistent with the aforementioned CuO experiments where lower plasma current and grounded samples result in less charging at the deposition front, and hence higher F-content films. The film grown at 3 mA + floating chuck had remarkable uniformity and very low porosity (as-grown), and it was further annealed in UHV at 300 C for 1 hr (see Figure 5.6). XRD patterns of these two films are given in Figure 5.7; peaks in the annealed sample correspond to the (020), (111), and (210) orthorhombic reflections of YF_3.

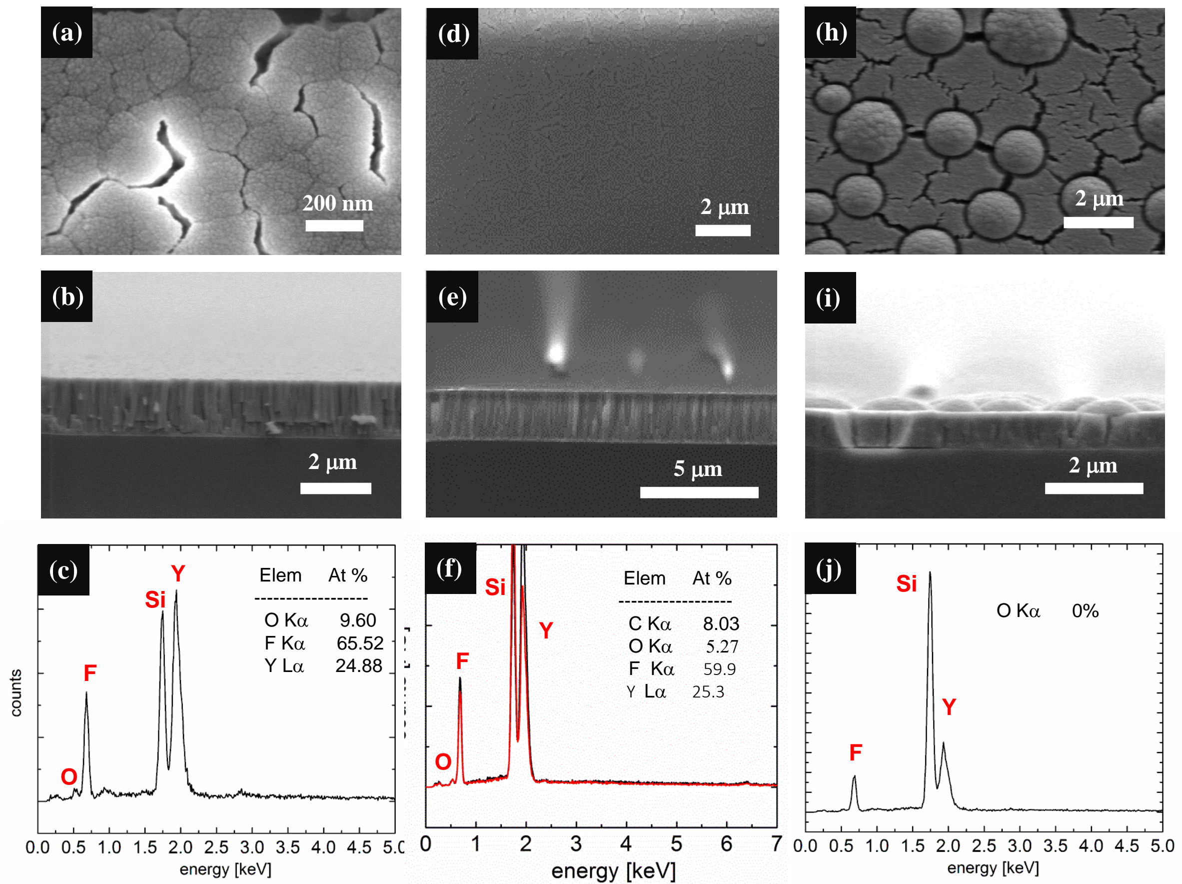

Figure 5.6: SEM and EDAX data for YOF_x and YF_x films deposited on a degenerately-doped Si substrate using $Y(hfac)_3$ precursor at (a-c) 8.5 mA plasma current + floating substrate, (d-f) 3 mA + floating substrate, and (g-i) 8.5 mA + grounded substrate. Note that the grounded substrate film had no observable oxygen signal via EDAX.

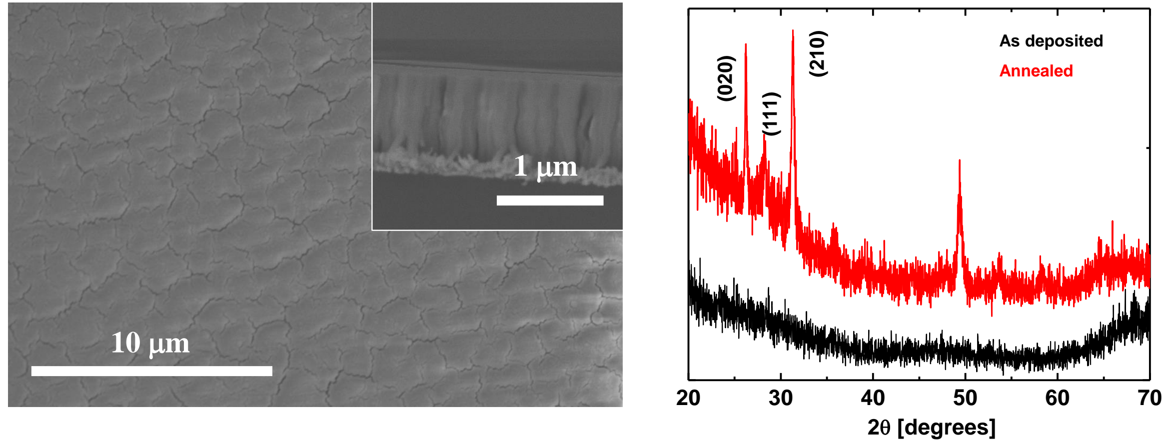

Figure 5.7: SEM of an annealed (300 C, UHV, 1 hr) YF_x film deposited from Y(hfac)$_3$ precursor at 3 mA with a floating substrate. XRD spectra for the as-grown (black) and annealed (red) samples are also shown, with the (020), (111) and (210) peaks of the orthorhombic phase of YF_3 noted.

5.4 Discussion

The deposition experiments described in this chapter clearly demonstrate that the electrostatic configuration of the substrate, its ability to distribute or dissipate charge when exposed to the plasma jet, and the use of acac vs. hfac (fluorine containing) precursors all affect the morphology and C/O/F contamination levels in the resulting films. Plasma jet exposure of the substrate leads to surface charging that likely repels electronegative F species created in the reactive plasma environment. Additionally, it has been shown that nanoparticles and clusters within a plasma take on a negative surface charge due to electron collisions. These charged nanoparticles will interact very differently with a floating (charged) vs. grounded substrate, namely that the former will result in longer diffusion times [78]. Longer diffusion times would enhance the likelihood of forming crystalline structures on the surface, as well as increased opportunity for fluorine species to react with oxygen or carbon species to form volatile compounds that are removed from the surface in vacuum [87]. This simplified picture is not meant to

understate the complexities of surface chemistry and plasma-initiated reactions occurring at the growth front, but rather to communicate general observations that may be helpful in choosing deposition conditions and film precursors. Plasma-substrate distance and plasma current can also be used to affect the level of surface charging, and hence, the resulting film morphology. In general, lower currents and greater distances resulted in less charging, which favor a more dense, nanoparticle/aggregate-like morphology compared to crystalline nanowire-like structures.

5.5 Conclusions and future work

In this chapter, observations regarding substrate electrostatics and deposition with a specific class of fluorine-containing precursors were presented. Higher fluorine incorporation during deposition was associated with less substrate charging, due to using a grounded chuck, lower plasma current, or large substrate-plasma distance. This observation was used to manipulate fluorine content in a YOF_x film to achieve oxygen-free YF_3 from a precursor containing oxygen. Future experiments involving biasing the deposition chuck to large negative voltages ($>$ -270 V, the MHCD voltage) should be conducted. Results of deposition on biased chucks should mimic those on a substrate that has charged up under the jet and would therefore repel fluorine, retard agglomeration, and increase diffusion times in the same manner.

Chapter 6

Microplasma-deposited materials for electrochemical energy storage

This chapter explores the application of microplasma-deposited thin film materials to electrochemical energy storage, specifically for high surface area electrode materials for pseudo- and micro-supercapacitors that store charge via Faradaic charge transfer processes. Materials of interest include RuO_2, NiO, MnO_2 and a mixed oxide system, $Ni_{1-x}Co_xO_y$. The merits of using microplasmas for fabrication of these devices will be highlighted, and include the ability to (i) directly deposit high surface area oxides onto current collectors; (ii) tune the size of the deposited nanostructures, which is shown to have a profound effect on device performance; and (iii) easily combine the spatially-localized nature of microplasma deposition with standard foundry techniques to fabricate microscale energy storage devices.

6.1 Introduction to electrochemical capacitors

Electrochemical energy storage in the form of electrochemical capacitors has been of great interest for years because their specific power and energy bridge the gap between conventional capacitors and batteries. Similar to a normal capacitor, energy is stored in the form of a potential difference between two electrodes with the total, ideal *capacitance* defined as

$$C = \frac{Q}{V} \tag{6.1}$$

where the electrodes are charged to $+/-Q$ with a potential V between them. However, unlike the traditional capacitor, electrochemical capacitors exhibit much higher specific energies and lower specific powers, more like those of a battery. This is depicted in the Ragone plot in Figure 6.1, where various energy storage devices are compared based on their available energy (horizontal axis) and how quickly it can be delivered (vertical axis).

6.1.1 Electrical double layer capacitors (EDLCs)

There are two main types of electrochemical capacitors, the first being the electrical double layer capacitors (EDLCs). These capacitors store energy via an electrochemical double layer or Helmholtz layer at the surface of the electrodes when ionic charges from the electrolyte accumulate at the electrode surfaces [88]. The charging process entails physical adsorption of ionic species to the electrode surface and is non-Faradaic (i.e., no electochemical reactions are occurring). EDLC electrodes are typically made from high surface area carbon or other highly porous, conducting electrodes (metals and doped

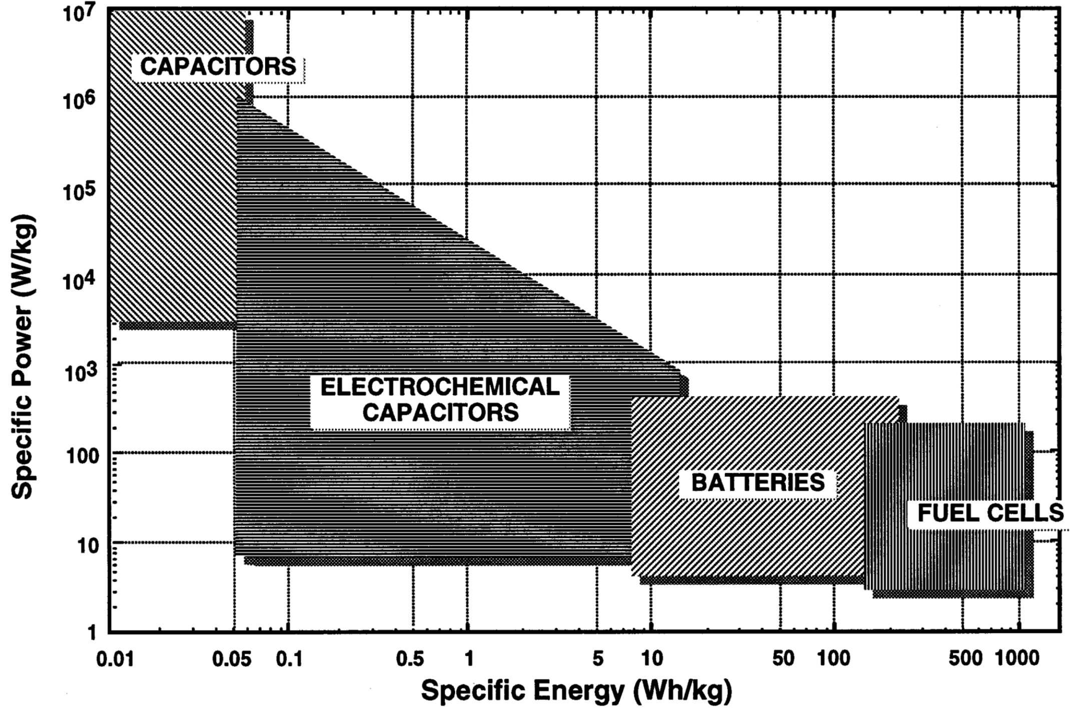

Figure 6.1: Ragone plot showing the specific power and energy of available energy storage technologies. From [88]

oxides). The capacitance of an EDLC is given as

$$C = \frac{\epsilon_r \epsilon_0}{d} A \tag{6.2}$$

where ϵ_r is the relative permittivity of the medium at the electrical double layer, ϵ_0 is the permittivity of vacuum, d is the thickness of the double-layer and A is the specific surface area of the electrode. The charge separation and accumulation process at the electrode surfaces is shown schematically in Figure 6.2. The main factors that contribute to overall capacities are the electrolyte used and the electrode surface area. Many high surface area carbons such as activated carbon, carbon nanotubes, aerogels, and graphene have been and are being explored for these applications [89]. The main advantage of the EDLC storage mechanism is excellent cycling stability; however, EDLCs generally have

lower specific capacities, e.g., < 200 F/g, even for carbon aerogels.

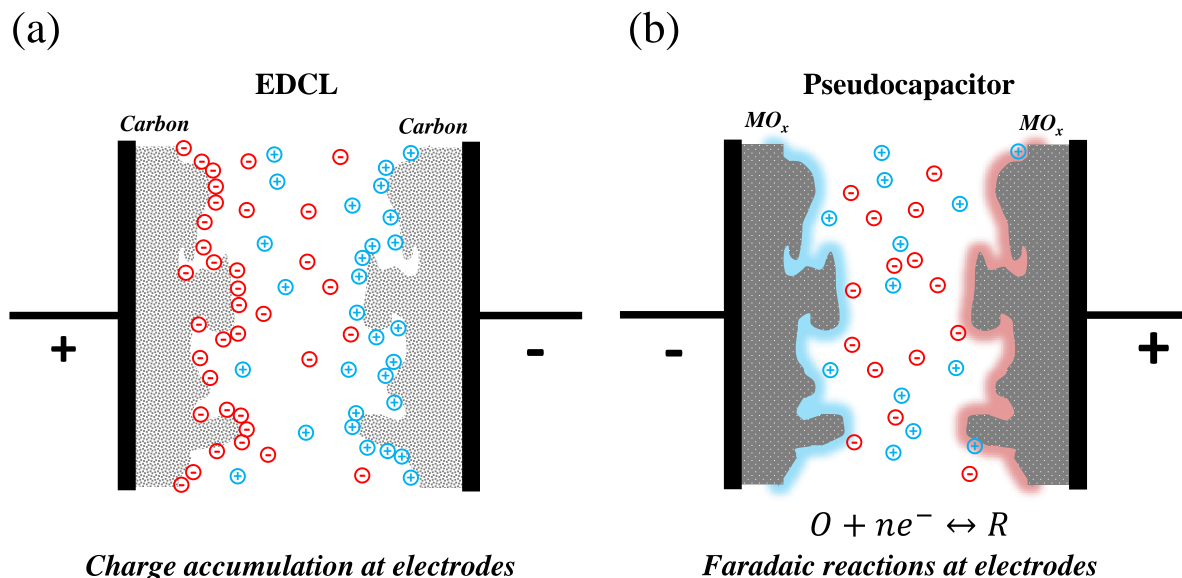

Figure 6.2: Schematic of storage mechanisms of electrochemical capacitors. The EDCL capacitor (a) stores energy via charge accumulation at the electrode surfaces and pseudocapacitors (b) via Faradaic charge transfer reactions at and involving the surfaces of the electrodes.

6.1.2 Pseudocapacitors

The second class of electrochemical capacitors is the pseudocapacitor (PCs). In this device, reduction-oxidation, or Faradaic reactions occur at the electrode surface when the double layer forms in the electrolyte. Electrode materials in these systems are most often transition metal oxides and some polymers that can undergo redox reactions during charge/discharge cycling. The theoretical pseudocapacitance of an electrode is given by

$$C = \frac{nF}{MV} \tag{6.3}$$

where n is the number of electrons involved in the redox reactions, F is Faraday's constant (96485 C/mol e), M is the molar mass of the oxide, and V is the operating voltage

window [90]. PCs are tantalizing alternatives to the more-developed EDLC because they possess up to 10x higher theoretical capacitance; however, they have yet to be commercialized significantly due to poor cyclablity and (often) low power density [89].

6.1.3 Hybrid capacitors

One way to mitigate the aforementioned issue with PC cycling is to create a hybrid capacitor that uses components from both the ECDL and PC. Two types of these hybrid 'supercapacitors' are under development: (i) an asymetric hybrid with a pseudocapacitive anode and a carbon-based ECDL cathode and (ii) a symmetric, "composite" hybrid capacitor where the redox material and a carbonaceous material is either mixed together (e.g., mixed nanopowders) or constructed in a hierarchical manner (e.g., oxide structures grown on carbon fibers) [90]. An example of a symmetric hybrid capacitor is given below in Section 6.3.

6.2 Pseudocapacitive materials

Many other transition metal oxide materials have been studied as potential electrodes in pseudocapacitor energy storage devices. A diagram of potential pseudocapacitive materials in terms of their specific capacitance is shown in Figure 6.3. Promising candidates include MnO_2, NiO, Co_3O_4, SnO_2, ZnO, TiO_2, V_2O_5, CuO, Fe_2O_3, and WO_3 [90]. Given this suite of metal oxides, and the general need for high surface areas in a hybrid device, we have explored whether microplasma-deposited metal oxide films may be appropriate for such applications. Toward this goal, the following sections present some proof of concept growth studies on RuO_2 and $Ni_{1-x}Co_xO_y$, as well as detailed investigations on the growth and electrochemical testing of NiO on carbon, and fabrication of MnO_2-based microsupercapacitors, with companion electrical characterization.

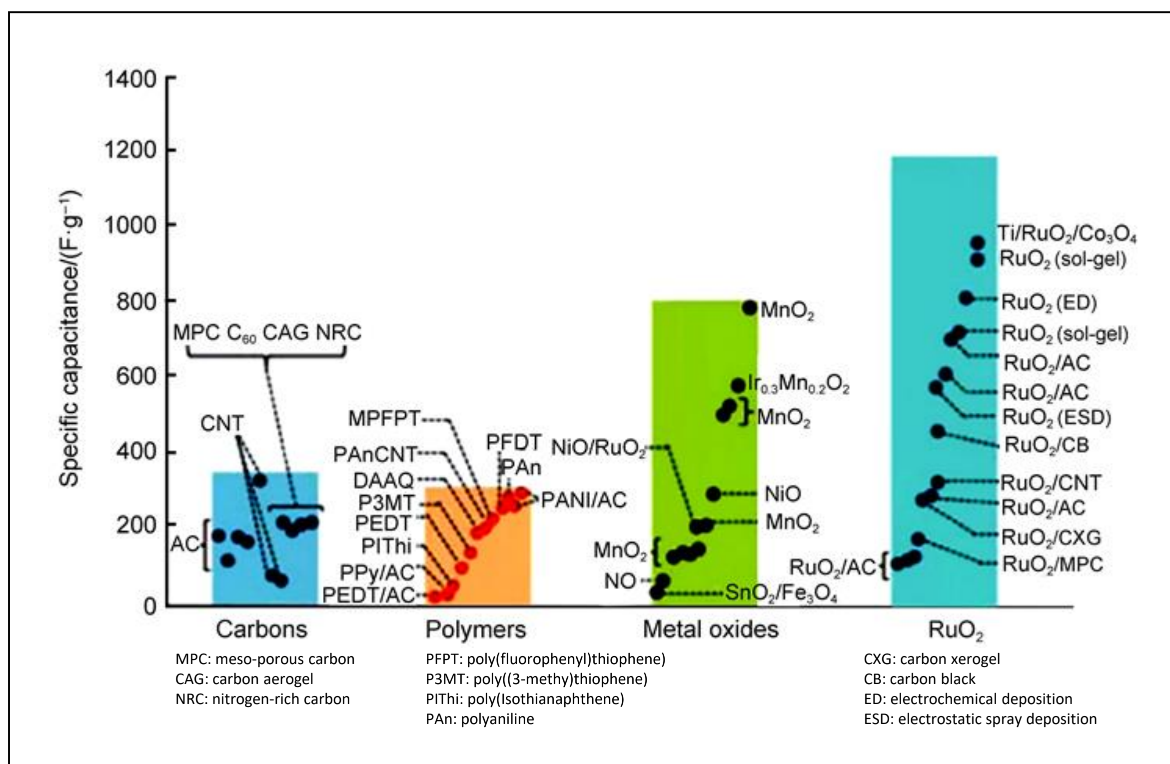

Figure 6.3: Electrochemical capacitor electrode materials and their specific capacitances. Adapted from [91].

6.2.1 RuO_2

RuO_2 is the "original" pseudocapactive material, studied extensively since the 1970's, whose capacitive ability as an electrode was demonstrated via Faradiac charge transfer. The mechanism was later revealed to involve storage of protons from an acidic electrolyte in a hydrated RuO_2 electrode surface [92]. With a theoretical capacity of 1300-2200 F g^{-1} and relatively high conductivity (10^5 S cm^{-1}), RuO_2 seems ideal, and has received much research focus for energy storage. Unfortunately, RuO_2 suffers from low cyclability and high materials cost ($266/oz) [89,92], making its widespread implementation rather unlikely. Notwithstanding, we have explored if microplasmas could be used to deposit these RuO_x materials. In preliminary experiments, a ruthenocene CVD precursor was

introduced into an Ar/O_2 plasma (8.5 mA, 12 Torr), and RuO_x was successfully deposited on a Si substrate, as shown in Figure 6.4. The film had porous character and is made up of 50 nm cube-like nanostructures, whose habit is suggestive of the common tetragonal phase of RuO_2. EDAX was also conducted (Table 6.1) and revealed a modest level of carbon contamination (13 at%), suggesting further optimization of the deposition process is needed, e.g., adding extra O_2 to the jet and/or background to remove C in the film, as well as companion electrochemical testing.

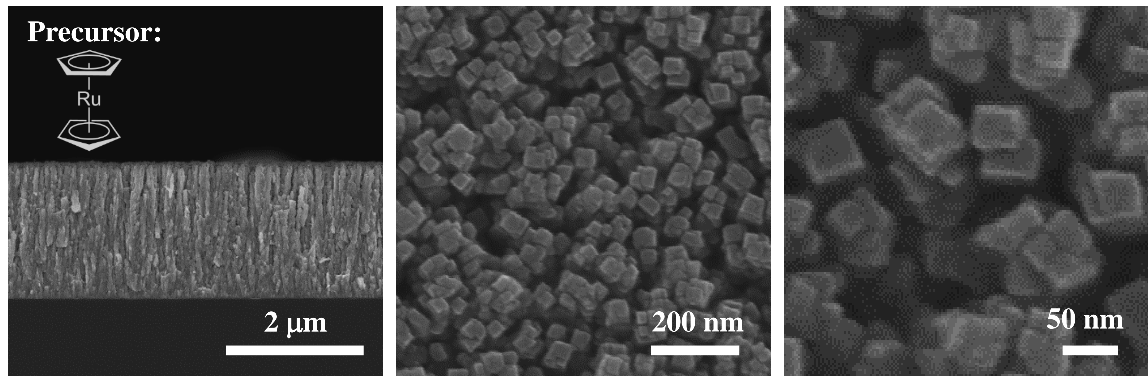

Figure 6.4: Preliminary deposition of RuO_x thin film using an Ar/O_2 microplasma jet with ruthenocene precursor at 12 Torr and 8.5 mA. Side and top views are shown.

Element	atomic %
Ru	33%
O	54%
C	13%

Table 6.1: EDAX analysis of the microplasma-deposited RuO_x nanostructured film shown in Figure 6.4

6.2.2 $Ni_{1-x}Co_xO_y$

In general, transition and mixed metal oxides are attractive materials for next-generation energy storage because they are readily available, cheap, and many have

high theoretical capacitances. However, most exhibit poor electrical conduction, which is usually mitigated by adding a conductive binder such as carbon [93] to form a effective electrochemical electrode. Unfortunately, diluting the redox-active metal oxide only decreases the surface area available for Faradaic charge storage. However, some mixed metal oxides, such as the spinel form of $NiCo_2O_4$, are receiving considerable interest, due in large part to their inherently high electrical conductivity, which eliminates the need for a conductive binder. For example, Windisch *et al.* [94] reported growth of $NiCo_2O_4$ thin films with resistivities as low as 0.003 Ω cm (see Fig. 6.5).

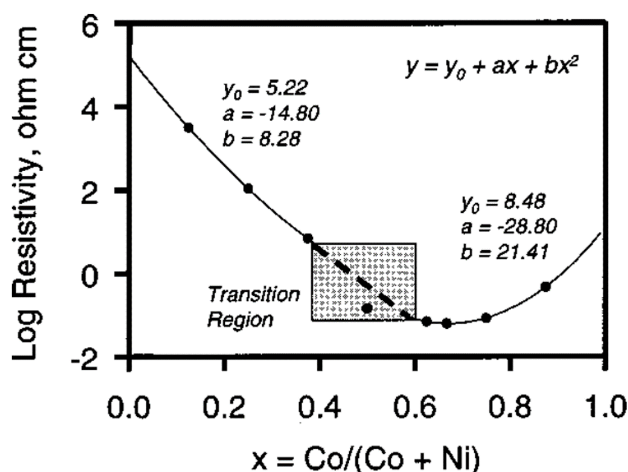

Figure 6.5: Resistivity of several Ni/Co oxides. A minimum is observed for the spinel $NiCo_2O_4$. Adapted from [94].

NiO and CoO also readily form solid solutions, but under the right conditions, can form the spinel $NiCo_2O_4$ phase, or a combination. Various crystal phases and a pseudo-phase diagram of the (Ni,Co)O system in shown in Fig. 6.6 [95]. From this diagram, one can see that a single phase CoO/NiO solid solution is guaranteed above a specific temperature in the 600-800 C range. These authors reported complicated phase relationships within this system and found that heating a spinel-containing sample above 600 C resulted in loss of the spinel and the formation of a solid solution of NiO/CoO;

whereas, heating and cooling the system below 600 C at most compositions resulted in the solid solution and a separate Co_3O_4 phase [95]. These aforementioned measurements therefore suggest that forming the high conductivity spinel phase is highly desirable, but it must be done at low growth temperatures to avoid the miscibility of NiO and CoO. Given the low temperature requirement, and the need for high surface area materials, it seems very promising to growth such films using microplasma jet deposition. Moreover, exploring the (Ni,Co)O system may also prove to be an interesting way to investigate growth conditions within the microplasma jet, given the low-temperature requirements for the formation (and retention) of the spinel phase. Also, the microplasma spray technique has the ability to deposit high surface area, nanostructured thin films that would be excellent candidates for redox-based electrochemical energy storage devices.

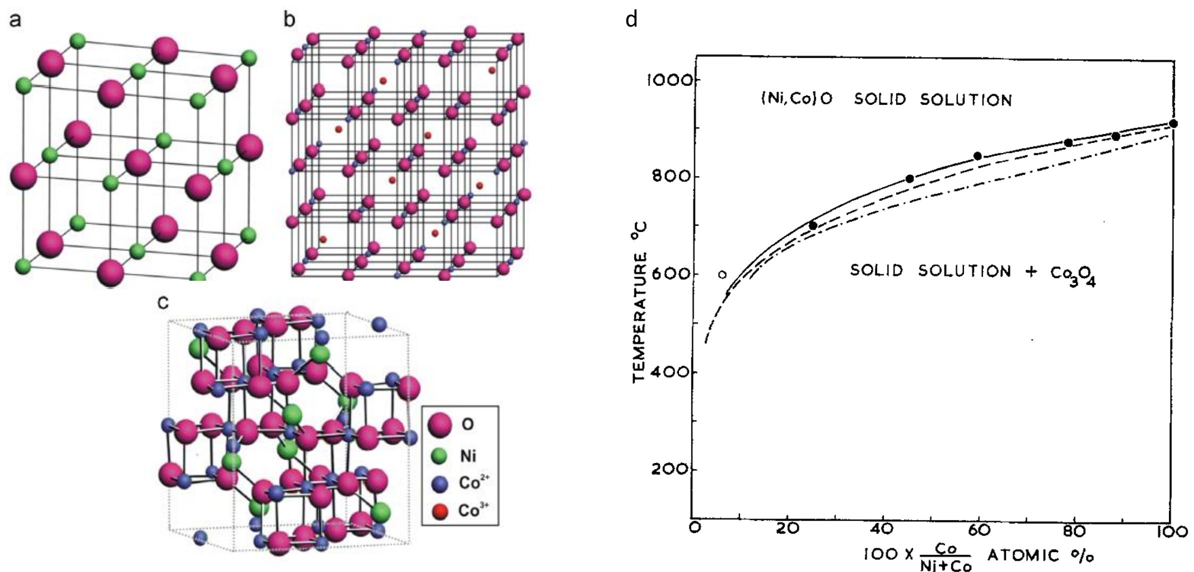

Figure 6.6: Crystal structures of (a) rock salt NiO, (b) Co_3O_4, and (c) Ni-doped Co_3O_4 (the spinel phase $NiCo_2O_4$), from [93]. (d) Pseudo-phase (temperature-composition) diagram [95] for the (Ni,Co)O system. A phase boundary between a single phase solid solution of NiO/CoO region and a two-phase NiO/CoO solid solution + Co_3O_4 region is shown.

Experimental setup

Mixed metal oxide nanostructures were deposited on degenerately doped Si substrates using the microplasma deposition system discussed in Chapter 2. The flow-stabilized, direct-current hollow cathode discharge was used to crack two sublimed organometallic precursors, cobaltocene and ferrocene (STREM), into active growth species (e.g., atoms, ions, and clusters), which were directed towards the substrate under supersonic flow conditions. Oxygen (5-20 sccm) was introduced directly into the capillary cathode gas feed. The substrate stage was located 8-12 mm downstream from the capillary exit. Both precursors were housed in stainless steel "sublimation cells" and were heated to a desired temperature using fiberglass coated heat tape. The precursor flux to the plasma, and thus the film stoichiometry, was controlled in one of two ways: (1) by adjusting the Ar flow to the sublimation cell containing the precursor or (2) by increasing the temperature of the precursor cell.

Phase and crystal structure of the deposited oxide thin films were analyzed via θ-2θ XRD (with -4 degree offset to suppress Si substrate peaks) using Cu Kα radiation on a PANalytical Empyrean diffractometer. High resolution SEM micrographs were taken on an FEI XL40 SEM and film stoichiometry was determined using energy dispersive x-ray (EDAX) spectra of Ni and Co Kα lines.

Results and discussion

Nanostructured $Ni_{1-x}Co_xO_y$ films of different compositions (X = 0.42 to 0.84) were deposited on silicon substrates, as shown in Fig. 6.7. A variety of film morphologies were obtained, ranging from dense, columnar structures for the lowest Co concentration sample, $X_{Co} = 0.42$, to vertically-aligned nanoblades and nanostructures for $X_{Co} > 0.55$. These films were grown using the $Ni(Cp)_2$ sublimation cell held at 23 C and the $Co(Cp)_2$

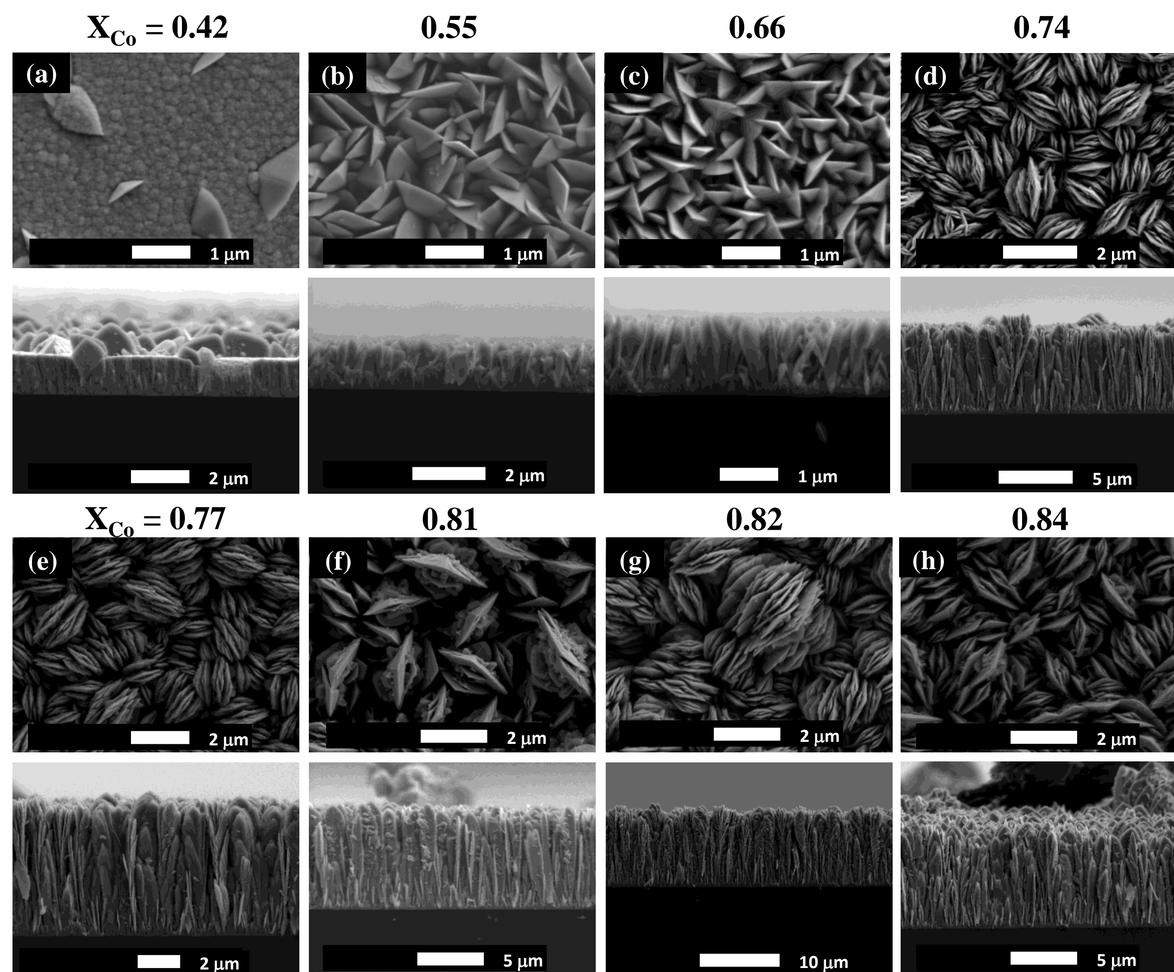

Figure 6.7: SEM images of microplasma-deposited $Ni_{1-x}Co_xO_y$ nanostructured thin films. The mole fraction Co was varied from (a) 0.42 to (h) 0.84. Atomic composition is based on EDAX spectra of the Ni and Co Kα lines.

sublimation cell heated to 36-48 C. The final film composition, as measured via EDAX, could be easily controlled by changing the $Co(Cp)_2$ cell temperature, as depicted in Fig. 6.8. For the $NiCo_2O_4$ spinel, the desired Co mol fraction is $X_{Co} = 0.66$, which was achieve at 40 C for the cobaltocene precursor.

XRD analysis is exceedingly challenging when working with small deposits and thin films. However, the analysis shown in Figure 6.9 suggests:

- Pure phases of NiO and Co_3O_4 were deposited. The NiO deposit was highly tex-

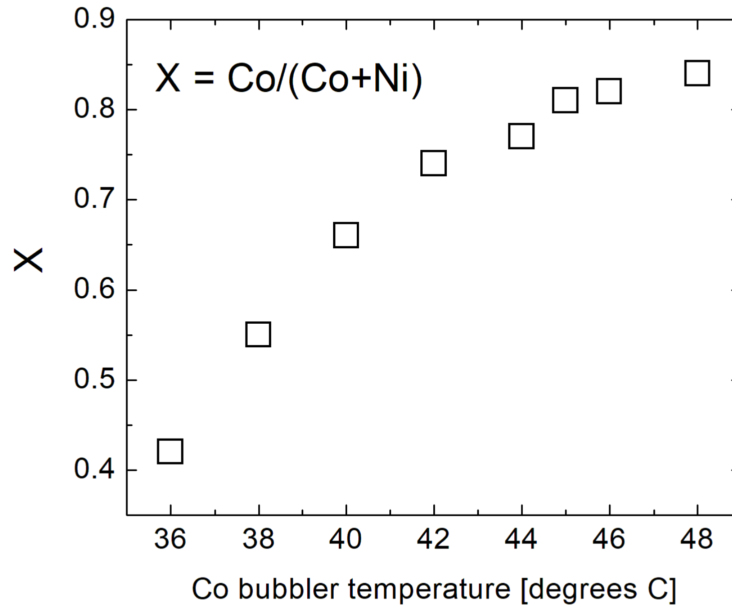

Figure 6.8: (Ni,Co)O film composition (mol fraction Co) as a function of cobaltocene precursor cell temperature. The nickelocene precursor cell temperature was held constant at 23 C.

tured and gave only one, very strong (200) reflection. The cobalt oxide film, on the other hand, showed a weak and fairly broad peak that corresponds to the (111) reflection of Co_3O_4.

- It is unclear if the spinel $NiCo_2O_4$ phase was deposited, as the XRD pattern for the $X_{Co} = 0.66$ (green) suggests. The small, shifted peak near both NiO and Co_3O_4 reflections may suggest the presence of a solid solution, where the lattice parameter is shifted slightly.

- A biphasic, solid solution of NiO and Co_3O_4 was likely obtained for $X_{Co} = 0.88$, as evidenced by the (111) reflections from both oxide phases.

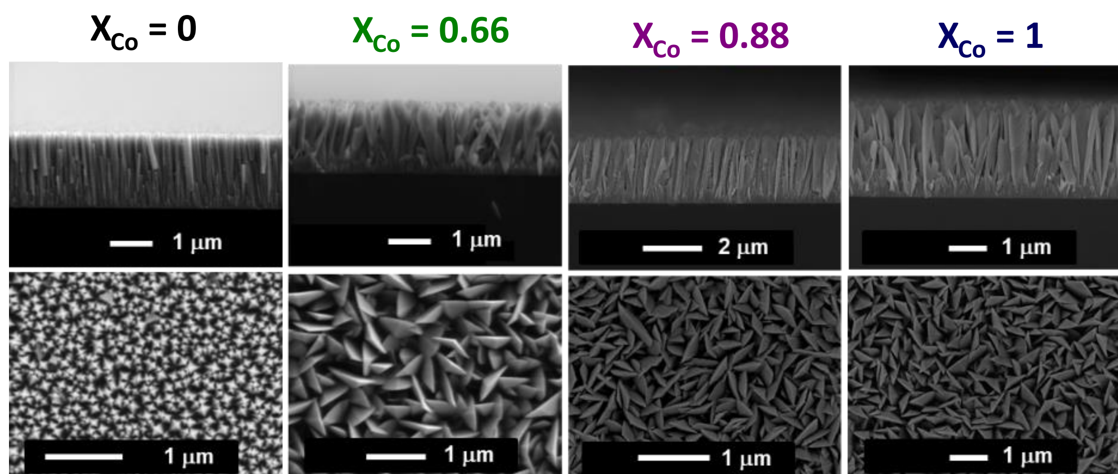

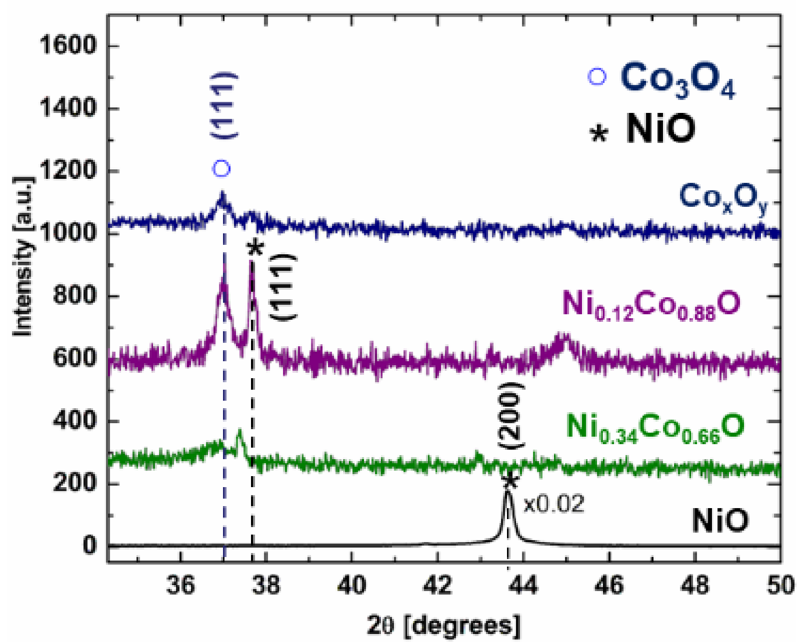

Figure 6.9: SEM images and preliminary XRD data for microplasma-deposited, nanostructured thin films: pure phase NiO, two mixed oxides, and pure CoO.

Concluding remarks

The previous sections have shown how the microplasma-based deposition tool developed in this work can be used to directly deposit biphasic, nanostructured $Ni_{1-x}Co_xO_y$ at various compositions. This is accomplished by simply tuning the amounts of sublimed precursors delivered to the plasma source. SEM also reveals that deposits are composed of high surface area, vertically-aligned nanostructures that would seem ideal for electrochemical energy storage applications. These measurements are underway.

6.3 Nickel oxide nanostructures on carbon fiber for hierarchical pseudocapacitors

Nanostructured metal oxides on various forms of carbon (fiber, paper, nanotubes, etc.) have seen increased interest in recent years as high surface area, redox-active electrodes for pseudocapacitors [90]. In particular, NiO boasts an extremely high theoretical capacitance value of 2584 F g^{-1} (with a voltage window of 0.5 V), but it unfortunately has a rather low electrical conductivity (0.01 - 0.32 S m^{-1} [96]). This latter issue has been somewhat circumvented by forming a composite pseudocapacitor, where nanostructured NiO is mixed with a binder to improve conductivity and achieve high specific capacities and high cyclability, with reported typical performances ranging from 50-1700 F g^{-1} [97–99]. Many routes have been explored to form NiO on carbon, including hydrothermal and solvothermal methods, sol-gel, precipitation, electrochemical deposition, and microwave synthesis.

Microplasma jet-based synthesis, as has been previously shown, allows spray deposition of nanostructured materials on virtually any surface, and moreover, the deposited films are in direct electrical contact with the substrate (current collector), eliminating

the need for binders or post-deposition processing. Direct growth onto the current collector increases the mechanical stability of the system and also decreases the contact resistances. As such, microplasma spray deposition is potentially an easy and direct method to realize high performance pseudocapacitor electrodes in a single step. The following section highlights experimental results on direct spray deposition of NiO onto Toray carbon fiber paper, with companion IV and CV electrical testing of films in a proof-of-concept pseudocapacitor device.

6.3.1 Microplasma deposition on carbon fiber paper

The microhollow cathode discharge was operated at 8.5 mA and 18 Torr with a flow of 150 sccm Ar to the capillary. Approximately 50 sccm O_2 was introduced to the chamber background. A nickelocene precursor was sublimed at 24 C and injected into the plasma jet. The deposition substrate was located 1 cm downstream of the nozzle throat and was raster scanned in a single-pass serpentine pattern to deposit a 0.9 x 0.5 cm^2 or 0.45 cm^2 area film on Toray carbon fiber paper. The NiO film thickness (or size of nanostructures) deposited on the carbon paper could be tuned by adjusting the substrate scanning rate under the jet, i.e., 100 ms vs. 500 ms between each stepper motor pulse to move the deposition chuck. Longer wait times between motor movements resulted in thicker NiO deposits composed of larger nanostructures.

An example of microplasma-deposited NiO on carbon paper is shown in Figure 6.10. As can be seen, the first few fiber layers are confomally covered with sub-50 nm diameter NiO nanostructures ("fuzz") that are similar to those presented in Chapter 4. The NiO features appear to be highly crystalline with facets that are reminiscent of a cubic crystal habit, which is expected for the bunsenite (rocksalt) phase of NiO. It is also interesting to note that exposure of the carbon paper substrate to the plasma, which does indeed

contain oxygen, does not appear to disrupt or damage the carbon fibers. This observation is somewhat expected because the microplasma jet source is a very low temperature plasma, with effective gas temperatures in the 300-700 K range (see Chapter 3 for details). Shadowing of fibers lying deeper within the substrate (paper) thickness certainly occurs, but this is not a significant issue with respect to the electrode's performance in a pseudocapacitor device (see Section 6.3.2), other than perhaps increasing its gravimetric capacity (F/g). In future experiments, it may be possible to pump through the porous fiber paper to cover fibers throughout the entire bulk of the paper.

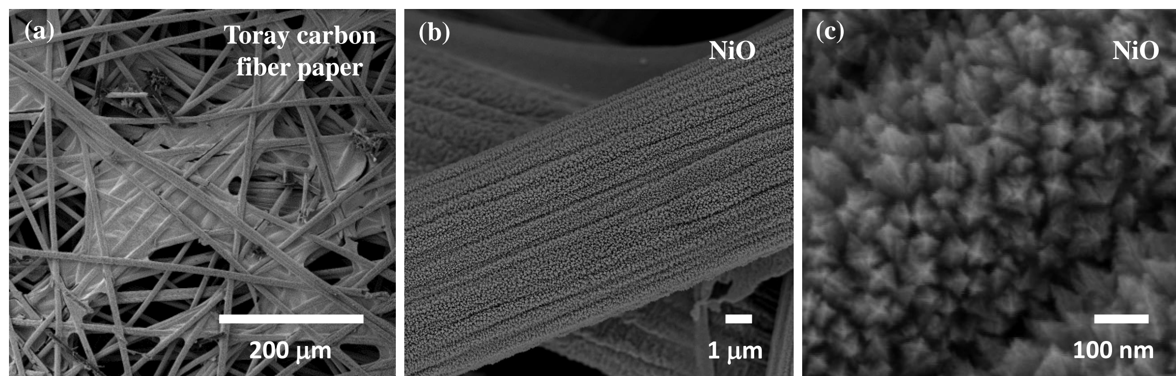

Figure 6.10: Microplasma spray-deposited NiO on Toray carbon fiber paper substrate for pseudocapacitor electrode. Panel (a) is the paper substrate, and (b,c) show various zoom images of the NiO nanostructures.

6.3.2 Cyclic voltammetry of NiO on carbon

The reversible redox behavior of NiO in an alkaline electrolyte is given in Equation (6.4), and involves cycling between the oxide (Ni^{2+}) and oxyhydroxide (Ni^{1+}) phases to reversibly store charge. The aforementioned NiO on carbon samples (Figure 6.10) were tested electrochemically in 0.1 M KOH electrolyte solution using a standard 3-electrode electrochemical cell, with NiO on carbon as the working electrode, a Pt counter electrode,

and an Ag/AgCl reference electrode.

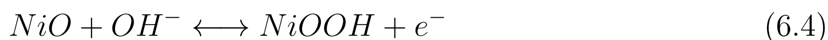

$$NiO + OH^- \longleftrightarrow NiOOH + e^- \qquad (6.4)$$

Cyclic voltammetry (CV, working electrode current response vs. voltage) was performed with a computer controlled Gamry potentiostat at different sweep rates in the 0-0.8 V potential window with respect to Ag/AgCl. The electrolyte was refreshed and outgassed with N_2 for each sample (i.e., NiO deposited with 100 ms vs. 500 ms chuck rastering wait times) and the CV curves shown (see Figure 6.11) were those taken after at least 10 anodic-cathodic sweeps to stabilize the response. It should also be noted that redox peaks tend to shift more positive/negative as sweep rate is increased and this is thought to be due to fast ionic/electronic diffusion rates during the redox reactions made possible due to high surface area and pore structure of nanomaterial electrodes [96].

6.3.3 Results and discussion

Figure 6.11 shows several CV sweeps of NiO deposits on carbon from 0 - 0.8 V at various voltage sweep rates ranging from 10-200 mV/s. Smaller NiO nanostructures (panel(a)) were obtained with faster sample scanning (100 ms wait between moves), and have higher current response than the larger structures deposited at slower chuck scanning rates (panel(b), with 500 ms wait between moves). We also note a larger current response for the anodic peak.

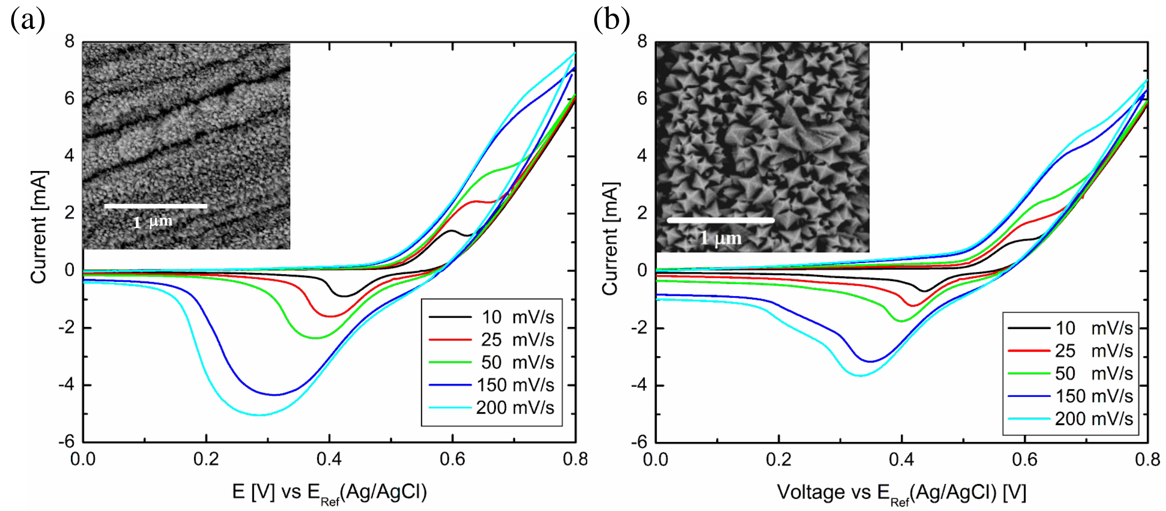

Figure 6.11: Cyclic voltammograms of microplasma-deposited NiO on Toray carbon fiber current collectors in 0.1M KOH electrolyte at various voltage sweep rates. The structures in panels (a) and (b) were deposited with fast (100 ms wait) and slow (500 ms wait) chuck scanning rates. CV curves represent the 10th. consecutive scan obtained at each voltage sweep rate.

Large redox peaks associated with the $Ni^{2+} \longleftrightarrow Ni^{1+}$ transition are clearly visibly in the CV traces, indicating that the electrode behaves in a pseudocapacitive manner to store charge, rather than acting as an EDLC, which would have a more square CV hysteresis loop. Moreover, the smaller NiO structures obtained with fast chuck scanning, clearly provide more redox active surface area for charge storage than the slow-scanned sample, and (necessarily) much more area than the electrical double layer from Toray carbon paper itself. The specific capacity of the NiO on carbon composite pseudocapacitors was calculated using the following:

$$C = \frac{1}{m\nu\left(V_c - V_a\right)} \int_{V_a}^{V_c} I(V)dV \tag{6.5}$$

where m is the mass of the active electrode material (NiO), ν is the potential scan rate, and V_a and V_c are the voltage scan range (anodic to cathodic potentials), and $I(V)$ is the response current as a function of voltage. Inductively coupled plasma-atomic emission

spectroscopy (ICP-AES) was used to obtain an accurate value for the mass of NiO on the electrodes. After CV testing, the NiO samples were dissolved in nitric acid, and along with a dilution series of known Ni^{2+} concentrations, were analyzed using a Thermo iCAP6300 ICP-AES. Specifically, Ni lines at 216.56 nm, 221.65 nm, 231.60 nm, and 341.48 nm were used for quantification. The mass of NiO in the two samples in Figure 6.11 were determined to be 40 μg (sample (a)) 118 μg (sample (b)).

Using these values, we obtain the following results for specific capacity:

Sample	**10 mV s^{-1}**	**200 mV s^{-1}**
Small crystallites (a)	307 F g^{-1}	96 F g^{-1}
Large crystallites (b)	117 F g^{-1}	33 F g^{-1}

Table 6.2: Specific capacities calculated from cyclic voltammograms (Figure 6.11) of pseudocapacitive NiO and carbon fiber electrodes at potential sweep rates of 10 and 200 mV s^{-1}.

As summarized in Table 6.2, we observe modest specific capacities for the NiO on carbon electrodes, the largest being 307 F g^{-1}, which is on par with values typically reported for NiO, and corresponds to the electrode with smaller NiO crystallites. This is suggestive that since redox chemistries are only surface reactions, material morphology and surface area play a key role in determining device performance. It should also be noted that the decrease in specific capacity with increasing voltage sweep rate is a common observation and generally attributed to kinetic limitations of the electrolyte.

To conclude, we demonstrated the ability to directly deposit NiO nanostructures of tunable dimensions on a carbon fiber paper current collector to fabricate composite pseudocapacitor electrodes. Cyclic voltammetry in alkaline electrolyte showed that these electrodes have reasonable specific capacitances, with the smaller, higher surface area material outperforming the others at 307 F g^{-1} at a voltage sweep rate of 10 mV s^{-1}.

6.4 Microplasma spray deposition of vertically-aligned MnO_2 nanostructures for solid-state, planar microsupercapacitors

6.4.1 Introduction

Semiconducting and transition metal oxide nanowires and nanostructures have been of great interest in the development of a wide range of sensing, energy storage, and energy conversion technologies. However, integration of such nanostructures is inherently challenging, especially as the size of the device decreases. Localized and directed growth of nanostructures (wires) is feasible via chemical vapor deposition (CVD) and vapor-liquid-solid (VLS) epitaxy using a patterned catalyst, where structures only grown on the patterned catalyst itself, or in combination with electrodeposition processes on conductive patterns. However, CVD and VLS often require high temperatures, and electrodeposition often yields materials with low crystallinity. Micro-patterning of nanostructures grown via solvothermal methods also remains a challenge, as these generally require high temperatures, surface directing agents, and post-synthesis calcination, none of which are amenable to most foundry patterning techniques.

Interest in microscale patterning of semiconductor and transition metal oxide nanostructures has increased over the last decade, largely driven by the desire to fabricate microbatteries and microsupercapacitors for on-chip energy storage [100]. Several approaches exist to create these "micro" device structures, including inkjet and/or screen printing of a nanopowder suspension, and electrophoretic deposition of a charged slurry onto a patterned electrode. Unfortunately, these methods are low resolution and frequently suffer from poor active layer adhesion. Other methods involve *in situ* synthesis of the electrode active layer; for example, electodeposition of an active material onto a

patterned electrode, and for EDLC-type microsupercapacitors, laser scribbing of photoresist, which results in patterned areas of carbonaceous material. However, a general, direct method for the deposition of pseudocapacitive materials (i.e., nanostructured transition metal oxides) that is compatible with foundry micropatterning techniques remains a challenge.

Herein, we present an approach that utilizes standard photolithography techniques, in combination with microplasma-based deposition of vertically-aligned nanostructures, to create patterned features on micron length scales. This technique provides a general route to nanostructure growth and has been previously reported in [47]. Most significantly, we present a foundry-compatible technique for highly localized, fast deposition and patterning of nanostructured materials for microscale device fabrication. This hybrid microplasma-foundry lithography method is used to fabricate a solid state MnO_2 microsupercapacitor, with areal and volumetric capacitances of 600 μF cm^{-2} and 25 F cm^{-3}, respectively.

6.4.2 Experimental details

A combination of standard photolithography and microplasma-based deposition was used to fabricate microsupercapacitor devices (see Figure 6.13). A negative resist, AZ 2020 nLOF was used for this process due to its relative thermal stability (up to 250 C). Transparency photomasks of interdigitated electrodes with 50 μm thick "fingers" were used (Figure 6.12). The negative resist was spun onto silicon substrates with a thermally grown 250 nm oxide layer. The samples were exposed through the masks using an Karl Suss MJB UV400 contact aligner and developed. The resulting photoresist features were about 2 μm high. A 20 nm Cr adhesion layer was then ebeam evaporated through the patterned photoresist, followed by deposition of 100 nm of Au to form electrical contacts.

The active electrode material, namely NiO (as a test system) or MnO_2, was then spray deposited onto the photoresist/electrode patterns via microplasma jet, followed by liftoff of the photoresist.

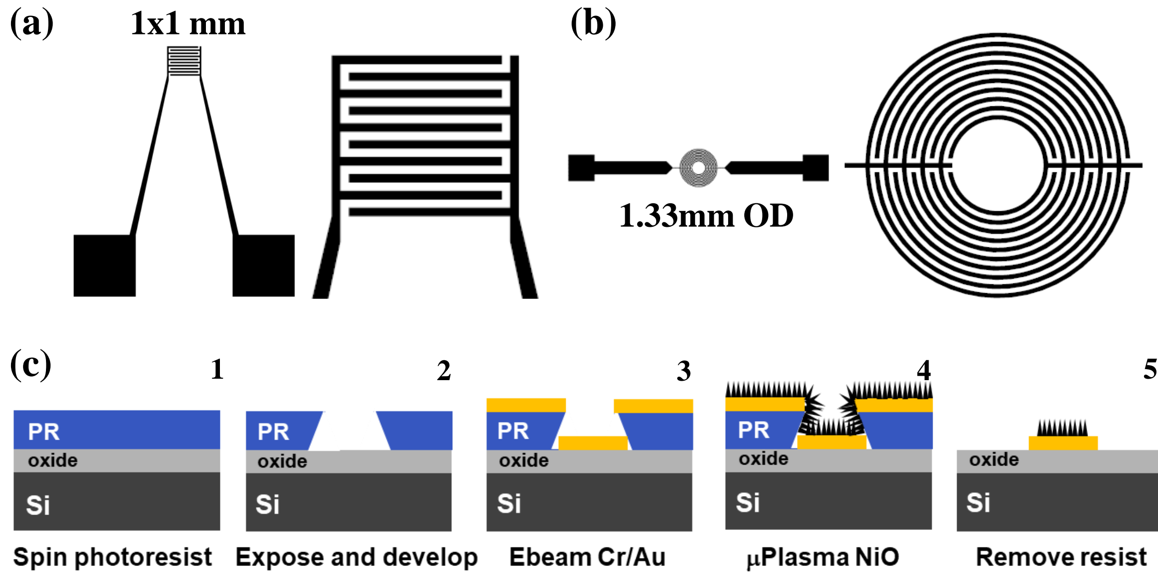

Figure 6.12: (a,b) Photomasks of interdigitated electrode structures used to to fabricate microsupercapacitors. The square electrode is 1x1 mm^2, with 50 μm wide fingers fanned out to large metal contact pads for testing. The electrode finger spacing is also 50 μm. The circular electrode has an outer diameter of 1.33 mm and 50 μm wide fingers. (c) Process flow developed to fabricate microsupercapacitor devices, which combines standard microelectronics foundry techniques and microplasma jet spray deposition.

NiO films were deposited using the aforementioned methods (see Chapter 2 and 4), and vertically-aligned MnO_2 structures were directly deposited onto the masked devices using a manganese(II) hexafluoroacetylacetonate hydrate ($Mn(hfac)_2$ H_2O) precursor. The microplasma jet was run with 150 sccm Ar and 5 sccm O_2 with 12 Torr chamber pressure. The Mn precursor was sublimed at 85 C and entrained in 40 sccm Ar and injected directly into the plasma jet. The deposition substrate was raster scanned under the jet over a 1x1 mm^2 area in a serpentine pattern with 30 ms wait time between XY stage motor movements, giving a total deposition time of 5 minutes. The deposits and

resulting devices were imaged in an FEI XL30 SEM, and XRD was conducted on a larger deposit using a PANalytical Empyrean diffractometer.

A polyvinyl alcohol/phosphoric acid mixture served as the gel electrolyte; 1.8g of 85wt% H_3PO_4 and 1.5g of PVA were mixed in 15 mL of DI water and gently heating until the PVA dissolved. This solution was allowed to cool and drop-cast onto the device electrodes. Electrochemical testing of the devices was carried out on a computer controlled Gamry Series G 300 potentiostat.

6.4.3 Results and discussion

Lithographically-patterned microplasma deposits

The lithography and deposition procedures were first debugged and optimized using NiO, the results of which can be seen in Figure 6.13. Pattern transfer had high fidelity and photoresist lift off was effective, leaving behind a 300 nm thick film of crystalline NiO nanostructures with good adhesion on the circular interdigitated electrode pattern.

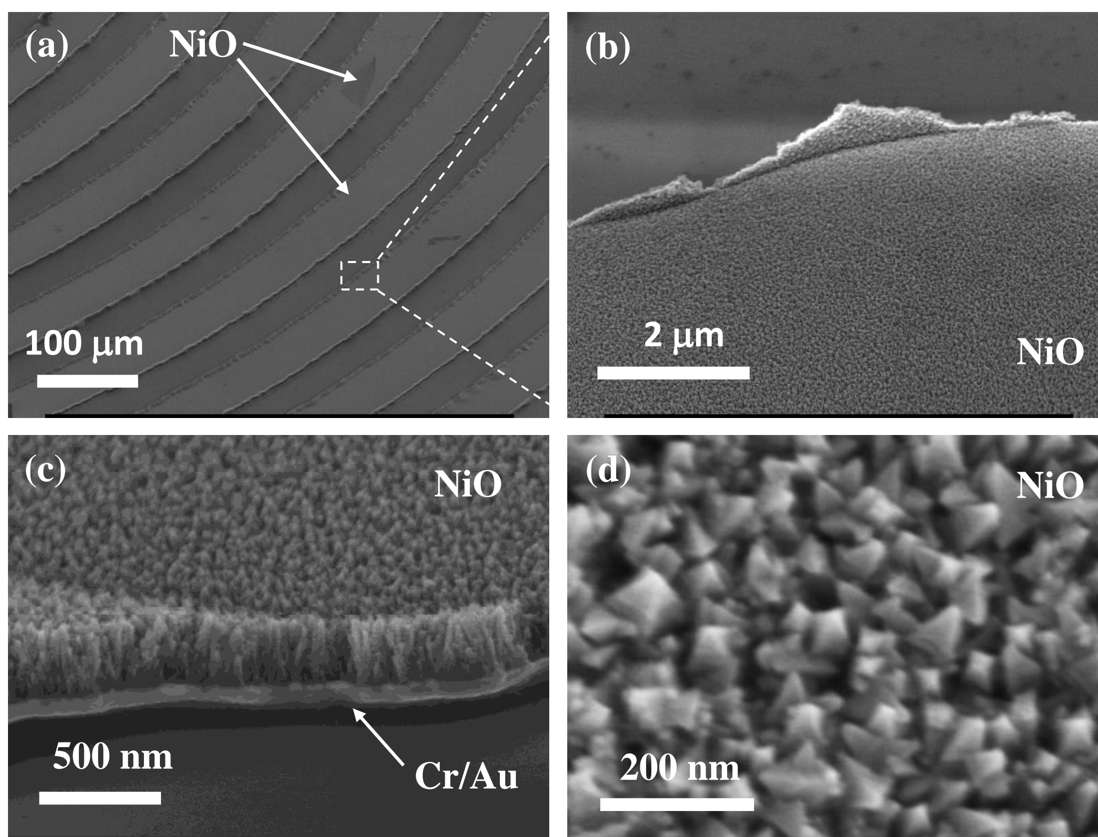

Figure 6.13: SEMs of the photolithographic patterning of microplasma-deposited NiO on Cr/Au electrodes at various magnifications.

As discussed in Chapter 3, since the gas temperature of the plasma jet is low, further baking or damage to the photoresist pattern did not occur, allowing easy liftoff. Given the height of the photoresist (2 μm) and slight undercut that is typical of negative photoresists, small "wings" on the sides of the 50 μm electrode "fingers" are observed. The process may be optimized to reduce these undesirable features by slightly decreasing development time of the photoresist.

Microplasma-based deposition of vertically-aligned MnO_2 nanostructures

Vertically-aligned MnO_2 nanoblades were grown on a degenerately-doped Si wafer substrate for the purpose of XRD, shown in Figure 6.14. Two clear reflections are observed and correspond to either the β-MnO_2 or γ-MnO_2 phases.

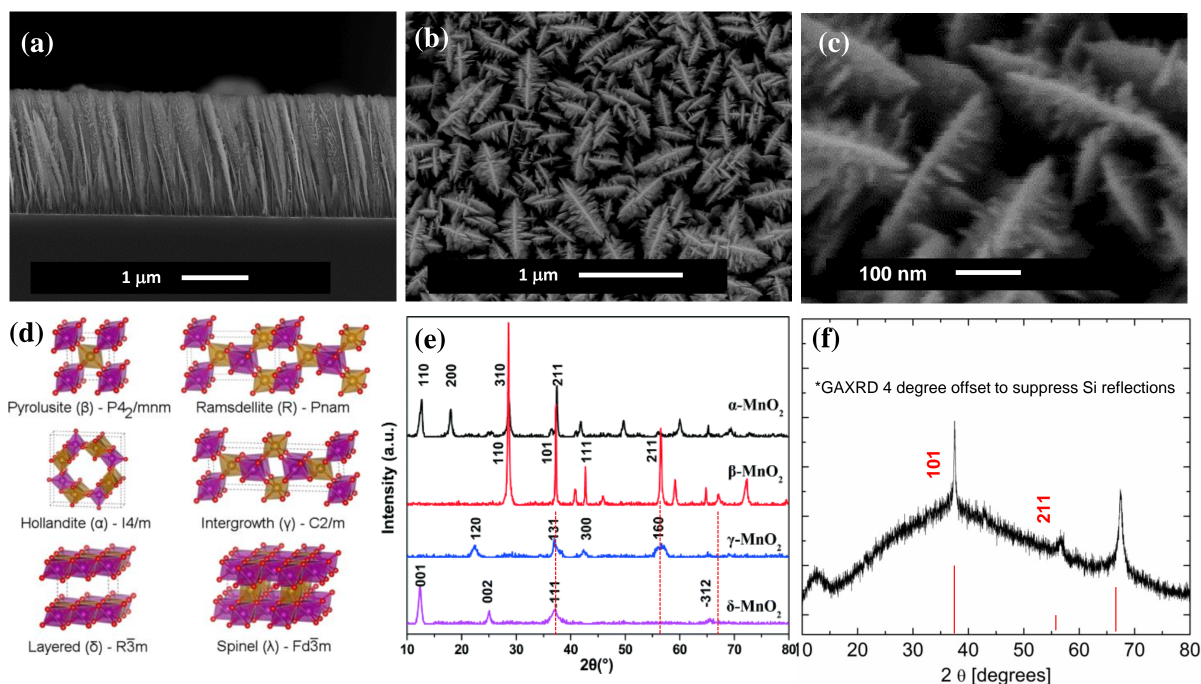

Figure 6.14: (a) Side and (b,c) top views of vertically-aligned MnO_2 nanostructures directly spray deposited on Si substrate using the microplasma jet. (d,e) Crystal structure and XRD patterns of various phases of MnO_2. (f) XRD scan of the MnO_2 film in (a-c), showing reflections that correspond to the known patterns in (e) for the β-MnO_2 or γ-MnO_2 phases.

Then, having optimized the MnO_2 deposition process, the process flow depicted in Figure 6.12 was repeated, but with MnO_2 as the active electrode material. After photoresist liftoff, the microsupercapacitor was rinsed in DI water and dried. The phosphoric acid gel electroylte was then drop-cast onto the electrodes. The resulting device is shown in Figure 6.15.

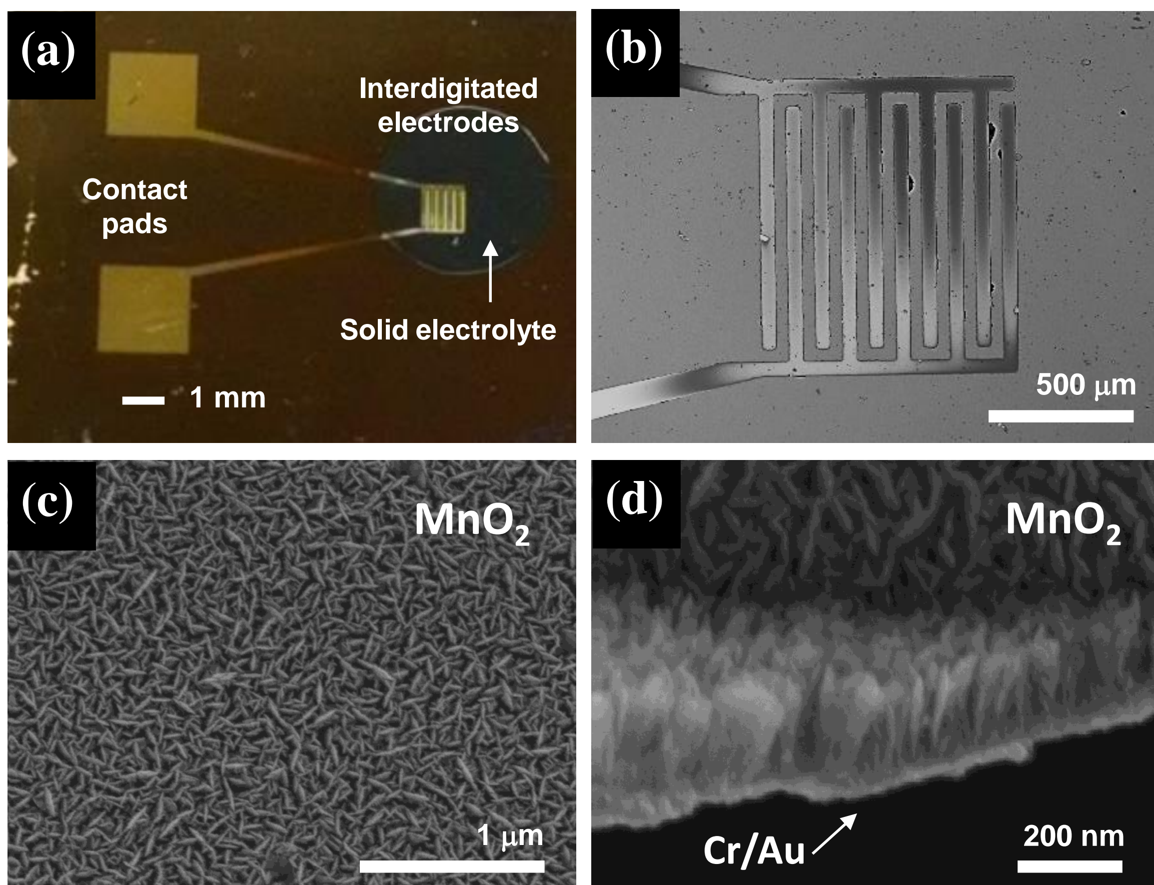

Figure 6.15: A photograph of the finished, all solid-state device is shown in (a). Micrographs of the electrodes and active electrode material are shown in (b-d).

Device characterization

Cyclic voltammetry was used to characterize the MnO_2 microsupercapacitor and is similar to the process described in Section 6.2.3. The potential between the two electrodes was ramped cyclically between 0 and 0.8 V at rates ranging from 10 mV s^{-1} to 200 V s^{-1}. The CV sweeps are shown in Figure 6.16. The expected electrochemical reaction for MnO_2 in acidic electrolyte is as follows:

$$MnO_2 + H^+ + e^- \longleftrightarrow MnOOH \tag{6.6}$$

Similar to the behavior of RuO_2, H^+ easily diffuses into the hydrated oxide structure, resulting in high capacitance. As can be seen in Figure 6.16, the CV sweeps take on a more capacitor-like appearance with more square hysteresis loops, in contrast to the more battery-like behavior of NiO with well defined oxidation and reduction peaks. The MnO_2 CV sweeps were integrated and treated according to Equation 6.5 to calculate specific capacitance. However, instead of normalizing by mass, microsupercapacitor capacities are generally normalized by active material area and volume. These values are calculated and reported in Figure 6.16. At the lowest potential sweep rate (10 mV s^{-1}), a volumetric capacitance of 25 F cm^{-3} and areal capacitance of 600 μF cm^{-2} were observed. The severe drop-off in capacitance as the sweep rate is increased is similar to what was observed in the NiO system in section 6.2.3; at higher scan rates, diffusion limited processes become more apparent, which is especially true when using a gel electrolyte. Further work is needed to optimize electrolyte properties. It should also be noted that a bare (no MnO_2) device of the same dimensions was also tested as a blank (Figure 6.16, triangle symbols), and no capacitive effects were seen.

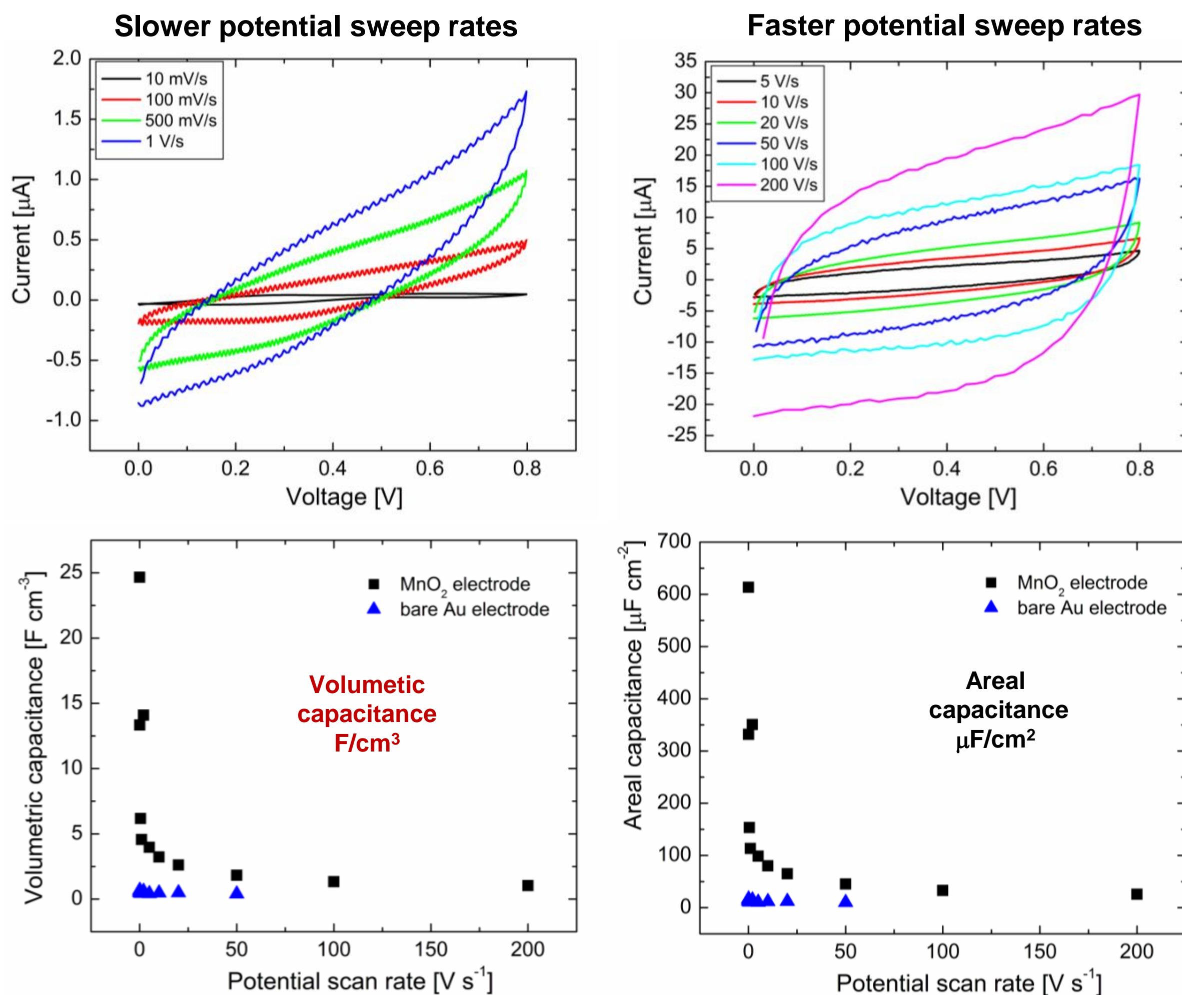

Figure 6.16: Cyclic voltammograms of an MnO_2 microsupercapacitor at various voltage sweep rates. The calculated volumetric and areal capacitances are shown as a function of the voltage scan rate in the lower panels. Data for a "blank" device, without the active MnO_2 material present, is shown with triangle symbols.

6.4.4 Conclusion

A general technique for nanostructure deposition that is compatible with foundry micropatterning techniques was developed and used to fabricate NiO and MnO_2 microsupercapacitors. The microplasma-based method allows for highly localized deposition

of a nanomaterial through a photoresist pattern. Successful patterning of NiO vertically-aligned nanostructures was also demonstrated. The process was repeated for the fabrication of a solid-state MnO_2 based microsupercapacitor. This miniaturized energy storage device was tested using cyclic voltammetry and preformed well in terms of areal and volumentric specific capacitances. Overall, microplasma-based deposition may provide a way to directly deposit pseudocapacitive materials for the fabrication of micro-scale energy storage devices.

Chapter 7

Thesis summary

In this thesis, the design, construction, and characterization of a novel microplasma-jet based deposition source were presented. Application of this new synthesis tool to deposit nanostructured thin film materials, specifically for electrochemical energy storage technologies, was highlighted.

Scientific and technological contributions to the field include:

- Details of how to construct a flow-through MHCD plasma source and deposition system. Fluid mechanics and plasma physics associated with micro-hollow cathode discharges (MHCDs) and their unique operational characteristics were presented.
- Demonstration of how optical emission spectroscopy (OES) and double Langmuir probe (DLP) electrical characterization could be used to determine the rotational, vibrational, and electron temperatures of the jet, allowing a deeper understanding of the MHCD source.
- Demonstration of how the microplasma jet source can be used to deposit a wide variety of nanostructured and mixed metal oxides on virtually any substrate, along

with detailed materials characterization (e.g., SEM/TEM, XPS, CV) of the resulting films and their application to batteries.

- Showing how the electrical configuration of the plasma drive circuit and sample (e.g., related to sample charging for conducting vs. insulating substrates and a grounded vs. floating deposition chuck) insofar as they directly affect the resulting film morphology, crystallinity, composition, and contamination.

- Combining microplasma jet deposition with standard microelectronics foundry techniques to realize electrochemical energy storage devices, namely MnO_2-based microsupercapacitors for on chip energy storage.

Overall, this general, direct, plasma-based deposition technique is relevant to a wide range of current fields of research, as the ability to synthesize nanostructured materials, as well as integrate them into larger systems, is fundamental to the development of next-generation micro- and optoelectronic devices, sensors, and energy harvesting and storage technologies.

Bibliography

[1] M. Sugawara, *Plasma Etching Fundamentals and Applications*, ch. 1, pp. 2–13. Oxford Science Publications, 1998.

[2] A. Lieberman, Michael and A. J. Lichtenberg, *Principles of Plasma Discharges and Materials Processing.* Wiley, 2005.

[3] A. Fridman and L. A. Kennedy, *Plasma Physics and Engineering.* Taylor and Francis, 2004.

[4] G. Tallents, *An Introduction to the Atomic and Radiation Physics of Plasmas.* Cambridge University Press, 2018.

[5] H. R. Griem, *Validity of local thermal equilibrium in plasma spectroscopy*, *Physical review* **131** (1963), no. 3 1170.

[6] U. Fantz, *Basics of plasma spectroscopy*, *Plasma sources science and technology* **15** (2006), no. 4 S137.

[7] S. Muhl and A. Perez, *The use of hollow cathodes in deposition processes: A critical review*, *Thin Solid Films* **579** (2015) 174–198.

[8] K. H. Schoenbach, A. El-Habachi, W. Shi, and M. Ciocca, *High-pressure hollow cathode discharges*, *Plasma Sources Science and Technology* **6** (1997), no. 4 468.

[9] R. H. Stark and K. H. Schoenbach, *Direct current high-pressure glow discharges*, *Journal of applied physics* **85** (1999), no. 4 2075–2080.

[10] G. Stockhausen and M. Kock, *Proof and analysis of the pendulum motion of beam electrons in a hollow cathode discharge*, *Journal of Physics D: Applied Physics* **34** (2001), no. 11 1683.

[11] S. Hashiguchi and M. Hasikuni, *Theory of the hollow cathode glow discharge*, *Japanese journal of applied physics* **26** (1987), no. 2R 271.

[12] D. Mariotti and R. M. Sankaran, *Perspectives on atmospheric-pressure plasmas for nanofabrication*, *Journal of Physics D: Applied Physics* **44** (2011), no. 17 174023.

[13] D. Mariotti and R. M. Sankaran, *Microplasmas for nanomaterials synthesis*, *Journal of Physics D: Applied Physics* **43** (2010), no. 32 323001.

[14] U. R. Kortshagen, R. M. Sankaran, R. N. Pereira, S. L. Girshick, J. J. Wu, and E. S. Aydil, *Nonthermal plasma synthesis of nanocrystals: fundamental principles, materials, and applications*, *Chemical reviews* **116** (2016), no. 18 11061–11127.

[15] C. Richmonds and R. M. Sankaran, *Plasma-liquid electrochemistry: rapid synthesis of colloidal metal nanoparticles by microplasma reduction of aqueous cations*, *Applied Physics Letters* **93** (2008), no. 13 131501.

[16] F.-C. Chang, C. Richmonds, and R. M. Sankaran, *Microplasma-assisted growth of colloidal ag nanoparticles for point-of-use surface-enhanced raman scattering applications*, *Journal of Vacuum Science & Technology A: Vacuum, Surfaces, and Films* **28** (2010), no. 4 L5–L8.

[17] W.-H. Chiang, C. Richmonds, and R. M. Sankaran, *Continuous-flow, atmospheric-pressure microplasmas: a versatile source for metal nanoparticle synthesis in the gas or liquid phase*, *Plasma Sources Science and Technology* **19** (2010), no. 3 034011.

[18] W.-H. Chiang and R. M. Sankaran, *Linking catalyst composition to chirality distributions of as-grown single-walled carbon nanotubes by tuning ni x fe 1- x nanoparticles*, *Nature materials* **8** (2009), no. 11 882.

[19] R. M. Sankaran, D. Holunga, R. C. Flagan, and K. P. Giapis, *Synthesis of blue luminescent si nanoparticles using atmospheric-pressure microdischarges*, *Nano letters* **5** (2005), no. 3 537–541.

[20] J. Goree, *Ion trapping by a charged dust grain in a plasma*, *Physical review letters* **69** (1992), no. 2 277.

[21] H. Maurer and H. Kersten, *On the heating of nano-and microparticles in process plasmas*, *Journal of Physics D: Applied Physics* **44** (2011), no. 17 174029.

[22] S. Askari, I. Levchenko, K. Ostrikov, P. Maguire, and D. Mariotti, *Crystalline si nanoparticles below crystallization threshold: effects of collisional heating in non-thermal atmospheric-pressure microplasmas*, *Applied Physics Letters* **104** (2014), no. 16 163103.

[23] N. Kramer, E. Aydil, and U. Kortshagen, *Requirements for plasma synthesis of nanocrystals at atmospheric pressures*, *Journal of Physics D: Applied Physics* **48** (2015), no. 3 035205.

[24] T. L. Koh and M. J. Gordon, *Spray deposition of nanostructured metal films using hydrodynamically stabilized, high pressure microplasmas*, *Journal of Vacuum Science & Technology A* **31** (2013), no. 6 061312.

[25] T. L. Koh, E. C. OHara, and M. J. Gordon, *Microplasma-based synthesis of vertically aligned metal oxide nanostructures*, *Nanotechnology* **23** (2012), no. 42 425603.

[26] T. Koh and M. Gordon, *Thin-film deposition with high pressure capillary micro-discharges under different supersonic flow and shock regimes*, *Journal of Physics D: Applied Physics* **46** (2013), no. 49 495204.

[27] T. Koh, E. O'Hara, and M. Gordon, *Growth of nanostructured cuo thin films via microplasma-assisted, reactive chemical vapor deposition at high pressures*, *Journal of Crystal Growth* **363** (2013) 69–75.

[28] A. C. Pebley, A. Peek, T. M. Pollock, and M. J. Gordon, *Microplasma-based growth of biphasic nife2o4/nio nanogranular films for exchange bias applications*, *Chemistry of Materials* **26** (2014), no. 20 6026–6032.

[29] A. C. Pebley, P. E. Fuks, T. M. Pollock, and M. J. Gordon, *Exchange bias and spin glass behavior in biphasic nife 2 o 4/nio thin films*, *Journal of Magnetism and Magnetic Materials* **419** (2016) 29–36.

[30] A. C. Pebley, E. Decolvenaere, T. M. Pollock, and M. J. Gordon, *Oxygen evolution on fe-doped nio electrocatalysts deposited via microplasma*, *Nanoscale* **9** (2017), no. 39 15070–15082.

[31] J. A. Thornton, *Influence of apparatus geometry and deposition conditions on the structure and topography of thick sputtered coatings*, *Journal of Vacuum Science and Technology* **11** (1974), no. 4 666–670.

[32] C. Ferreira and J. Delcroix, *Theory of the hollow cathode arc*, *Journal of Applied Physics* **49** (1978), no. 4 2380–2395.

[33] B. D. Fahlman and A. R. Barron, *Substituent effects on the volatility of metal β-diketonates*, *Advanced Materials for Optics and Electronics* **10** (2000), no. 3-5 223–232.

[34] G. Stauf, D. Driscoll, P. Dowben, S. Barfuss, and M. Grade, *Iron and nickel thin film deposition via metallocene decomposition*, *Thin Solid Films* **153** (1987), no. 1-3 421–430.

[35] M. T. Vieyra-Eusebio and A. Rojas, *Vapor pressures and sublimation enthalpies of nickelocene and cobaltocene measured by thermogravimetry*, *Journal of Chemical & Engineering Data* **56** (2011), no. 12 5008–5018.

[36] M. A. Siddiqi, R. A. Siddiqui, B. Atakan, N. Roth, and H. Lang, *Thermal stability and sublimation pressures of some ruthenocene compounds*, *Materials* **3** (2010), no. 2 1172–1185.

[37] K. Becker, K. Schoenbach, and J. Eden, *Microplasmas and applications*, *Journal of Physics D: Applied Physics* **39** (2006), no. 3 R55.

[38] D. Mariotti, *Nonequilibrium and effect of gas mixtures in an atmospheric microplasma*, *Applied Physics Letters* **92** (2008), no. 15 151505.

[39] D. Mariotti, J. Patel, V. Švrček, and P. Maguire, *Plasma–liquid interactions at atmospheric pressure for nanomaterials synthesis and surface engineering*, *Plasma Processes and Polymers* **9** (2012), no. 11-12 1074–1085.

[40] T. Nozaki, A. Ağıral, S. Yuzawa, J. H. Gardeniers, and K. Okazaki, *A single step methane conversion into synthetic fuels using microplasma reactor*, *Chemical engineering journal* **166** (2011), no. 1 288–293.

[41] K. Becker, A. Koutsospyros, S.-M. Yin, C. Christodoulatos, N. Abramzon, J. Joaquin, and G. Brelles-Marino, *Environmental and biological applications of microplasmas*, *Plasma physics and controlled fusion* **47** (2005), no. 12B B513.

[42] E. Stoffels, Y. Sakiyama, and D. B. Graves, *Cold atmospheric plasma: charged species and their interactions with cells and tissues*, *IEEE Transactions on Plasma Science* **36** (2008), no. 4 1441–1457.

[43] M. Moselhy, I. Petzenhauser, K. Frank, and K. H. Schoenbach, *Excimer emission from microhollow cathode argon discharges*, *Journal of Physics D: Applied Physics* **36** (2003), no. 23 2922.

[44] B. Sismanoglu, J. Amorim, J. Souza-Corrêa, C. Oliveira, and M. Gomes, *Optical emission spectroscopy diagnostics of an atmospheric pressure direct current microplasma jet*, *Spectrochimica Acta Part B: Atomic Spectroscopy* **64** (2009), no. 11-12 1287–1293.

[45] C. Laux, T. Spence, C. Kruger, and R. Zare, *Optical diagnostics of atmospheric pressure air plasmas*, *Plasma Sources Science and Technology* **12** (2003), no. 2 125.

[46] P. Bruggeman and R. Brandenburg, *Atmospheric pressure discharge filaments and microplasmas: physics, chemistry and diagnostics*, *Journal of Physics D: Applied Physics* **46** (2013), no. 46 464001.

[47] K. E. Mackie, A. C. Pebley, M. M. Butala, J. Zhang, G. D. Stucky, and M. J. Gordon, *Microplasmas for direct, substrate-independent deposition of nanostructured metal oxides*, *Applied Physics Letters* **109** (2016), no. 3 033110.

[48] M. Simek, G. Dilecce, and S. DeBenedictis, *On the use of the numerical-simulation of the first positive system of n-2. 1. emission and lif analysis*, *Plasma Chemistry and Plasma Processing* **15** (1995), no. 3 427–449.

[49] M. Simek and S. De Benedictis, *On the use of the numerical simulation of the first positive system of n2: Ii. fast trot estimation from the partially resolved (3,0) band*, *Plasma Chemistry and Plasma Processing - PLASMA CHEM PLASMA PROCESS* **15** (09, 1995) 451 – 463.

[50] S. G. Belostotskiy, T. Ouk, V. M. Donnelly, D. J. Economou, and N. Sadeghi, *Gas temperature and electron density profiles in an argon dc microdischarge measured by optical emission spectroscopy*, *Journal of applied physics* **107** (2010), no. 5 053305.

[51] Y. B. Golubovskii and V. Telezhko, *Measurement of gas temperature from the unresolved rotational structure of the first positive band system of nitrogen*, *Journal of Applied Spectroscopy* **39** (1983), no. 3 999–1003.

[52] SpecairFit, *Specair*, *http://www.specair-radiation.net/* (2012).

[53] E. Johnson and L. Malter, *A floating double probe method for measurements in gas discharges*, *Physical Review* **80** (1950), no. 1 58.

[54] B. Beal, L. Johnson, D. Brown, J. Blakely, and D. Bromaghim, *Improved analysis techniques for cylindrical and spherical double probes*, *Review of Scientific Instruments* **83** (2012), no. 7 073506.

[55] R. V. Kennedy, *Theory of the arc hollow cathode*, *Journal of Physics D: Applied Physics* **34** (2001), no. 5 787.

[56] J. M. Williamson and C. A. DeJoseph Jr, *Determination of gas temperature in an open-air atmospheric pressure plasma torch from resolved plasma emission*, *Journal of applied physics* **93** (2003), no. 4 1893–1898.

[57] X. Yu, T. J. Marks, and A. Facchetti, *Metal oxides for optoelectronic applications*, *Nature materials* **15** (2016), no. 4 383.

[58] C. Wang, L. Yin, L. Zhang, D. Xiang, and R. Gao, *Metal oxide gas sensors: sensitivity and influencing factors*, *Sensors* **10** (2010), no. 3 2088–2106.

[59] J. Briscoe and S. Dunn, *Piezoelectric nanogenerators–a review of nanostructured piezoelectric energy harvesters*, *Nano Energy* **14** (2015) 15–29.

[60] Z. Wang and C.-J. Liu, *Preparation and application of iron oxide/graphene based composites for electrochemical energy storage and energy conversion devices: current status and perspective*, *Nano Energy* **11** (2015) 277–293.

[61] D. Merche, N. Vandencasteele, and F. Reniers, *Atmospheric plasmas for thin film deposition: A critical review*, *Thin Solid Films* **520** (2012), no. 13 4219–4236.

[62] H. Jung, J. Park, E. S. Yoo, G.-S. Han, H. S. Jung, M. J. Ko, S. Park, and W. Choe, *Functionalization of nanomaterials by non-thermal large area atmospheric pressure plasmas: application to flexible dye-sensitized solar cells*, *Nanoscale* **5** (2013), no. 17 7825–7830.

[63] R. Suryanarayanan, *Plasma spraying: theory and applications.* World scientific, 1993.

[64] P. Fauchais, *Understanding plasma spraying*, *Journal of Physics D: Applied Physics* **37** (2004), no. 9 R86.

[65] J. Karthikeyan, C. Berndt, J. Tikkanen, S. Reddy, and H. Herman, *Plasma spray synthesis of nanomaterial powders and deposits*, *Materials Science and Engineering: A* **238** (1997), no. 2 275–286.

[66] T. Koh, I. Chiles, and M. Gordon, *Slit-based supersonic microplasma jets: Scalable sources for nanostructured thin film deposition*, *Applied Physics Letters* **103** (2013), no. 16 163115.

[67] J. Kang, O. L. Li, and N. Saito, *A simple synthesis method for nano-metal catalyst supported on mesoporous carbon: the solution plasma process*, *Nanoscale* **5** (2013), no. 15 6874–6882.

[68] D. Mariotti, S. Mitra, and V. Švrček, *Surface-engineered silicon nanocrystals*, *Nanoscale* **5** (2013), no. 4 1385–1398.

[69] A. Kumar, P. A. Lin, A. Xue, B. Hao, Y. K. Yap, and R. M. Sankaran, *Formation of nanodiamonds at near-ambient conditions via microplasma dissociation of ethanol vapour*, *Nature communications* **4** (2013).

[70] M. M. Rahman, I. Sultana, Z. Chen, M. Srikanth, L. H. Li, X. J. Dai, and Y. Chen, *Ex situ electrochemical sodiation/desodiation observation of co 3 o 4 anchored carbon nanotubes: a high performance sodium-ion battery anode produced by pulsed plasma in a liquid*, *Nanoscale* **7** (2015), no. 30 13088–13095.

[71] F. L. Gonzalez, L. Chan, A. Berry, D. E. Morse, and M. J. Gordon, *Simple colloidal lithography method to fabricate large-area moth-eye antireflective structures on si, ge, and gaas for ir applications*, *Journal of Vacuum Science & Technology B* **32** (2014), no. 5 051213.

[72] T. Lopez and L. Mangolini, *On the nucleation and crystallization of nanoparticles in continuous-flow nonthermal plasma reactors*, *Journal of Vacuum Science & Technology B, Nanotechnology and Microelectronics: Materials, Processing, Measurement, and Phenomena* **32** (2014), no. 6 061802.

[73] L. Mangolini and U. Kortshagen, *Selective nanoparticle heating: another form of nonequilibrium in dusty plasmas*, *Physical review E* **79** (2009), no. 2 026405.

[74] X. Wang, D.-M. Tang, H. Li, W. Yi, T. Zhai, Y. Bando, and D. Golberg, *Revealing the conversion mechanism of cuo nanowires during lithiation–delithiation by in situ transmission electron microscopy*, *Chemical Communications* **48** (2012), no. 40 4812–4814.

[75] S.-H. Park and W.-J. Lee, *Hierarchically mesoporous cuo/carbon nanofiber coaxial shell-core nanowires for lithium ion batteries*, *Scientific reports* **5** (2015).

[76] C. Wang, Q. Li, F. Wang, G. Xia, R. Liu, D. Li, N. Li, J. S. Spendelow, and G. Wu, *Morphology-dependent performance of cuo anodes via facile and controllable synthesis for lithium-ion batteries*, *ACS applied materials & interfaces* **6** (2014), no. 2 1243–1250.

[77] L. Wang, H. Gong, C. Wang, D. Wang, K. Tang, and Y. Qian, *Facile synthesis of novel tunable highly porous cuo nanorods for high rate lithium battery anodes with realized long cycle life and high reversible capacity*, *Nanoscale* **4** (2012), no. 21 6850–6855.

[78] K. K. Ostrikov, I. Levchenko, and S. Xu, *Self-organized nanoarrays: plasma-related controls*, *Pure and Applied Chemistry* **80** (2008), no. 9 1909–1918.

[79] H. Profijt, S. Potts, M. Van de Sanden, and W. Kessels, *Plasma-assisted atomic layer deposition: basics, opportunities, and challenges*, *Journal of Vacuum Science & Technology A: Vacuum, Surfaces, and Films* **29** (2011), no. 5 050801.

[80] H. Profijt, M. Van de Sanden, and W. Kessels, *Substrate-biasing during plasma-assisted atomic layer deposition to tailor metal-oxide thin film growth*, *Journal of Vacuum Science & Technology A: Vacuum, Surfaces, and Films* **31** (2013), no. 1 01A106.

[81] H. Kim, S. Woo, J. Lee, Y. Kim, H. Lee, I.-J. Choi, Y.-D. Kim, C.-W. Chung, and H. Jeon, *Effect of dc bias on the plasma properties in remote plasma atomic layer deposition and its application to hfo2 thin films*, *Journal of The Electrochemical Society* **158** (2011), no. 1 H21–H24.

[82] Y. Ito, Y. Fukui, K. Urabe, O. Sakai, and K. Tachibana, *Effect of series capacitance and accumulated charge on a substrate in a deposition process with an atmospheric-pressure plasma jet*, *Japanese Journal of Applied Physics* **49** (2010), no. 6R 066201.

[83] J. Goree, *Charging of particles in a plasma*, *Plasma Sources Science and Technology* **3** (1994), no. 3 400.

[84] A. Sobota, O. Guaitella, and E. Garcia-Caurel, *Experimentally obtained values of electric field of an atmospheric pressure plasma jet impinging on a dielectric surface*, *Journal of Physics D: Applied Physics* **46** (2013), no. 37 372001.

[85] R. Wild, T. Gerling, R. Bussiahn, K. Weltmann, and L. Stollenwerk, *Phase-resolved measurement of electric charge deposited by an atmospheric pressure plasma jet on a dielectric surface*, *Journal of Physics D: Applied Physics* **47** (2013), no. 4 042001.

[86] S. I. EDAX, *Product bulletin - eds*, *https://www.edax.com/products/eds* (2018).

[87] P. C. Nordine and J. D. LeGrange, *Heterogeneous fluorine atom recombination/reaction on several materials of construction*, *AIAA Journal* **14** (1976), no. 5 644–647.

[88] R. Kötz and M. Carlen, *Principles and applications of electrochemical capacitors*, *Electrochimica acta* **45** (2000), no. 15-16 2483–2498.

[89] J. Y. Hwang, M. F. El-Kady, Y. Wang, L. Wang, Y. Shao, K. Marsh, J. M. Ko, and R. B. Kaner, *Direct preparation and processing of graphene/ruo2 nanocomposite electrodes for high-performance capacitive energy storage*, *Nano Energy* **18** (2015) 57–70.

[90] M. Zhi, C. Xiang, J. Li, M. Li, and N. Wu, *Nanostructured carbon–metal oxide composite electrodes for supercapacitors: a review*, *Nanoscale* **5** (2013), no. 1 72–88.

[91] K. Naoi and P. Simon, *New materials and new configurations for advanced electrochemical capacitors*, *Journal of The Electrochemical Society (JES)* **17** (2008), no. 1 34–37.

[92] V. Augustyn, P. Simon, and B. Dunn, *Pseudocapacitive oxide materials for high-rate electrochemical energy storage*, *Energy & Environmental Science* **7** (2014), no. 5 1597–1614.

[93] D. P. Dubal, P. Gomez-Romero, B. R. Sankapal, and R. Holze, *Nickel cobaltite as an emerging material for supercapacitors: an overview*, *Nano Energy* **11** (2015) 377–399.

[94] C. Windisch Jr, G. J. Exarhos, K. F. Ferris, M. H. Engelhard, and D. C. Stewart, *Infrared transparent spinel films with p-type conductivity*, *Thin Solid Films* **398** (2001) 45–52.

[95] R. Moore and J. White, *Equilibrium relationships in the system nio-coo-o 2*, *Journal of Materials Science* **9** (1974), no. 9 1393–1400.

[96] M. M. Sk, C. Y. Yue, K. Ghosh, and R. K. Jena, *Review on advances in porous nanostructured nickel oxides and their composite electrodes for high-performance supercapacitors*, *Journal of Power Sources* **308** (2016) 121–140.

[97] X. Ren, C. Guo, L. Xu, T. Li, L. Hou, and Y. Wei, *Facile synthesis of hierarchical mesoporous honeycomb-like nio for aqueous asymmetric supercapacitors*, *ACS applied materials & interfaces* **7** (2015), no. 36 19930–19940.

[98] R. S. Kate, S. A. Khalate, and R. J. Deokate, *Overview of nanostructured metal oxides and pure nickel oxide (nio) electrodes for supercapacitors: a review*, *Journal of Alloys and Compounds* **734** (2018) 89–111.

[99] S. Vijayakumar, S. Nagamuthu, and G. Muralidharan, *Supercapacitor studies on nio nanoflakes synthesized through a microwave route*, *ACS applied materials & interfaces* **5** (2013), no. 6 2188–2196.

[100] N. A. Kyeremateng, T. Brousse, and D. Pech, *Microsupercapacitors as miniaturized energy-storage components for on-chip electronics*, *Nature nanotechnology* **12** (2017), no. 1 7.